Volcanic and Sedimentary Geology of the Basaltic Karaka Volcano, South Auckland

A thesis

submitted in partial fulfilment

of the requirements for the degree

of

Master of Science (Research) in **Earth Sciences**

at

The University of Waikato

by

MADISON KEDDIE IVY HANSEN

THE UNIVERSITY OF
WAIKATO
Te Whare Wānanga o Waikato

2020

Abstract

Intraplate monogenetic volcanic fields are a common volcanic feature of the upper western North Island. There are four geographically related fields, approximately 38 km apart which young northwards from Raglan to Auckland. The South Auckland Volcanic Field (SAVF; 1.56–0.51 Ma) is older and more degraded than the Auckland Volcanic Field (AVF; active since 250 ka) to the north. Located between the two fields and overlying the Late Pliocene to Mid-Pleistocene pumiceous fluvial deposits of the Puketoka Formation, is the newly discovered Karaka Volcano. Although residents had referred to a volcanic landform in the area, it was in 2018 that evidence for a volcano based on geomorphology, a magnetic anomaly, weathered surficial deposits and water bore data was reported.

This thesis will present the recent findings of the volcano-sedimentary geology of the Karaka volcano. Evidence is based on stratigraphic analysis of two new drill cores, a complementary resistivity survey, petrography, scanning electron microscopy and geochemical investigations. One drill core intersected an upper 6 m blanket of Hamilton Ash Formation and a lower 7 m succession of interbedded, laminated dark brown organic-rich silts, and distal tephras. The lower succession is consistent with lake sediments associated with a crater lake within the geomorphic tuff ring. The second drill core, on the central high point of the volcanic landform, intersected an upper 6 m of brown and red clay. Beneath this, is a lower 9.5 m succession of volcanic ash, coarsening downwards, to a basaltic lapilli ash deposit with a lithic-rich matrix. This represents a phreatomagmatic phase in the upper part of the volcanic sequence. The resistivity survey connects the two drill holes giving an indication of extent and layering of the geology beneath the surface. No recognised volcanoes are within 5 km of this site, so it is unlikely that this pyroclastic deposit came from a distal vent, despite its isolated location outside of the predefined margins of the South Auckland and Auckland volcanic fields.

Basalt lapilli within the pyroclastic succession are porphyritic with a trachytic to glassy groundmass with predominant phenocrysts of olivine, augite, opaque

minerals and plagioclase. Geochemical analysis was conducted on whole rock samples of basalt lapilli by X-ray fluorescence spectroscopy (XRF) and on pyroxene, olivine, plagioclase and zeolites by electron probe microanalysis (EPMA). This data identified Karaka Basalt as a member of the Group B basalts of the SAVF. Lithics were fragments of the underlying sandstone and siltstone of the Waitemata Group. The surrounding matrix comprised small basalt fragments, lithics, quartz and plagioclase.

Glass compositions of tephra by EPMA provide information that has been used to produce a tentative minimum age on the crater lake and by proxy the volcano itself. Tephra TW gives a possible correlation to the Kidnappers Ignimbrite which has been dated previously at ~0.99 Ma. The age of this tephra along with belonging to the SAVF, and a covering of Kauroa and Hamilton Ashes, gives the Karaka Volcano an approximate age range of 1.56 – 0.99 Ma.

Acknowledgements

Completing a thesis in Earth Sciences has been a long time coming for me and has been an exciting time in my life. Delving into the world of research has allowed me to improve my critical thinking and share my ideas and information more eloquently, and I hope this thesis represents this improvement well.

A massive thanks go to my supervisor Dr Adrian Pittari who helped with any number of things from direction and organisation of this excellent topic to helping slug core barrels around in the field. The thorough editing of chapters and help sifting through my data has also been a tremendous help.

A large thanks to Dr Bruce Hayward, who started this project off and spurred it on giving good insight and experience to my investigations.

To the farm owners Ian and Jim Ross, who allowed us free reign over their property to investigate this landform as well as monetary contributions to drilling, I am very grateful. Other land users on-site also require thanks for putting up with our disturbance and managing animals so we could perform field testing, thank you!

This data could not have been gained without the help of many others who have spent their time assisting me. Cheers to those that have helped me in the field, including Noel Bates, Chris Morcom, Dean Sandwell and Chris-Anne Ross. Gratitude to those who have helped me in the lab at the University of Waikato, including Annette Rodgers, Kirsty Vincent and Renat Radosinksy. I would also like to thank those further afield at the Victoria University of Wellington, including Dr Jenni Hopkins for undertaking EPMA analysis on tephra glass and helping with tephra analysis and Dr Ian Shipper for assistance on the EPMA.

Funding has come in the form of The University of Waikato Masters Research Scholarship.

Finally, thank you to my family who probably will not be able to understand much of this work but who have often been more excited than me about this project and who have spurred me on with their kind words and pride in what I have been doing. To Kim, thank you for urging me on, being stressed about this for me and single-handedly also being the biggest distraction from its completion. Although the week we took off to learn the piano was well worth it!

Table of Contents

List of Figures

List of Tables

Chapter 1

Introduction

1.1 Introduction

Generation of a volcano in a monogenetic volcanic field often occurs in a single eruptive episode. Eruptions in intraplate basaltic fields create discrete but often overlapping volcanic landforms. Eruption styles associated with monogenetic fields, include Strombolian eruptions and Hawaiian fire fountaining, which can create scoria cones and lava flows, as well as phreatomagmatic eruptions creating maars or tuff rings. In many long-lived or extinct monogenetic fields, volcanic centres may be eroded and buried beneath younger volcanic deposits or more recent sedimentary successions.

Investigation of the now-extinct South Auckland Volcanic Field (SAVF) and the active Auckland Volcanic Field (AVF) has led to thorough mapping and dating of volcanic features. However, amongst these two fields, there is still potential for the discovery of further undiscovered volcanic landforms. One such landform, the Karaka Volcano, was identified in late 2017 by Auckland geologist, Bruce Hayward (2018). The Karaka Volcano is a small landform in South Auckland (Figure 1.1). The discovery of this volcano led to media attention and local public interest, due to the intended land use of the volcano and its potential for future geoheritage status.

1.2 Research Aim and Objectives

This study aims to use modern methods to confirm the newly identified volcanic landform in Karaka, as well as attempt to outline the eruptive history of the volcano. The following objectives will address this aim:

- To use field outcrops, drill core and resistivity to get an indication of sediments located in and around the Karaka Volcano.

- To describe the basaltic pyroclastic sequence of the Karaka Volcano through core interpretation and determining the origins of basalt and lithics present within the core.
- To examine and interpret the characteristics of sedimentary deposits at the surface and in drill core.

Figure 1.1: The study site, as shown on a map of the North Island of New Zealand.

1.3 Methods

The methods undertaken to achieve the objectives above were; field near-surface studies including a general site walkover, hand auger sampling; and subsurface studies including drilling of two cores and a resistivity survey. Laboratory analysis conducted includes optical microscopy, scanning electron microscopy (SEM), electron probe micro-analyzer (EPMA), x-ray diffraction (XRD), x-ray fluorescence (XRF), loss on ignition (LOI) and grain sizing.

Descriptions of detailed methodologies are within individual chapters.

1.4 Study Area

Karaka is an Auckland suburb to the west of Papakura and south of the Manakau Harbour. The study site is between Laing and Urquhart roads 5 km north of the SAVF. The surrounding area has gently rolling topography. At Urquhart road, the topography has more significant relief – it includes the highest point of the local Karaka area at 71 m above sea level (asl). This high point is surrounded by small gullies and streams (Figure 1.2) draining south and east into Whagapouri Creek or north into the Manakau Harbour. The surrounding area consists of farmland as well as lifestyle blocks and farm buildings.

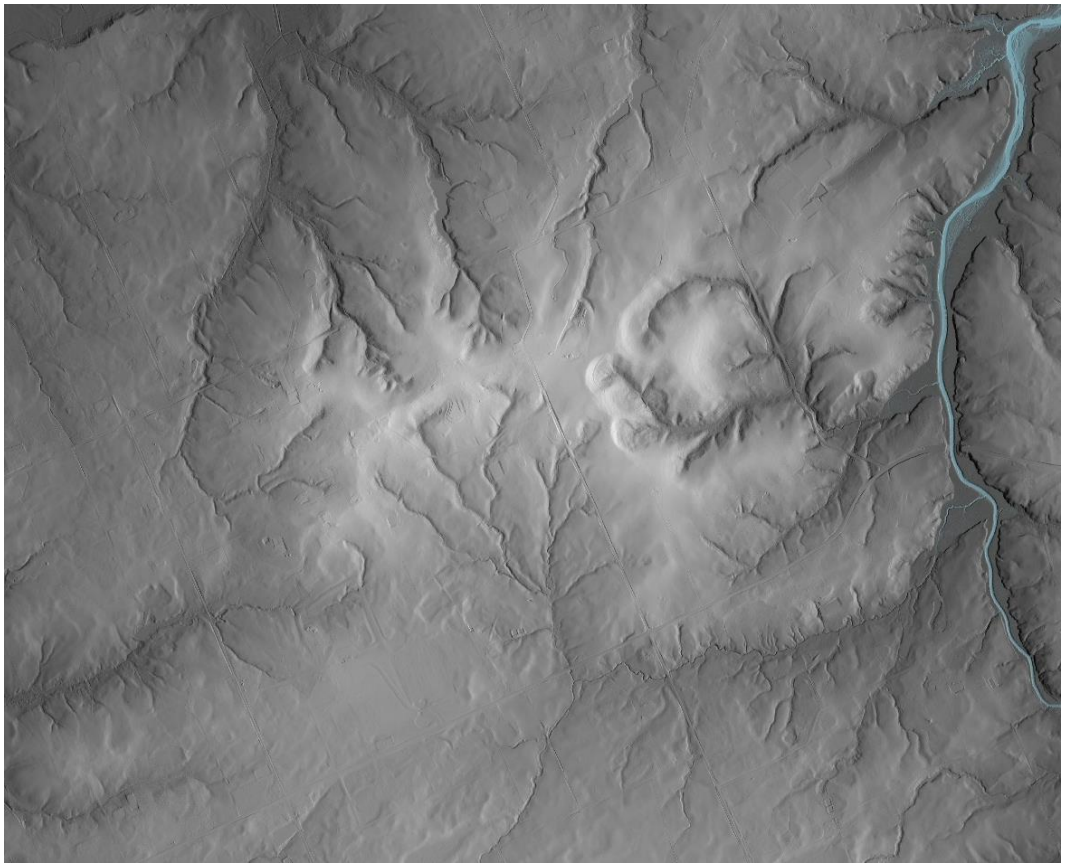

Figure 1.2: A hill shade of the Karaka Volcano and the surrounding area, indicating topography.

1.5 Thesis Structure and Chapter Outline

Chapter 2 covers background literature associated with the Karaka Volcano and regional geology. This chapter includes previous work conducted on-site as well as a background to the SAVF and AVF, underlying geology, cover ash sequences and regional New Zealand geological context.

Chapter 3 describes the two drill cores conducted on the Karaka Volcano, with detail on their stratigraphic succession.

Chapter 4 goes into detail of the petrological analysis of volcanic material retrieved in drill hole two. It describes the geochemical analysis conducted on the same samples.

Chapter 5 details the sedimentary succession of drill hole one and shows SEM imagery of different layers within a sedimentary organic deposit.

Chapter 6 is a discussion on the results from the previous chapters, especially concerning the volcanic and sedimentological history of the volcanic centre.

Chapter 2

Literature Review

2.1 Geological Setting of New Zealand

The New Zealand landmass resides in the Pacific Ocean on the continent of Zealandia. The geology of New Zealand is built up of terranes (Figure 2.1) created by scraping sediment off of the subducting Paleo-Pacific Plate, (Sutherland & King, 2015). This scraping formed accretionary prisms bounded by faults (Mortimer, 2015). Accumulation of these terranes occurred before the separation of Gondwana from the still joined Australia and Zealandia 83 Ma due to sea-floor spreading on the Antarctic-Australia Ridge (Mortimer, 2015). Zealandia separated from Australia 73 Ma with the formation of a spreading ridge in the Tasman Sea (Sutherland & King, 2015). Formation of accretionary prisms has created a pattern of geology with younger material in the west and older material in the east of New Zealand (Bradshaw, 1989; Laird & Bradshaw, 2004).

The terranes seen in Figure 2.1 have three rock types, sedimentary, igneous, and metamorphic. Igneous batholiths include the Honu, Paparoa, Karamea and Median Batholiths. Sedimentary terranes include the Buller, Takaka, Torlesse Composite (Rakaia, Kaweka and Pahau), Brook Street, Caples, Maitai, Murihiku, and Waipapa Composite terranes. Metamorphosed rock is found in several belts throughout the country, such as the Esk Head belt in the Pahau Terrane (Mortimer, 2015).

New Zealand's current position straddles the Pacific and Indo-Australian Plates boundary, formed around 30 Ma (Furlong & Kamp, 2009). In the north, the Pacific Plate (Figure 2.1) undergoes subduction beneath the Indo-Australian Plate by as much as 47 mm per year, (Horspool *et al.*, 2006) creating the Hikurangi Trench. The plate boundary then crosses onto land south of Wellington where it transitions from a subduction to a transpression boundary, causing strike-slip movement along the Alpine Fault. This section of the plate boundary has led to

the continual uplift of the Southern Alps through shortening of the continental crust (Furlong & Kamp, 2009). To the far south, the Indo-Australian Plate subducts the Pacific Plate at approximately 37 mm per year (Horspool *et al.*, 2006), creating the Puysegur Trench.

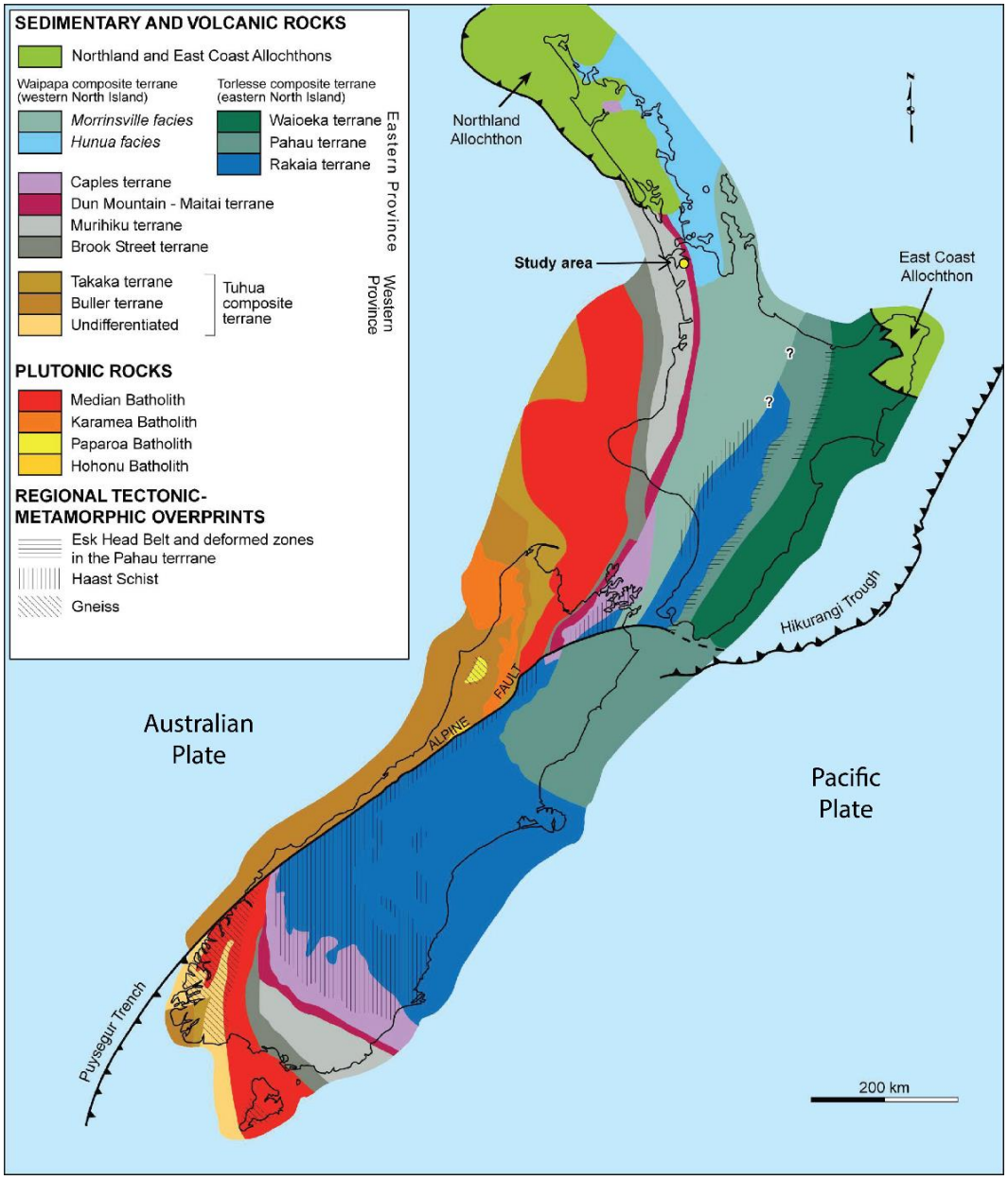

Figure 2.1: Terranes that make up the geology of New Zealand. The plate boundary that New Zealand sits on is pictured and shows the dynamic nature of the boundary (Kamp *et al.*, 2008a).

The convergence of the Pacific and Indo-Australian Plates has played a significant role in Cenozoic volcanism in the North Island of New Zealand. Subduction related-volcanism associated with the Hikurangi Margin (Horspool *et al.*, 2006) has

migrated southeastward over time through Northland, the Coromandel Volcanic Zone (CVZ), and finally the currently active Taupo Volcanic Zone (TVZ) and ranges from andesite to rhyolite in composition (Ballance, 1976; Hayward *et al.*, 2001; Cook *et al.*, 2005). There are several intraplate basalts in the North Island seen in Figure 2.2. These basalt fields are approximately 35 to 38 km apart with a general southwards aging (Briggs *et al.*, 1994). These fields are, Auckland Volcanic Field (AVF; 250,000 to 550 ya; (Lindsay *et al.*, 2011; Needham *et al.*, 2011)), South Auckland Volcanic Field (SAVF; 1.56-0.51 Ma; (Briggs *et al.*, 1994)), Ngatutura Basalts; (1.83-1.54 Ma; (Briggs *et al.*, 1989)) and the Okete Volcanic Field; (2.69-1.80 Ma (Ballance, 1976; Briggs *et al.*, 1989; Cook *et al.*, 2005)). The Northland Volcanic Province (10 Ma and 1800-1300 ya; (Smith *et al.*, 1993)), is another intraplate basaltic field in the North Island. However, it does not follow the same spatial trend mentioned above.

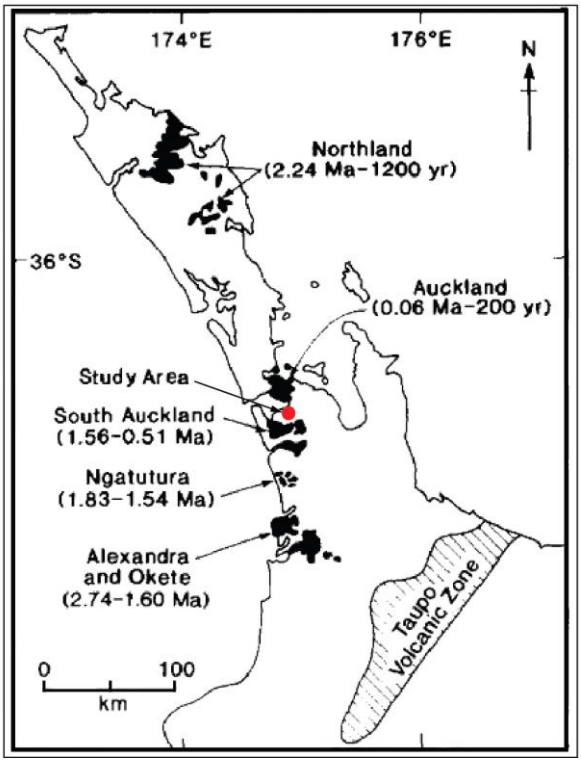

Figure 2.2: The location and age of intraplate basaltic fields in the North Island of New Zealand, with consideration to the Taupo Volcanic Zone (Briggs *et al.*, 1994).

2.2 South Auckland Volcanic Field

The SAVF (Figure 2.3) is an extinct monogenetic intra-plate basaltic field in the North Island of New Zealand (Nemeth *et al.*, 2012). The SAVF was active between 0.51 and 1.56 Ma with two peaks of activity at 0.6 and 1.3 Ma (Briggs *et al.*, 1994; Cook *et al.*, 2005). The field spans 300 km^2 extending from Drury to Pukekawa, north to south, and Hunua and Waiuku, east to west (Briggs *et al.*, 1994). It contains approximately 82 monogenetic volcanic centres, with 38 maars and tuff rings, 17 scoria cones, and 40 lava shields, several are counted as one volcanic centre (Nemeth *et al.*, 2012; Hayward, 2015; Mullane, 2015). The subducting Pacific Plate is absent beneath the SAVF showing volcanism here is caused by decompression melting and not related to the plate boundary (Briggs *et al.*, 1994; Cook *et al.*, 2005).

Raised blocks of Mesozoic greywacke and argillite basement occur on the eastern and southern sides of the SAVF. These blocks are overlain unconformably by transgressive Te Kuiti Group sediments (Rafferty, 1977). The Te Kuiti Group sediments accumulated east of the Taranaki Fault and can be hundreds of metres thick. Concentrations of exposed outcrops occur between Papakura and Taumaranui. The Waikato Coal Measures are the lowermost unit of the sequence, and the Otorohanga Limestone is the most recent. These and those in between are intermittent sediments formed from coastal through to bathyal environments (Kamp *et al.*, 2008a; Tripathi *et al.*, 2008). The Te Kuiti Group was overlain unconformably in the early Miocene by the Waitemata Group (Rafferty, 1977; Kamp *et al.*, 2008b). The Waitemata Group is a heterogenetic assemblage of shallow marine sediments(Hayward & Brook, 1984) that occur as a turbidite sequence of interbedded sandstone and siltstone, outcropping in Auckland and Northland (Ballance, 1964).

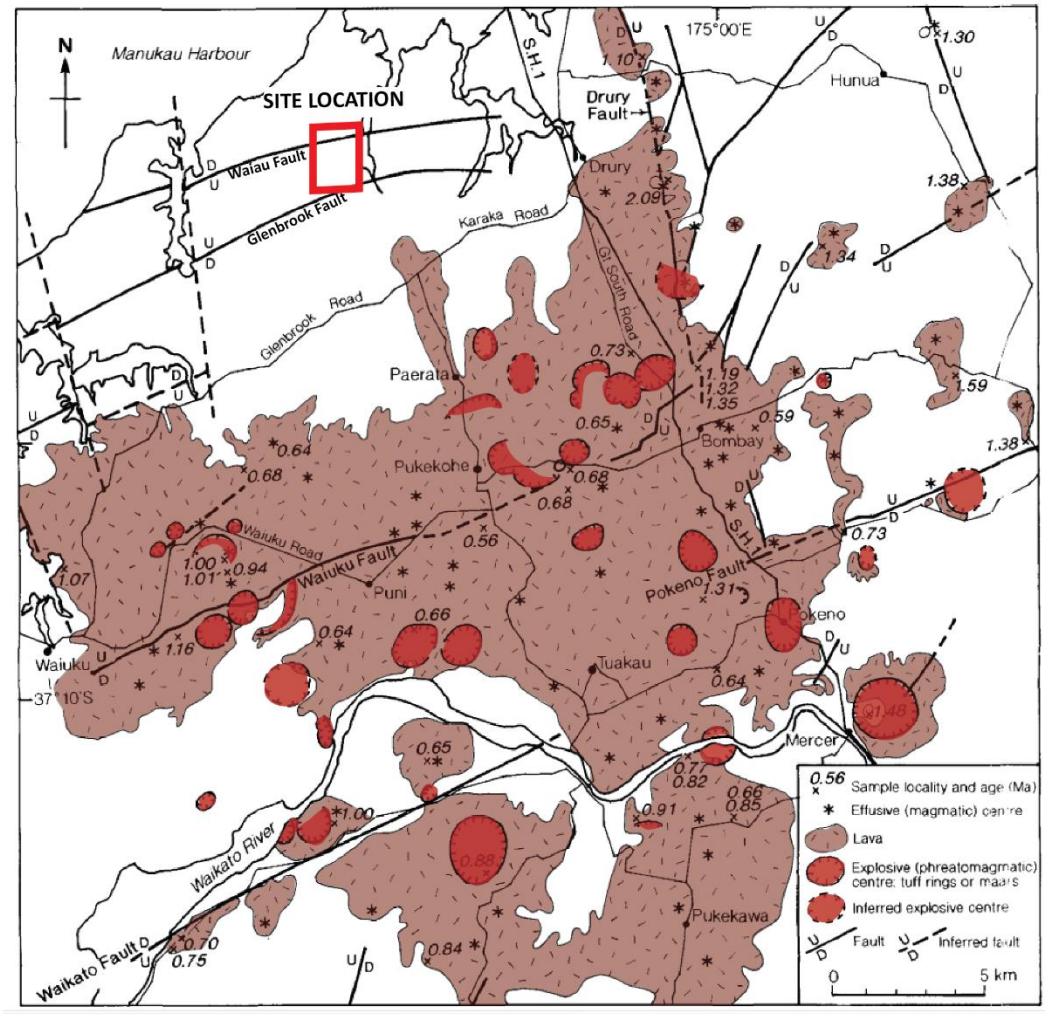

Figure 2.3: The SAVF, displaying volcanic centres and some of their ages as well as faults in the field (Briggs *et al.*, 1994).

The down-faulted blocks in the central SAVF are infilled with marine and estuarine sand and siltstones, such as the Kaawa Formation and Quaternary fluvial estuarine sediments (Briggs *et al.*, 1994; Edbrooke, 2001). The Kaawa Formation consists of coarse to medium sandstone with interbedded shell beds. Within it, small rounded volcanic and Waitemata sandstone fragments are found (Schofield, 1958a). Also infilling down-faulted blocks are Pliocene and Holocene fluvial and lacustrine gravels, sands, silts, and muds of the Tauranga Group. Tauranga Group sediments are intercalated with ignimbrites and tephras from the TVZ and CVZ (Nemeth *et al.*, 2012). These ignimbrites are made of pumiceous, terrestrial and minor estuarine sediments exposed in lowland areas south and west of Auckland, named the Puketoka Formation (Rafferty & Heming, 1979; Edbrooke, 2001). These more recent sediments deposited in the Pliocene and Pleistocene have high

permeability, porosity and transmissivity creating suitable aquifers at 100-200 m below sea level (Briggs *et al.*, 1994; Hayward, 2015).

Block faulting within the SAVF occurred following deposition of the Te Kuiti Group in the early Miocene and again during the Kaikoura orogeny in the Oligocene. This faulting has created the topography seen today underlying the SAVF volcanos. Several of the faults found in the SAVF strongly affect the geomorphology of the area, including the Drury Fault on the western margin of the Hunua Block. Some faults are linked to volcanic centres in the SAVF; for example, an ENE-alignment of vents occurs along the Waiuku and Pokeno faults (Schofield, 1958b).

Tuff rings, maars and scoria cones were formed in the SAVF by different processes. Formation of tuff rings and maars occurs in phreatomagmatic or explosive eruptions due to magma interaction with aquifers in the subsurface geology (Nemeth & Kereszturi, 2015). These often occurred in clusters ranging in size from 0.5 to 2.5 km in diameter (Rafferty & Heming, 1979). Two types of scoria cones are formed through strombolian and Hawaiian eruptions, and lava flows (Briggs *et al.*, 1994). These cone types are; small steep-sided cones associated with one lava flow, with moderately vesicular lava, and lower profile cones that are larger, and with less scoria and more extensive lava flows (Rafferty, 1977). Two groups of basalt, groups A and B, have also been identified within the field, with mineralogical, geochemical differences and no spatial trends (Cook et al., 2005). Group A basalts are hypersthene normative, subalkaline, silica-undersaturated, and have low total alkalis that transition into quartz-tholeiitic basalts. Group B basalts are nepheline normative, alkaline, strongly silica undersaturated with high total alkalis that occur as basanites to nepheline-hawaiites. These magma types suggest the progressive melting of the mantle beneath the region (Rafferty & Heming, 1979).

The SAVF is older than the AVF and is much more eroded and less preserved. Lava throughout the SAVF field is weathered irregularly and is a poor indicator of age (Rafferty, 1977). Draping the SAVF, unlike the AVF, are up to 6 m of the Hamilton Ash Formation. Erosion of this 350,000 to 100,000 ya ash has occurred on some volcanic landforms (Hayward, 2015).

2.3 Auckland Volcanic Field

The active AVF covers 360 km^2 over much of New Zealand's largest city, Auckland (Figure 2.4)(Bebbington & Cronin, 2011). It contains 50 monogenetic centres with 26 maars and tuff rings, ranging in size from 700 m to 1.4 km in diameter, as well as scoria cones and lava flows. Eruptions began approximately 250 ka and continued until around 550 ya with the eruption of Rangitoto (Molloy *et al.*, 2009).

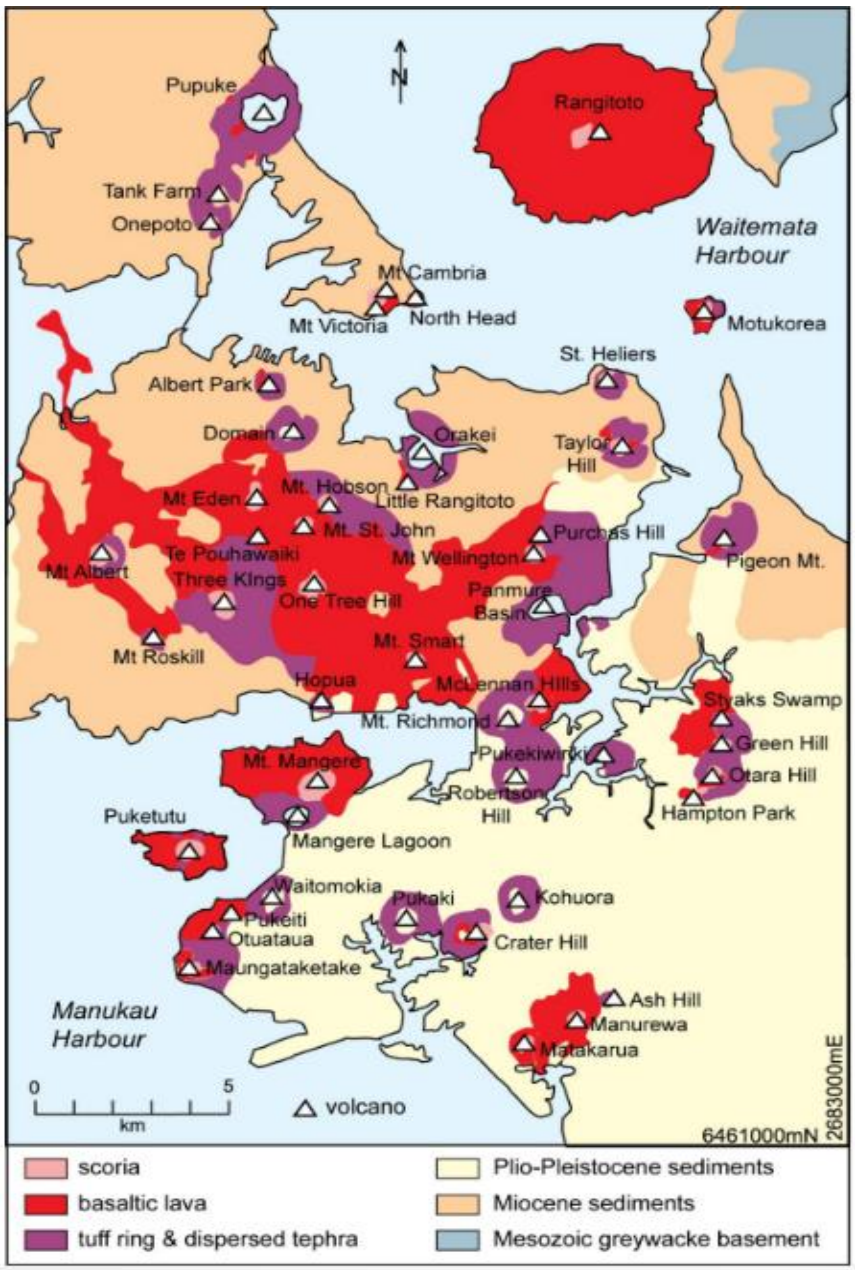

Figure 2.4: A map of the AVF displaying underlying geology and volcanic features (Lindsay *et al.*, 2011).

These eruptions have increased in volume and rate in the last 2,000 years and range in composition from olivine basalt to basanite. Effusion volumes range from 0.01 to 0.05 km^3 except for Rangitoto, which produced 0.3 km^3 of material (Smith *et al.*, 2008; Molloy *et al.*, 2009). Magma in these eruptions is derived from a shallow mantle source with low upwelling rates from 70 to 90 km deep through a ~30 km thick crust (Horspool *et al.*, 2006). Compared to the SAVF, vents here display little structural, spatial or age trends (Bebbington & Cronin, 2011).

Underlying the AVF is a thick sequence of Mesozoic greywacke and argillite, as well as mud, sand and silt beds from the Miocene Waitemata Group. Uplifted fault blocks and small volcanoes <100 m high make up the current topography (McDougall *et al.*, 1969; Sporli & Eastwood, 1997). Tuff rings in some places have been overlain by scoria as phreatomagmatic processes die down partway through an eruption. Phreatomagmatic deposits are found with sand and silt matrices from the Waitemata Group and younger fluvial-lacustrine to shallow marine Pliocene sediments (Nemeth *et al.*, 2012). Phreatomagmatic eruptions in Auckland have generally occurred on swampy ground or near surface water. These eruptions create craters 50 to 100 m deep and between 200 and 1000 m wide (Hayward *et al.*, 2011).

2.4 Tephrochronology

Tephras are unconsolidated deposits from pyroclastic fall and flow processes associated with explosive volcanic eruptions. The composition of tephras vary between eruptions and may include volcanic glass, crystals, pumice, scoria, and country-rock lithics. Components and particle sizes within tephra often vary depending on several conditions, including distance from the vent and atmospheric conditions. These variations make the correlation of tephras between sites difficult when considering their thickness, colour and proportion of components. When tephras can be correlated, they are effective at aligning and dating paleoenvironments. If visual descriptions of tephras do not match, there are several other ways of correlating tephras. They can be examined and matched through identifying mineral assemblages under a microscope and chemical

analysis of glass shards (Alloway *et al.*, 2004; Lowe, 2011). EPMA can be used to determine the major (>1%) and minor (0.1-1%) elemental composition of tephras, which is often enough to correlate tephra between outcrops. If the major and minor elemental analysis is not useful in distinguishing between two tephras, then LA-ICP-MS (laser ablation inductively coupled plasma mass spectrometry) can be used to examine the trace elements (<0.1%) (Lowe *et al.*, 2017). Dating of tephras can be accomplished through relative dating and radiometric dating (e.g. ^{14}C or various zircon dating methods) (Lowe *et al.*, 2017).

Rhyolitic and andesitic tephras are more widespread than basaltic tephras, which are likely only to be locally dispersed, although small particles of glass can travel hundreds to thousands of kilometres away from a vent. In the North Island, most tephras are generally from andesite and rhyolite-dominated volcanism from the CVZ and TVZ. The Hamilton Ash (Figure 2.5) is a sequence of tephra layers used as marker beds across the North Island. The Hamilton Ash can be up to 6 m thick with a strongly weathered clay texture and comprising multiple rhyolitic beds, paleosols, and loess (Lowe *et al.*, 2001). The Hamilton Ash is widespread across the Waikato, Coromandel and parts of South Auckland and is generally underlain unconformably by the Kauroa Ash Formation (Lowe, 2010).

The Hamilton Ash comprises of H1, also known as the Rangitawa tephra, at the base through to H7 at the top. In some places, H1 does not exist, and H2 is at the base. The Rangitawa tephra is pinkish to brownish, halloysitic, grey silt, with distinctive golden platy minerals. Marking the base is a 5 cm thick yellow layer with coarse sand-sized quartz crystals. A likely source of these ashes is the Whakamaru Group ignimbrite possibly produced from the Whakamaru caldera volcano (Lowe *et al.*, 2001). Overlaying it is 3 m of reddish-yellow, dark brown and very pale brown clayey soils (Kamp & Lowe, 1981; Lowe, 2008). The topmost layer H6/7 is a reddish-brown buried soil, also known as the Tikotiko Ash Member (Lowe, 2008).

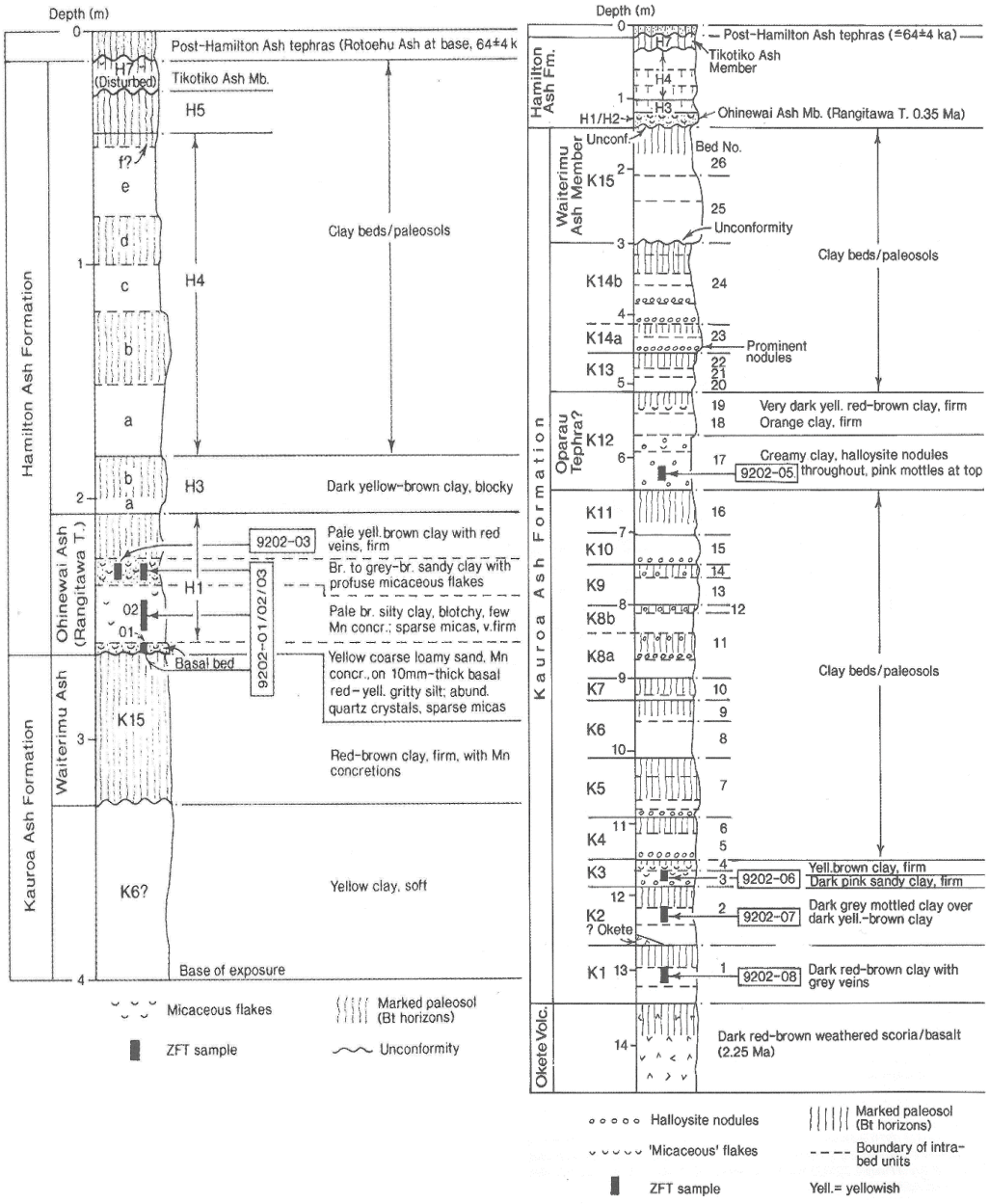

Figure 2.5: Stratigraphic columns of the Hamilton and Kauroa Ash beds (Lowe *et al.*, 2001).

Comprising the Kauroa Ash Formation (Figure 2.5) are 15 identified tephra beds, K1 through to K15. These tephra beds are incredibly weathered and clay-rich and are intercalated by paleosols, together comprising a sequence up to 12 metres thick. Deposition occurred between 2.24 and 0.8 Ma, and possible sources include young CVZ or older TVZ volcanic centres (Horrocks, 2000; Lowe *et al.*, 2001).

2.5 Previous Work

In 2018 evidence was provided for a previously undiscovered volcanic landform in South Auckland (Hayward, 2018). This landform is suggested to lie between Linwood, Urquhart and Laings Roads, in Karaka, north of the SAVF and south of the AVF. Topographic patterns in the area suggested a highly eroded volcanic cone nestled within a tuff ring (Figure 2.6). The average elevation of the area is 25 m asl, but the summit of the proposed volcanic cone and the surrounding ring rise to between 50 and 70 m asl, which also forms a small easterly-striking ridge to the west of the cone.

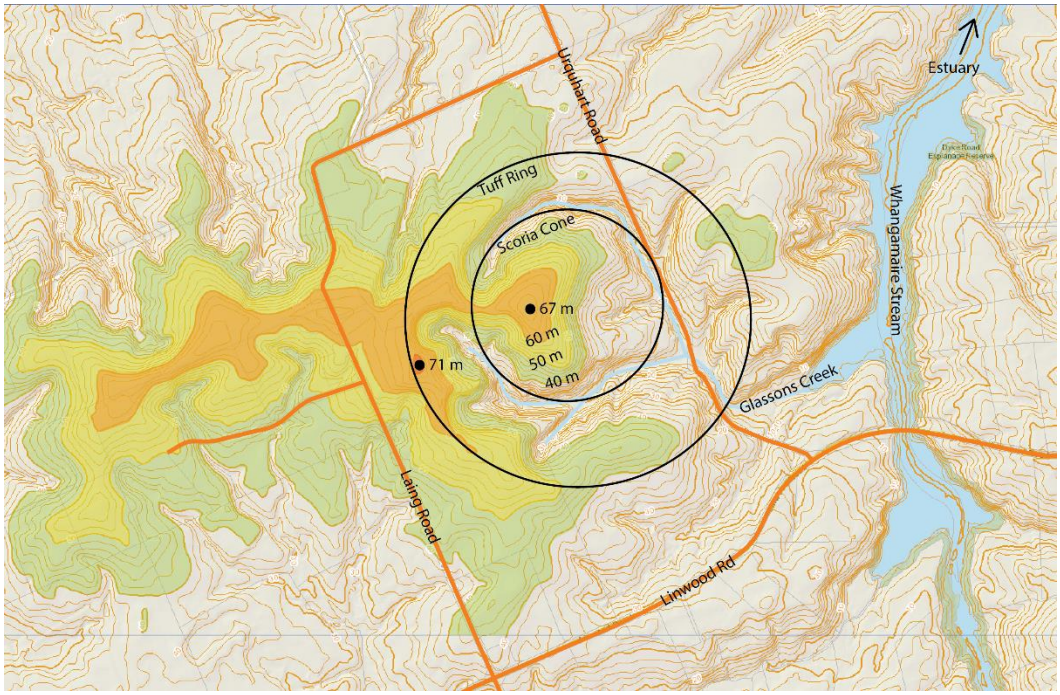

Figure 2.6: Topography of the landform in Karaka and stream pattern (Auckland Council, 2019).

The volcanic landform shown in Figure 2.7, houses a circular drainage system around the central cone within the tuff ring that drains into Glassons Creek to the southeast. Hayward (2018) suggested this tuff ring once housed a lake before a breach reduced the water level. The tuff ring is 1.1 km from crest to crest (Figure 2.6). Hayward (2018) also posed that this landform is likely of SAVF age, particularly as the Hamilton Ash mantles it. Faults in the area include the Glenbrooke Fault in the south and the Waiau Fault, roughly in line with Laing Road

in the north. These faults have created the Waiau Horst that this landform sits astride (Kenny *et al.*, 2012).

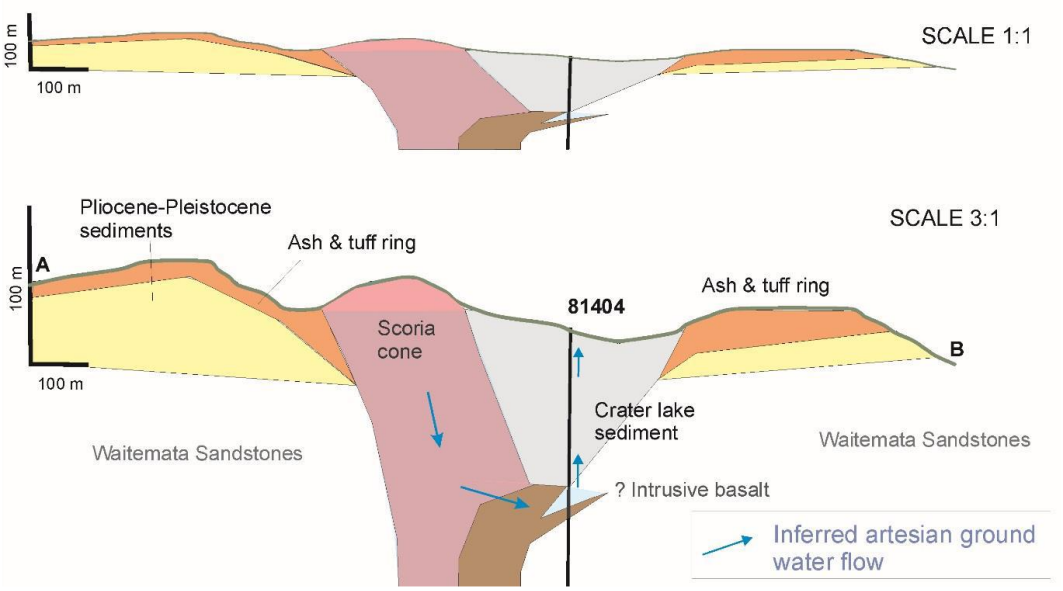

Figure 2.7: Inferred cross-section of the Karaka cone and tuff ring (Hayward, 2018) .

According to Edbrooke (2001), the potential Karaka cone overlies Pliocene to Middle Pleistocene pumiceous river deposits. Expected lithologies are pumiceous mud, sand and gravel with muddy peat and lignite, rhyolite pumice, including non-welded ignimbrite, tephra and alluvia. Nearer to the Manakau Harbour, Holocene river deposits are present which include sand, silt, mud and clay with local gravel and peat beds. Approximately 5 km to the south, basalts of the SAVF are present (Edbrooke, 2001).

Further evidence for the Karaka volcano is the change in elevation of the top surface of the Waitemata Group around the volcano (Hayward, 2018). Beneath Glassons Creek to the southeast of the volcano, exposures of the Waitemata Group are at the surface (16 m asl). Under the cone, the top of the Waitemata Group is found at 92 m below the surface. These variations in the top of the Waitemata Group may be caused by the eruption that created the tuff ring, evacuating volcanic material and causing a collapse in the overlying Waitemata Group.

The Waitemata Group was intersected during drilling of a water bore which gained artesian flow of groundwater at 110 m deep (Drillwell Exploration NZ Limited, 1996). This borehole was conducted 18 m asl and begun by retrieving organic clays from the surface to 71 m depth, which could have existed due to swamp or lake sediments residing within the tuff ring. Grey sands and traces of shells follow this to 110.84 m deep. Soft basalt was in the borehole between 110.84 to 123.6 m depth. Beneath this to the base of the borehole was sandstone and mudstone (248 m).

Only one outcrop of volcanic material (besides the overlying ash beds) was discovered, west of the cone in a weathered road cutting on Laings Road. This outcrop contains weathered tuff with a pinkish matrix containing some weathered lithic or scoria fragments. Material of this sort is generally found within 1 to 2 km of a vent, as such, this material must have come from a local source (Hayward, 2018; Vidanovich, 2018a).

Test pits conducted by Lander Geotechnical in 2016 at the end of the southern drainage arm of the cone, state that weathered tuff was encountered in test pits 3, 4, 5 and 7. Described tuff is orange, grey, red and brown, with inorganic silty clays and silty fine sands containing some medium gravel and silt inclusions with some limonite staining (Lander, 2016).

Further evidence of a volcano includes a magnetic survey carried out over the surface of the potential cone and tuff ring. An area of high magnetism (Figure 2.8) is present beneath the crest of the cone with another small area in the tuff ring to the east. These areas of high magnetism may be consistent with a basaltic plug within the cone, basaltic flows or basalt abundant debris. The potential plug is estimated to be at 75 to 250 m below the surface. Magnetic lows occur within the drainage areas surrounding the cone (Vidanovich, 2018b).

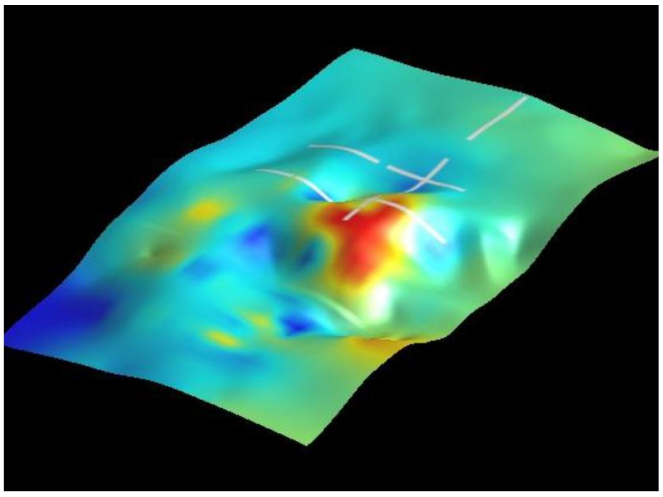

Figure 2.8: The magnetic intensity of an anomaly under the high point in topography, which may be a potential scoria cone (Vidanovich, 2018b).

Chapter 3

Field Geology and Subsurface Stratigraphy

3.1 Introduction

The Karaka Volcano does not lie within the current boundaries of either the AVF or the SAVF. Instead, it occurs near the Manakau Harbour on Puketoka Formation deposits (Edbrooke, 2001) and is approximately 5 km from the nearest volcanic landform of the SAVF. The nearest AVF deposit to Karaka is Matukutūruru in Wiri (31 ka) approximately 8 km away (Cassata *et al.*, 2008; Leonard *et al.*, 2017).

The topography around the Karaka District is subdued with an average elevation of 25 m asl. One area north of Linwood Road near Laing Road in Karaka has a much higher topography than the surrounding area, reaching 70 m asl.

Different monogenetic landforms have varying characteristics and include spatter cones, scoria cones, maar-diatremes and tuff rings/cones. Controls on the type of landform and its products include the underlying geology and manifestations of groundwater or surface water. Because of this, eruption styles and products may be dynamic, creating either one landform or a combination of several. These features generally create a recognisable topography in the landscape. Distinct landforms make the examination of topographic maps and digital spatial data, especially high detail lidar contours, useful tools for the identification of volcanic landforms. Over time, however, and dependant on the size of the volcanic feature, these landforms can be eroded or buried by younger deposits that are not associated with the land-forming eruptions—causing them to be challenging to distinguish from the surrounding landscape. This identification may also be made difficult by the presence of faulting in the area, which may further alter the topography.

Previous studies (Hayward, 2018) used topography, magnetic surveying, geotechnical test pits, literature and borehole data from the surrounding area to

indicate the presence of the Karaka Volcano. In this chapter, further field investigations such as subsurface drilling and a resistivity survey are presented to identify and characterise the volcano and its volcanic and sedimentary deposits.

3.2 Methods

3.2.1 Site investigations

The investigation into the Karaka Volcano began with a site walkover and examination of the site. A walkover of the site gave and an indication of topography, identified several outcrop locations, and found useful locations for further testing.

Minor tests conducted in the field include two hand augers on the potential scoria cone and some sampling of material at outcrops. More in-depth testing included two HQ drill holes and a resistivity survey. Test locations and outcrops are shown in Figure 3.1.

Hand auger sampling utilized a 2.2 m, 50 mm hand auger. These were conducted at two separate locations (Figure 3.1) to examine the depth and variations of cover beds. Hand auger one (HA1) was undertaken on top of the “scoria cone”, and hand auger two (HA2) was conducted on a steep flank section of the cone. Some samples were taken from each hand auger and stored at the University of Waikato.

Investigations also included describing a roadside cutting showing a succession of sand beds (SC1, Figure 3.1). Samples were collected using a spade.

The underlying basement Waitemata Sandstone is exposed in a stream at WSS (Figure 3.1) where it was sampled using a rock hammer.

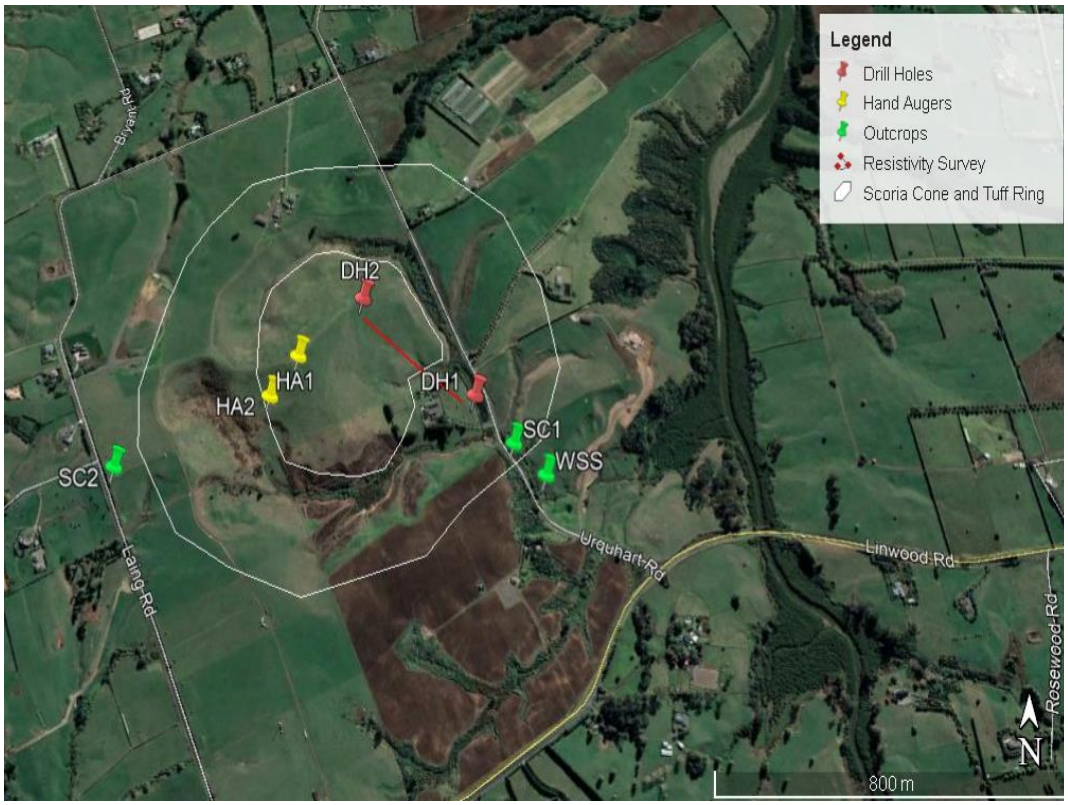

Figure 3.1: Site map and field locations of the Karaka Volcano (Google Earth Pro, 2019).

3.2.2 Core Drilling

Drilling was conducted on two, two-day sessions. The first drilling session took place on the 12th and 13th of December 2018. Here lake sediments were targeted, and drilling reached a depth of 13 m. The second drilling session took place on the 29th and 30th of May 2019 and reached a depth of 16 m into volcanic material.

The University of Waikato's trailer-mounted hydraulic drilling rig (Figure 3.2) was used on both drill sites. The drill uses a direct circulating-mud rotary drill system with an inner continuous core-sampling barrel. Hollow rods are used with a drill bit at the end and drilled into the ground with drilling fluid pumped into the rods. Drilling mud provides lubrication, increases sampling success and keeps parts of the drill rig cool throughout drilling. Once drilling was completed for every 1.5 m long rod, extraction of the 63.5 mm (HQ) core barrel occurred, and the sample was removed and stored in core boxes.

Recording of core loss and depths of sampling happened in 1.5 m increments. DH1 experienced approximately 2.5 m of core loss, and DH2 had approximately 4 m of core loss. The core was stored in PVC tubing and sealed in plastic sleeves using a heat sealer. The wrapped cores were then stored and labelled in a cardboard box and taken to the University of Waikato.

Figure 3.2: The drill rig and processing set up for DH1 in Karaka. The drill rig is operating on a low point within the tuff ring with water tanks and processing tables behind it.

Cores prepared for analysis were split in half using a wet tile saw. Half sections were not entirely even due to the nature of the improperly cut PVC tubes and the cutting mount used. Once cut and cleaned, to remove excess mud and PVC tubing shreds, the separate halves were wrapped in cling wrap and heat-sealed in plastic tubing and stored in the core box as either “archive” or “working”.

In the field, a brief core log was created before more extensive logging was conducted on the working cores. Core logging in the laboratory involved visual description of colour, structure, texture and visible components. Sampling occurred from different layers, zones and discrete clasts for further analysis. Photographs were also taken before re-wrapping in cling wrap and plastic sleeves, and placing them back into their box for refrigerated storage.

3.2.3 Resistivity Survey

A resistivity survey over the Karaka landform aligned approximately between the two drill holes to investigate the underlying geology to a greater depth. The survey line (Figure 3.3) was selected so that it intersected both the slope of the central "cone" and the adjacent proposed lake terrace and would link the two drill holes together. The survey used an AGI SuperSting R8 with a switch box, 28 electrodes and an electrode cable.

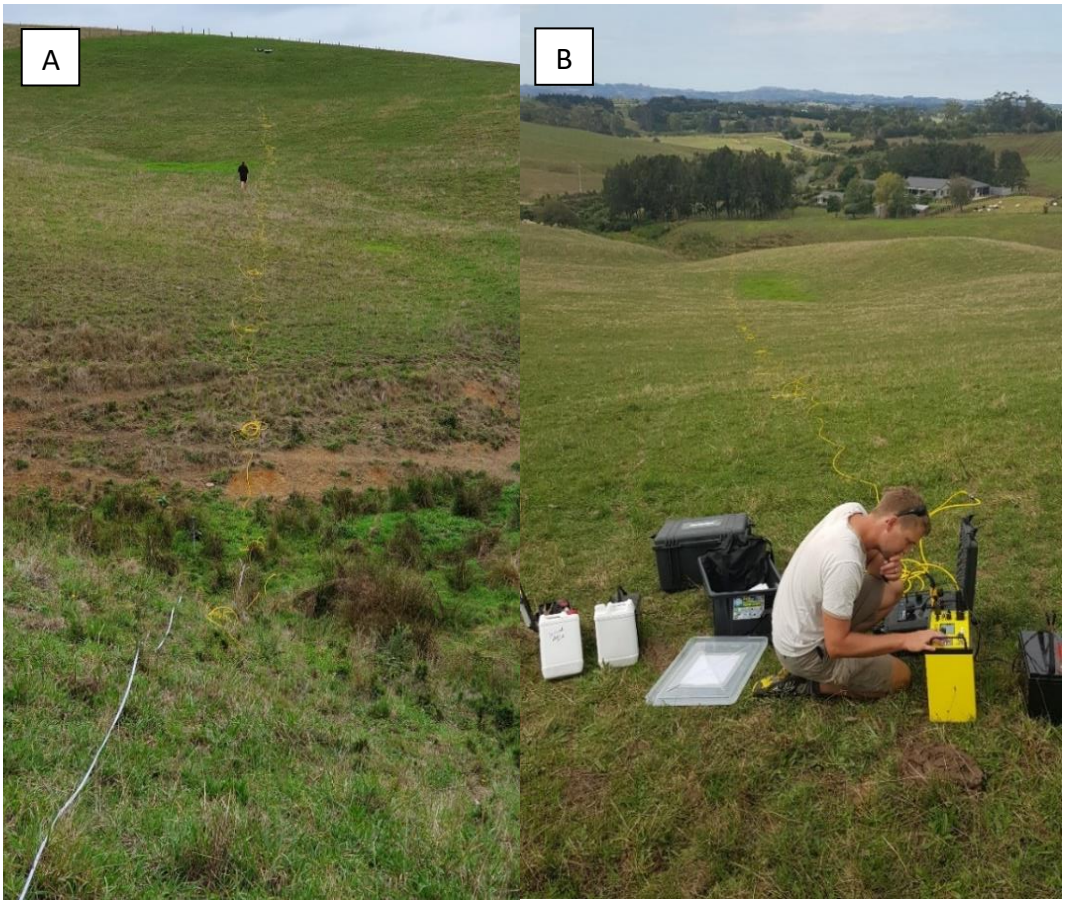

Figure 3.3: (A) Looking towards the northwest up the slope of the cone. (B) Looking downslope towards the southeast from the control box.

The total line length surveyed was 324 m, with a maximum electrode spacing of 20 m and a 2 x 25% rollover, where a quarter of the electrodes were moved from the start of the survey line to the end of the line to extend the length of the survey. The array type was dipole-dipole with gradient, and the intended electrode spacing was 8 m. Inversion of the data was done with AGI EarthImager 2D. The resulting data was then aligned with GPS points to assign topography.

3.3 Subsurface Ground Investigation

3.3.1 Drill Hole 1 (DH1)

The location of DH1 was selected to target a potential crater lake succession which had been suggested by the presence of organic sediments in a borehole and also basalt at depth in this location (Drillwell Exploration NZ Limited, 1996). This water bore stated that 'organic clays and grey-brown silts' were present from 6-71 m below the surface. 'Soft basalt' was found 110.84-123.6 m below the surface. 'Rock' was first encountered at 92 m below the surface and shells were found between 21-92 m. The depth to the underlying Waitemata Group noted in the water bore was considerably deeper here (92 m below the surface) than at Glasson's Creek 100 m to the southeast, where it outcrops at the surface.

DH1 was 13 m deep, and a simplified log is shown in Figure 3.4. Three key depositional packages were classified: the cover ash beds (0 - 5.7 m); a transitional package (5.7-7.4 m); and lastly a lacustrine or paludal depositional package to the base of the drill hole (Figure 3.5).

The cover ash beds are comprised of massive to laminated pale yellow to light grey clays, with red mottles until 5.7 m depth. The upper part is a massive yellow-orange clay with minor sand grains that transitions to a pale-yellow clay with red mottles. Some clay horizons also contain woody material in vertical veins. At some depths, these ash beds appear to have weathered pumice inclusions that crush easily. Near the base of these clay beds, are red or dark brown laminations.

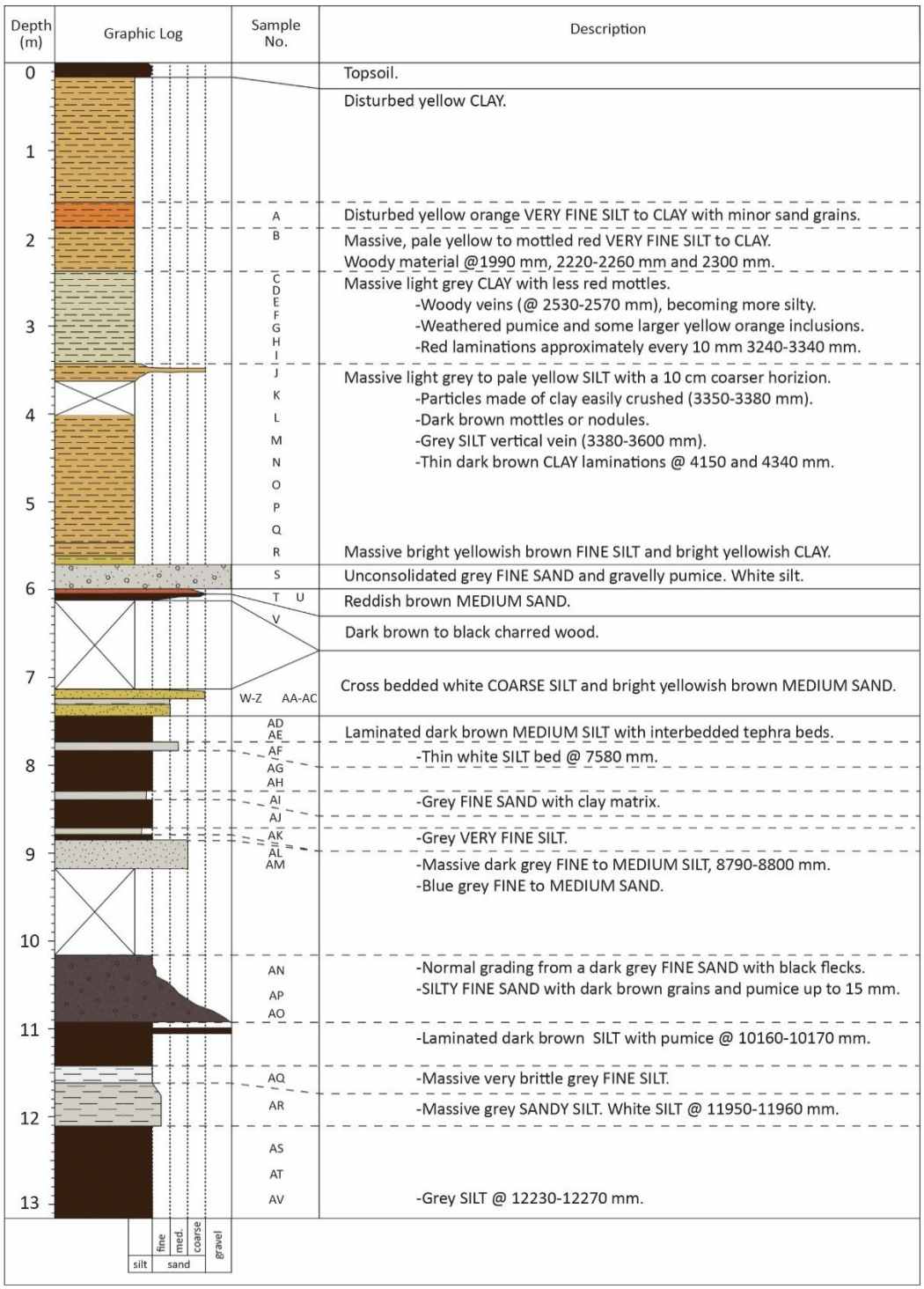

Figure 3.4: Simplified DH1 log. Each of the three depositional phases can be seen within the drill log. Light grey and orange clays span from the surface to approximately 5.7 m. Organic sedimentary deposits range from 7.4 to 13.2 m beneath the surface. Between the two are sediments that do not fit into either (as well as some core loss), these sediments include sand and charred wood.

The transitional package comprises alternating sedimentary beds of bright yellowish clay, a light grey pebbly and sandy pumice layer, white silt, coarse red

sand and a layer of dark brown to charred black wood. Beneath the woody layers are interbedded white silts and bright yellow sands, with some iron staining.

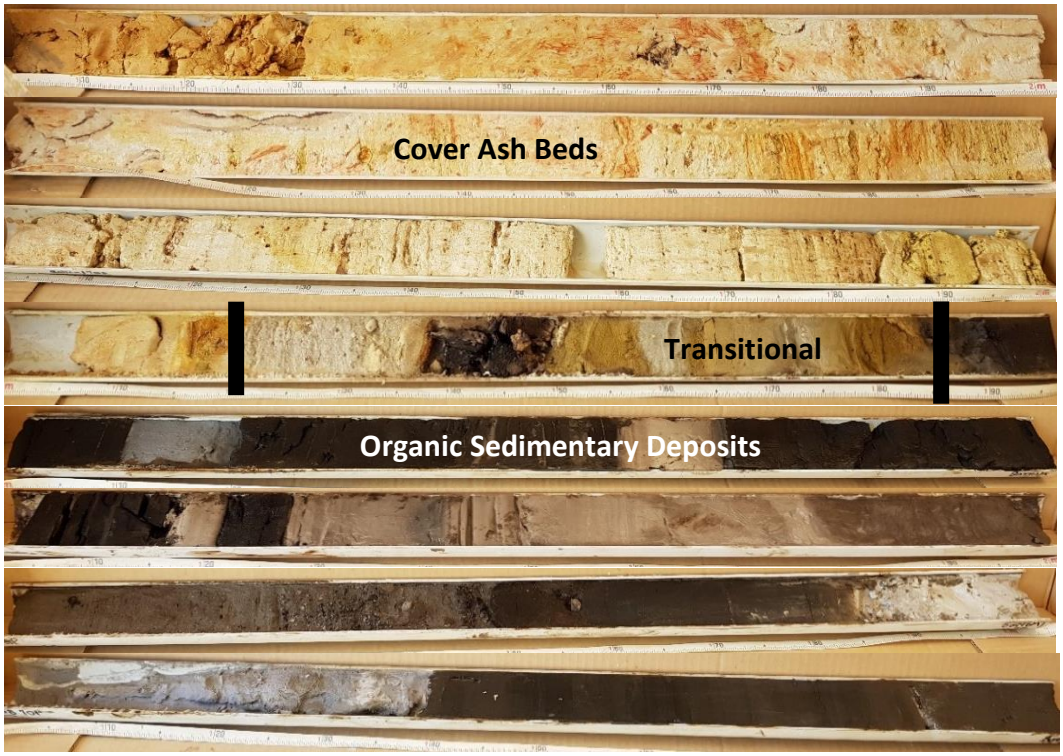

Figure 3.5: Sediments retrieved from DH1. The grey and orange clays near the surface are representative of cover ash beds. Easily distinguished from the two cover packages are the basal organic sedimentary deposits interbedded with various tephras.

The lower package (7.4 – 13.2 m) is predominantly dark brown to black laminated silt. The laminations in these layers are approximately 2-5 mm thick. Between some of these layers are thin grey beds that range between 2-10 mm thick. Some grey deposits dispersed within the brown laminated sediment are thicker; however, (approx. 10 cm thick) and are comprised of varying grain sizes, including sand and clay. There are two more extensive grey deposits within this succession, including one that begins as a dark grey fine to medium sand and that has a gradual transition to dark grey silt with fine sand. The second contains a black material that becomes coarser with depth and contains pumice (15 mm). Beneath this is another thicker tephra described as a very brittle grey to white silt that is approximately 60 cm thick. Near the base of the core, the sediments become harder and more challenging to drill through.

3.3.2 Drill Hole 2 (DH2)

The location of DH2 was on one of the high points of the potential cone in an attempt to intersect the pyroclastic cone deposits. A simplified log of DH2 is shown in Figure 3.6. The recovered drill core is displayed in Figure 3.7.

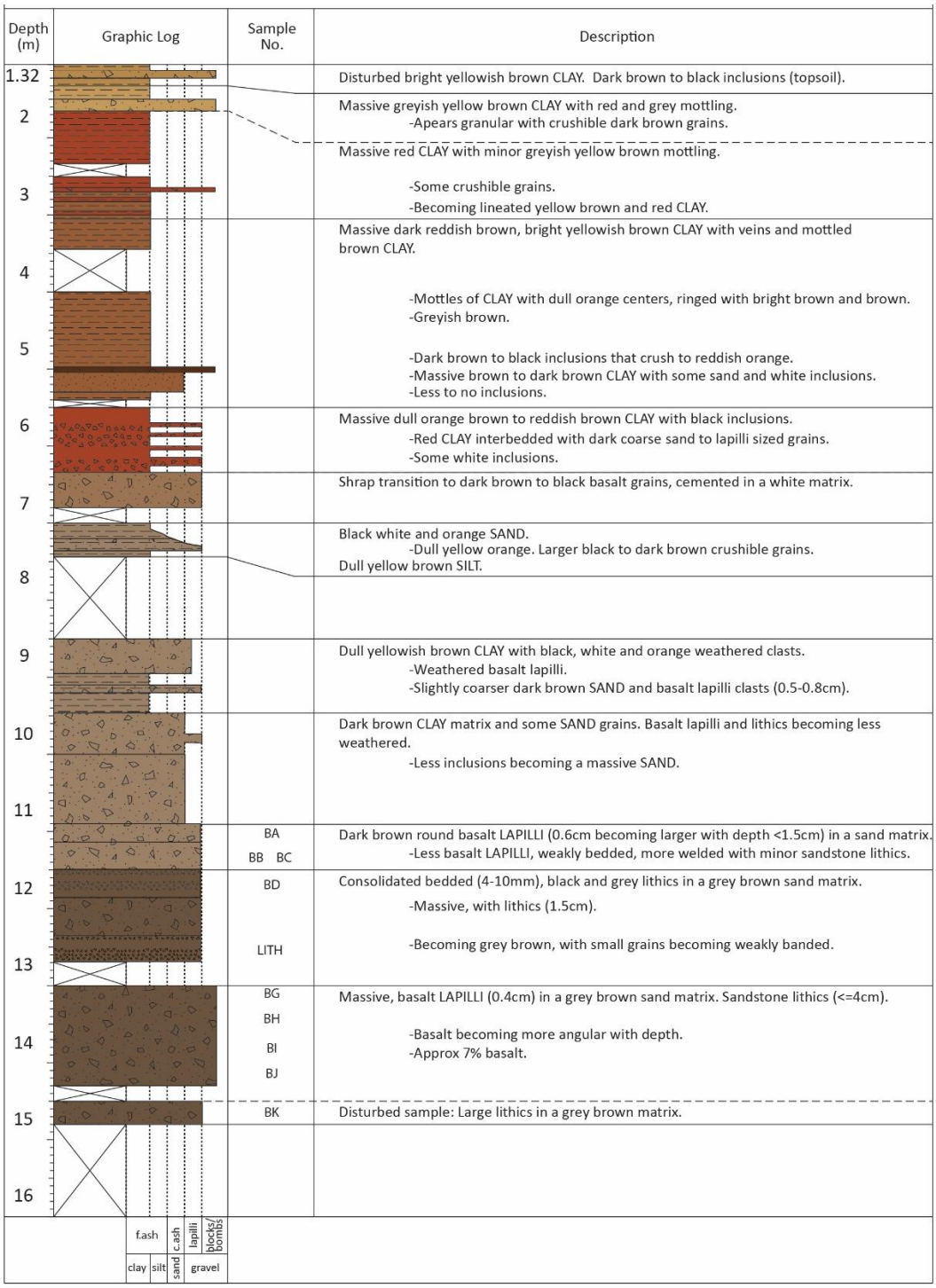

Figure 3.6: Drill log of DH2. This log displays red cover ash beds to 6.5 m deep and beneath it, a tuff deposit with dark brown basalt lapilli in the sand to the clay-like matrix.

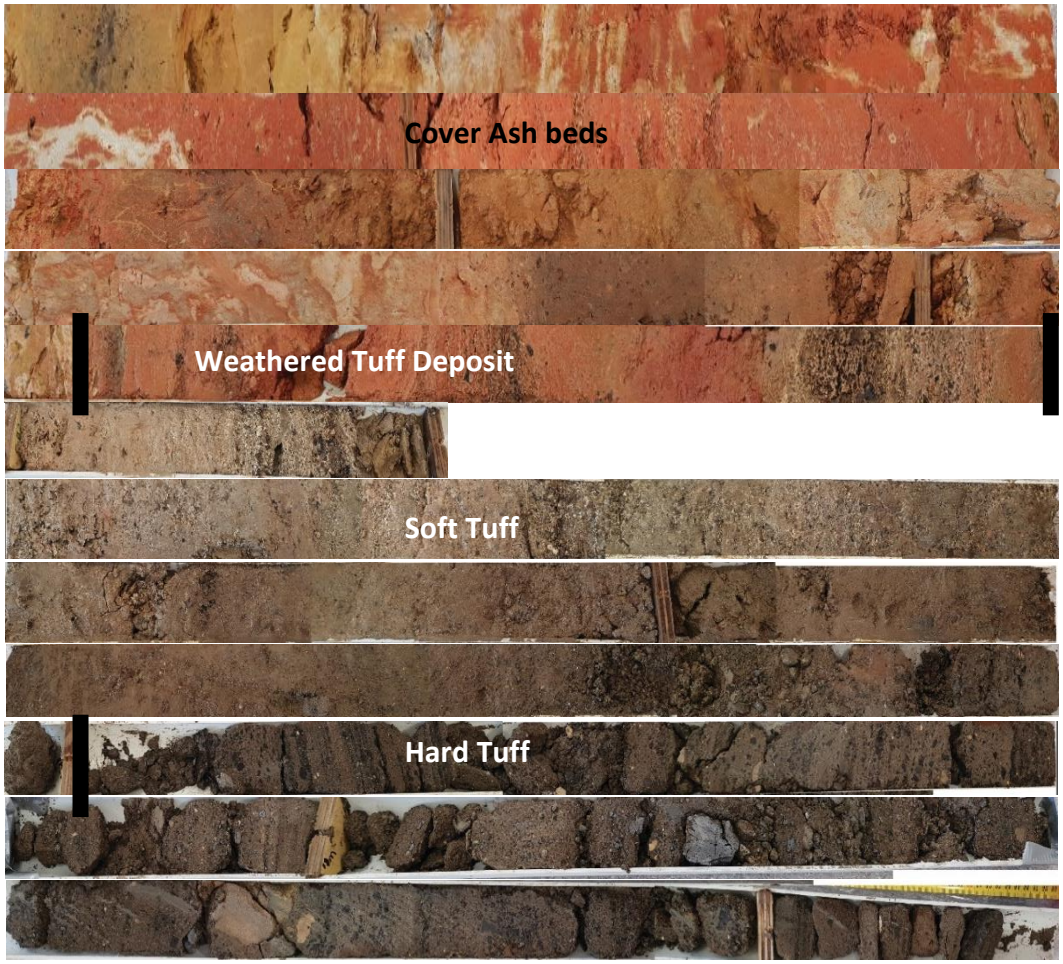

Figure 3.7: Material retrieved from DH2. The cover beds here are a different colour to those in DH1. Several sections of clay are interspersed with weathered basaltic material. Beneath the red clay is a grey matrix with basalt lapilli and lithics. The core material becomes consolidated near the base.

The material retrieved from the top of the core began as yellowish clay with some small black inclusions, likely to be topsoil. Yellow clay transitioned into a grey clay with some red laminations before becoming a massive red clay with some grey clay veins, and minor brown grains also present. At around 2.5 m the clay starts to become a brownish-red clay with some light brown veins. This clay then develops a mottled appearance with grey clay sections with red rims in a matrix of grey-brown clay (50 cm). The colour of this clay changes to dark brown with sand-sized brown inclusions for 50 cm before reverting to red clay with some sand grains. Within the next metre of red clay, there is a 10 cm thick layer that contains black crushable grains of possible weathered scoria lapilli.

Approximately 20 cm below this (7.5 m below the surface) there is a sharp transition into a much lighter coloured material containing weathered basalt lapilli. Between 8 and 9 m core was not recovered, but below 9 m the lithology is consistently similar containing dark brown fine or coarse ash with some basalt lapilli and lithics. Below 12 m the material becomes consolidated and shows distinct bedding and hard fresh basalt lapilli. Lithics in this part of the core are silt or sandstone; however, they are very soft and break easily. The most significant basalt piece found was a small bomb 5 cm in diameter and was a similar size to the largest lithic found (Figure 3.8).

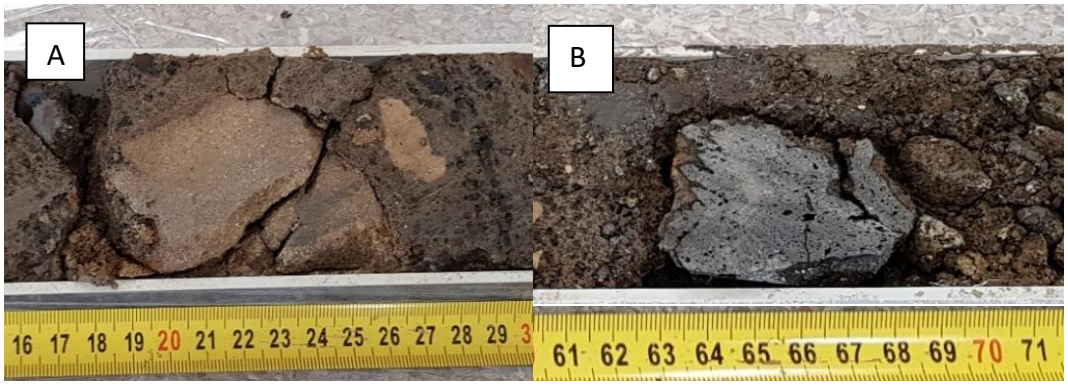

Figure 3.8: (A) A lithic fragment brought up in DH2. (B) A basalt bomb found in DH2.

3.3.3 Hand Auger Samples 1 and 2 (HA1 & HA2)

HA1 and HA2 are complimentary to DH2 and show the topsoil at this location to be between 100 and 200 mm thick, underlain by a brown clay mottled red, with white flakes (silica) and containing mica to 2 m deep (Figure 3.9). These ash beds are inferred as the Kauroa Ash.

Figure 3.9: HA1 and HA2. These hand augers display the variation in cover clay beds over a small distance.

3.4 Field Outcrops

Described below are three key outcrops.

3.4.1 Road cutting, Urquhart Rd, SC1

On the Urquhart roadside to the south-east of DH1 is a small outcrop of bedded sand. The outcrop is 2 m high at 18 m asl and ranges from whitish-yellow fine sand through to greyish brown fine sand and fine brown sand at the base (Figure 3.10). Several layers within the log show orange banding and some white silt lenses (Figure 3.11).

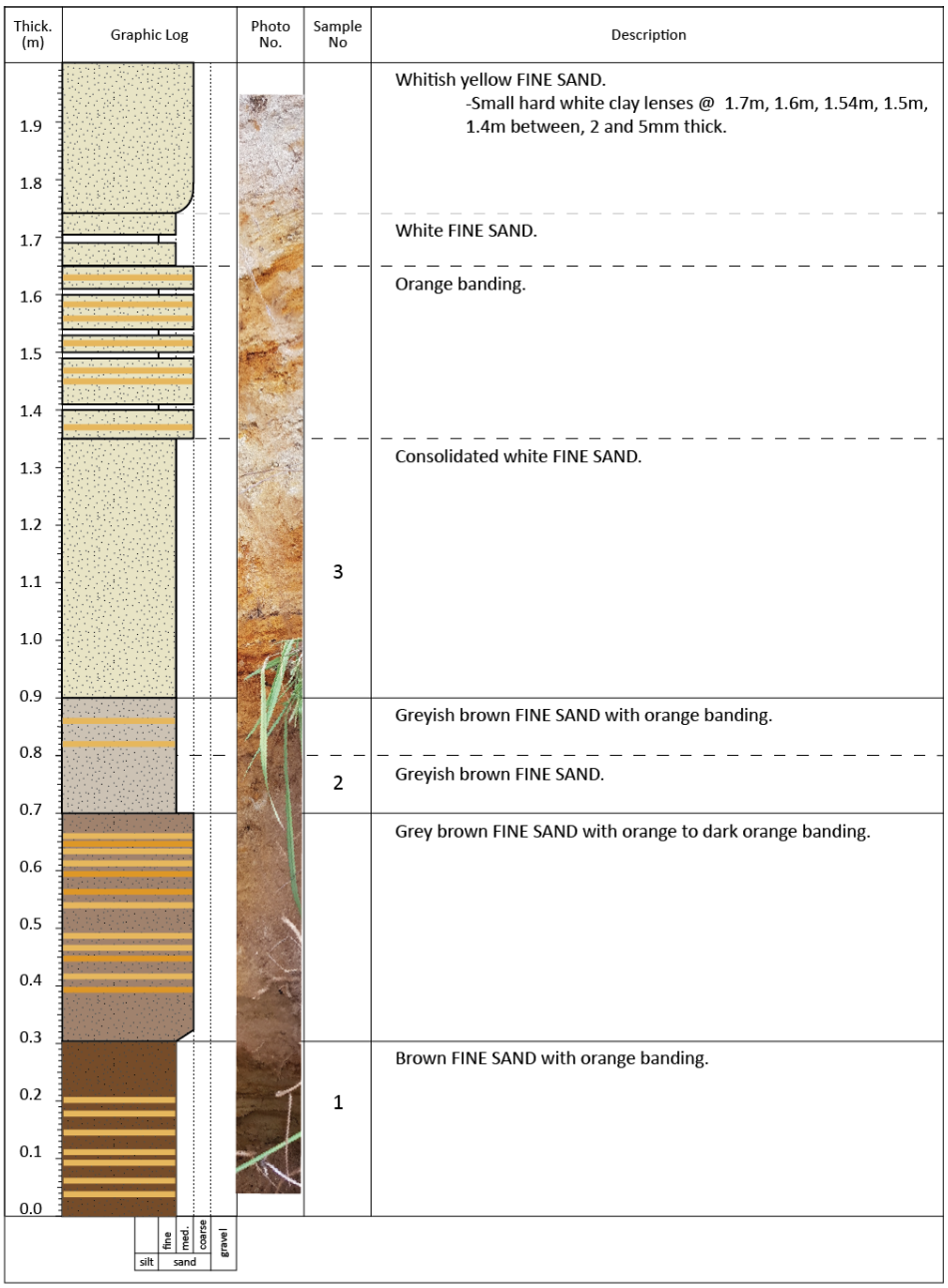

Figure 3.10: A stratigraphic column of a roadside sand deposit, potentially of the Puketoka Formation. This is very different from all of the material discovered in drill core.

Figure 3.11: Sand outcrop displaying on the Uquharts roadside. Showing differing material to that discovered in the drill core.

3.4.2 Roadside swale cutting, Laings Rd, SC2

On Laings Road, there is a roadside swale which cuts into the proposed tuff ring, allowing the exposure of a weathered tuff deposit. There were two lithologies observed: red and light brown clay, (Figure 3.12) and orange to red clay containing weathered brown clasts, possibly weathered basalt lapilli. A hand auger into the roadside tuff uncovered material consistently similar to 1.5 m depth.

Figure 3.12: Weathered tuff found in a roadside swale. This image displays two distinct tuff patterns. Above is the layered red and grey clay and beneath is the orange to red clay with light and dark brown inclusions potentially of basalt lapilli and lithic material.

3.4.3 Glassons Creek bed, WSS

An exposed section of the Waitemata sandstone of the Waitemata Group is at the surface in the bed of Glassons Creek 100 m south-east of DH1. The Waitemata Group is an interbedded, graded sandstone and siltstone or mudstone (Edbrooke, 2001).

3.5 Resistivity Survey

Several interpreted geophysical units are present in the inverted resistivity section (Figure 3.13). Unit 1 is at the surface, ranging from 2 to 10 m deep and has a

resistivity range of 50 to 107 Ω-m. This layer becomes deeper towards the southeast of the section and may represent the overlying clay beds of either the Hamilton or Kauroa Ash.

Unit 2 lies beneath Unit 1 and ranges from 10 to 30 m thick. This layer has a higher resistivity than Unit 1 ranging from 76 to 251 Ω-m, and is not continuous, with areas of both high and medium resistivity values. Unit 2 is likely to correlate to the basalt lapilli tuff succession, observed from 7.5 to 16 m within the DH2 drill core. To the southeast along with the resistivity profile, there are two segments of similar resistivity in line with Unit 2, however, slightly disconnected, it is undetermined if they correlate.

Beneath Unit 2 is the variable Unit 3 ranging from 14.5 to 30 m thick and with resistivities between 76 and 23.2 Ω-m. At the northwest end, this unit has a much lower resistivity than at the southeast where it is underlain by Unit 4.

Unit 4 is the lowermost unit (Figure 3.13) and consists of a small area around 18 m deep with a high resistivity of between 74 and 195 Ω-m. A magnetic survey of the area proposed a basaltic plug 80 m below the surface in this area, which may correlate with this unit (Vidanovich, 2018b). Units 3 and 4 occur below the depth reached by DH1 and DH2, so their lithology is not confirmed.

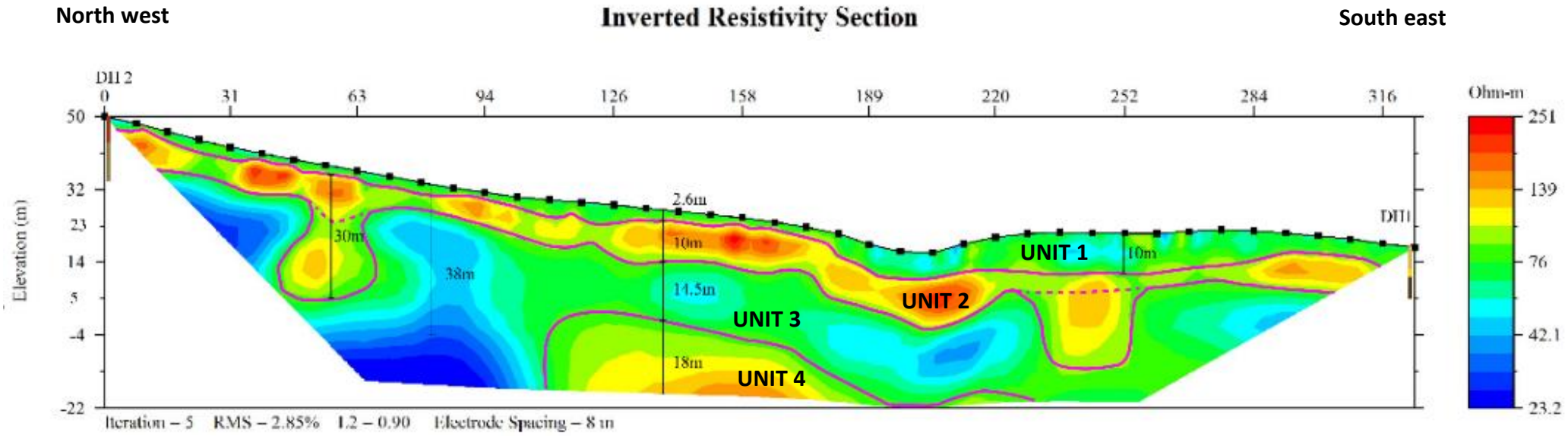

Figure 3.13: Inverted resistivity survey conducted in Karaka. The top unit (Unit 1) ranges in depth from 2 to 10 m thick and appears in green. The second deeper layer (Unit 2) is generally 10 m thick; however, has two areas where it deepens to approximately 30 m thick, this is shown in reds and oranges. The third layer (Unit 3) has a lower resistivity and ranges from 14.5 to 38 m thick, seen in blues and greens. The last unit (Unit 4) seen is at the base of the sections, and its thickest is around 18 m thick, visualised in yellow to orange.

Chapter 4

Basaltic pyroclastic sequence of the central hill

4.1 Introduction

DH2 at Karaka provided fresh basaltic material into the investigation of the Karaka Volcano, allowing for a better understanding of the volcanic processes at play. Basalt retrieved from the core has been prepared into thin sections, for microscopic petrography, as well as mineral chemistry. Bulk rock powdered samples were used for x-ray fluorescence (XRF) spectrometry and x-ray diffraction (XRD) analysis to gain more information on the whole rock composition, and mineralogy.

As Karaka lies between both the SAVF and the AVF, which vary in whole-rock chemistry, these analyses can help determine which volcanic field this volcano belongs to. Basalts of the SAVF can also belong to one of two compositional groups: Group A or Group B (Cook, 2002), which are distinguished by their geochemical compositions.

Group A consists of several different types of basalt including alkali olivine-basalts, transitional basalts, hawaiites, olivine-tholeiitic basalts and quartz-tholeiitic basalts. These are generally hypersthene normative with subalkalic compositions and are relatively low in high field strength elements (HFSE) such as Nb (9-29 ppm) Zr (97-219 ppm) (Cook, 2002).

Group B consists of alkali olivine-basalts, nephelinites, basanites, nepheline-hawaiites and mugearites. They are nepheline normative with alkali compositions and are relatively high in HFSE such as Nb (35-102 ppm) and Zr (194-491 ppm) (Cook, 2002).

4.2 Methods

4.2.1 Thin Section Preparation

Six basalt lapilli samples, three matrix and one lithic sample from several different depths of DH2 were prepared by setting into resin blocks. These resin blocks were ground down using a grinder and polished on a glass plate. Preparation of the matrix and a basalt block required surface impregnation. Once impregnated they were ground on a glass plate to remove the resin. The polished surface was mounted on a frosted glass slide with Hillquist thin section resin. Once the resin had set the excess block was cut off. The remaining rock was ground using a Struers Discoplan-TS until the slide was the correct optical thickness for viewing. Thin sections were either polished for the EPMA, or a coverslip was placed over the sample using petropoxy 154, for petrology.

4.2.2 Optical Microscopy

The polished and coverslipped thin sections were examined using a petrographic microscope. Crossed and plane polarised light was used to identify minerals and textures within the sample. Quantitative data was gathered on mineral abundancies using point counting. A stage interval was set at 0.2 mm, and 200 points were counted per slide. As lapilli in the thin sections were discontinuous, sample available for analysis was limited.

4.2.3 X-ray fluorescence spectrometry (XRF)

XRF spectrometry was used to identify major and trace element amounts of three basalt samples. Large rock samples were not available, so basalt lapilli was sieved out of the core and matrix material was ground off of the sample to minimize contamination. The clean basalt lapilli were then crushed into a powder using a tungsten-carbide ring mill.

LOI was determined by recording the weight of a ceramic crucible, then adding approximately 1 g of sample and recording the final weight. The crucible was placed in a furnace and heated to 1100 °C for 1 hour. Once this heating process

was complete, the sample was removed and reweighed to find the LOI. This weight was recorded.

The geochemical analysis was done using the Bruker S8 Tiger XRF machine at the University of Waikato. Major element compositions were measured using glass fusion beads which were made using 0.8 g of powdered sample with 8 g flux (lithium meta-tetraborate). This mix was heated to 1050 °C for 20 minutes. The molten sample was poured into a mould and cooled slowly to avoid cracking.

For trace element analysis, pressed pellets were made using 8 g of rock powder mixed with 25 drops of PVA. This sample was pressed using a hydraulic press and left to dry in an oven at 70 °C.

4.2.4 X-ray powder diffraction (XRD)

XRD was used to identify minerals within the sample. This was carried out on powdered whole-rock samples, made using the ring mill. Powdered samples were pressed into pellets and inserted into the Panalytical Empyrean XRD in the Faculty of Science and Engineering, at the University of Waikato. Data gathered was analysed using Highscore Plus to identify mineral peaks.

4.2.5 Electron Probe Microanalysis (EPMA)

Mineral compositions were analysed by the JEOL JXA-8230 EPMA at the Victoria University of Wellington. Major elements were identified using an accelerating voltage of 15 kV, a current of 8 nA, peak/background count times of 30 s/15 s, and was standardised using natural and synthetic compounds. The focused beam was standardised against plagioclase, kakanui (pyroxene), hypersthene, spring water, magnetite and ilmenite.

4.3 Pyroclastic sequence

The pyroclastic drill hole (DH2) begins displaying pyroclastic material (other than the cover ash beds) at approximately 5 m deep. This material is crushable and dark brown, possibly weathered basaltic lapilli. These become more frequent with

depth and less weathered. Pyroclastic material in the core is predominantly lapilli in size. Lithics become present at approximately 6.5 m depth. The Kauroa Ash is inferred to extend to a depth of 6.5 m. Beneath this, the material becomes tuff like, and houses weathered pyroclastic material in a white matrix, much of which is very weathered and soft. At 11.5 m depth the drill core becomes much harder and the pyroclastic lapilli within it, is fresh and extractable, the lithics remain highly weathered.

4.4 Petrography

4.4.1 Basalt Lapilli

Fresh basalt lapilli recovered from DH2 were homogenous in texture. Recovered lapilli were dark grey and included small red flecks of iddingsite. Under the thin section (Figure 4.1), lapilli were found to be approximately 15% vesicular, with an average vesicle size of 162 µm. Lapilli were porphyritic with a trachytic to glassy groundmass.

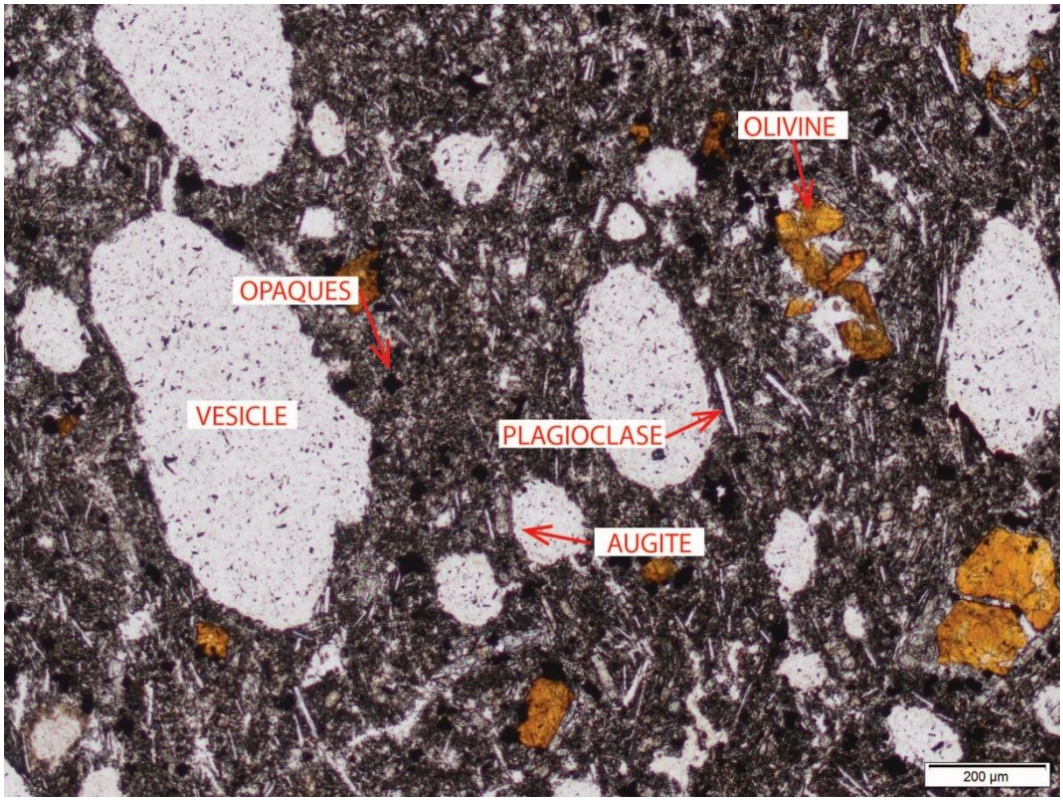

Figure 4.1: General mineralogy and texture of Karaka basalt under plane polarised light.

The point count conducted, as seen in Table 4.1 showed prevalent phenocrysts are olivine, augite and opaques, while plagioclase is a micro phenocryst. Phenocryst abundances ranged from 6.2 to 9.5% with a fine-grained, variably intergranular, intersertal, trachytic and hyalopilitic groundmass consisting of glass, plagioclase, augite and opaque minerals.

Table 4.1: Point count results from basalt lapilli from Karaka, DH2.

Phenocrysts	
Olivine (%)	9.5
Opaques (%)	7.3
Augite (%)	6.2
Groundmass and Microlites	
Groundmass (%)	54.8
Feldspar (%)	4.2
Unresolved Minerals (%)	0.2
Structures	
Vesicles (%)	14.8
Plucked out (%)	1.3
Lithics (%)	1.7
TOTAL (%)	100.0
TOTAL PHENOCRYSTS (%)	23

4.4.2 Phenocrysts

4.4.2.1 Olivine

Olivine is the dominant phenocryst, as seen in Figure 4.2. Olivine had an abundance of 9.5% in the point count and was euhedral to subhedral with a general orthorhombic shape. These crystals range in size from 15 µm to 712 µm with an average size of 144 µm.

Several large crystals have altered to iddingsite on their rims or along cracks. Several grains appear to have altered to iddingsite completely (Figure 4.2b). Some olivine grains were poikilitic, with smaller augite or plagioclase crystals within them.

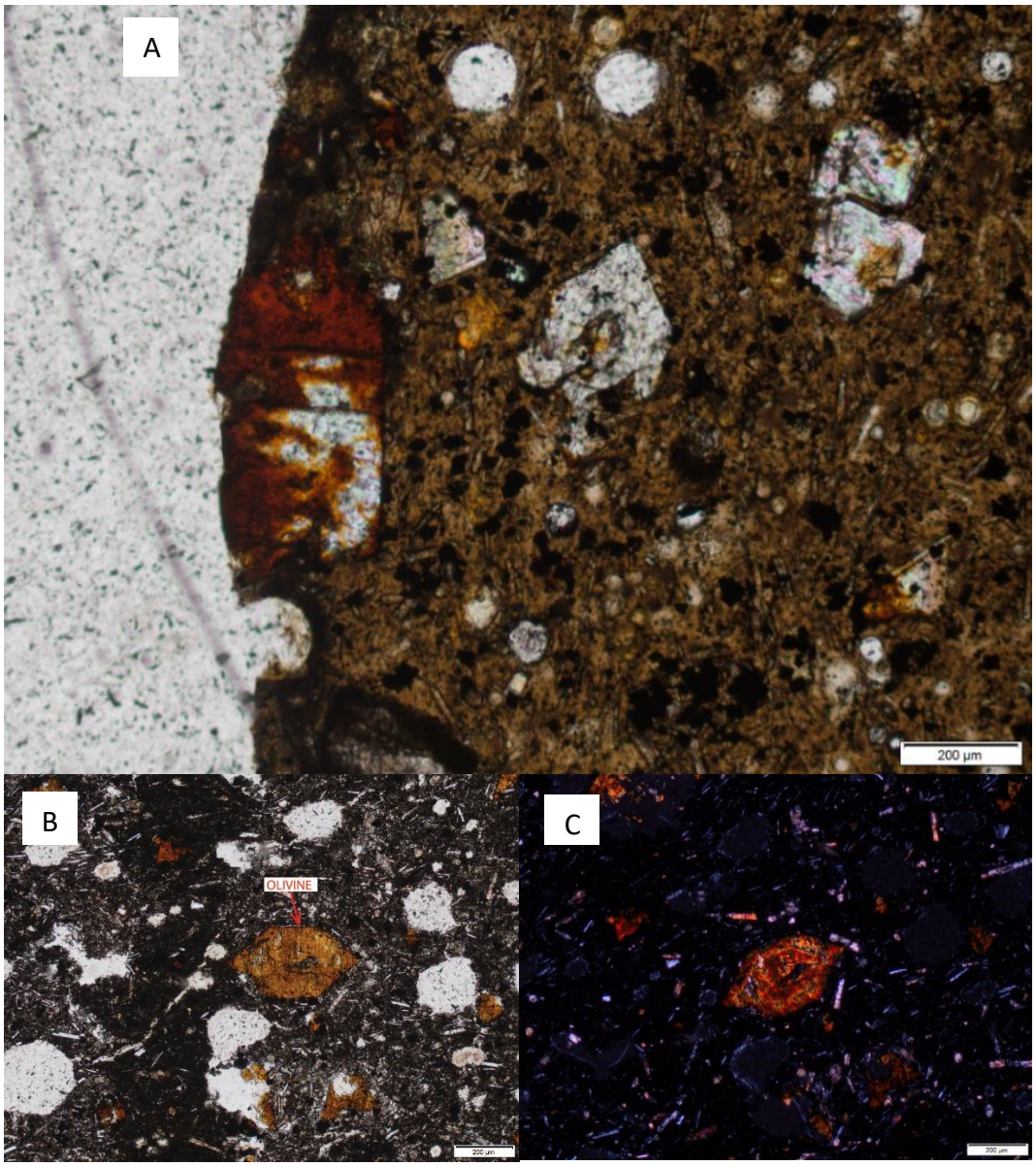

Figure 4.2: A) Olivine shown with iddingsite rims. B) Iddingsite pseudomorphs alter olivine in plane polarised light and C) in cross polarised light.

4.4.2.2 Opaque Minerals (Fe-Ti Oxides)

Opaque minerals (Figure 4.3) were abundant as phenocrysts as well as in the groundmass. They range in size from 17 to 86 µm and had an average size as phenocrysts of 45 µm. Opaque minerals were generally euhedral in shape. Opaques make up 7.3% of the basalt material.

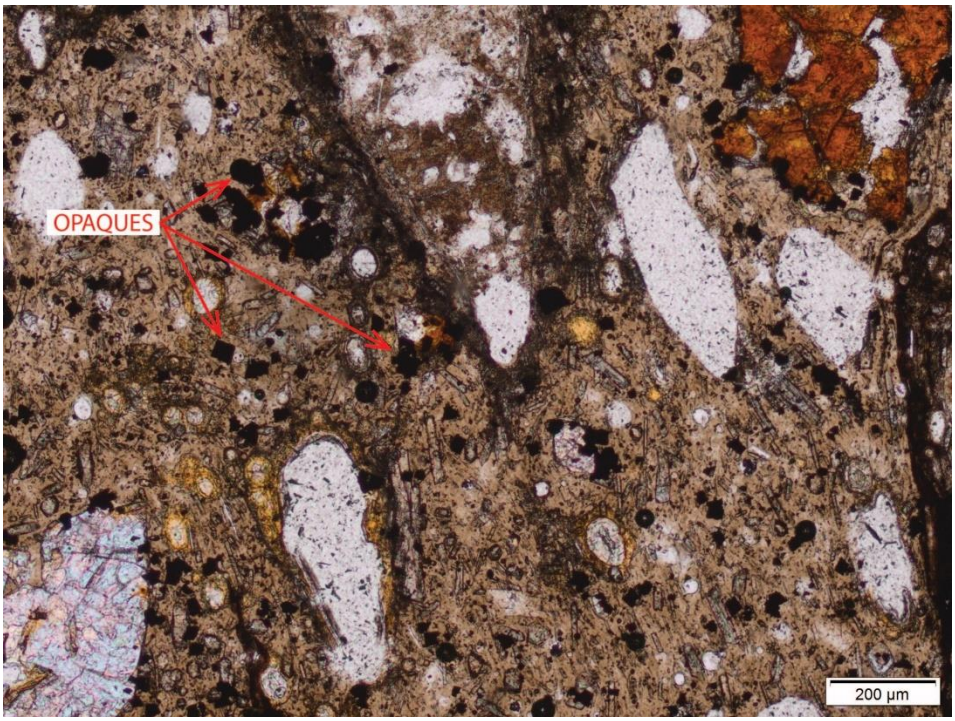

Figure 4.3: Opaque minerals under plane polarised light in thin section.

4.4.2.3 Augite

Augite (Figure 4.4) was one of the predominant phenocrysts subordinate to olivine in thin sections comprising 6.2% of the point count. These crystals were amongst the largest in thin section and subhedral in shape. They ranged in size from 40 µm to 418 µm with an average size of 130 µm. Some of these formed glomerocrysts and showed high interference colours in thin section.

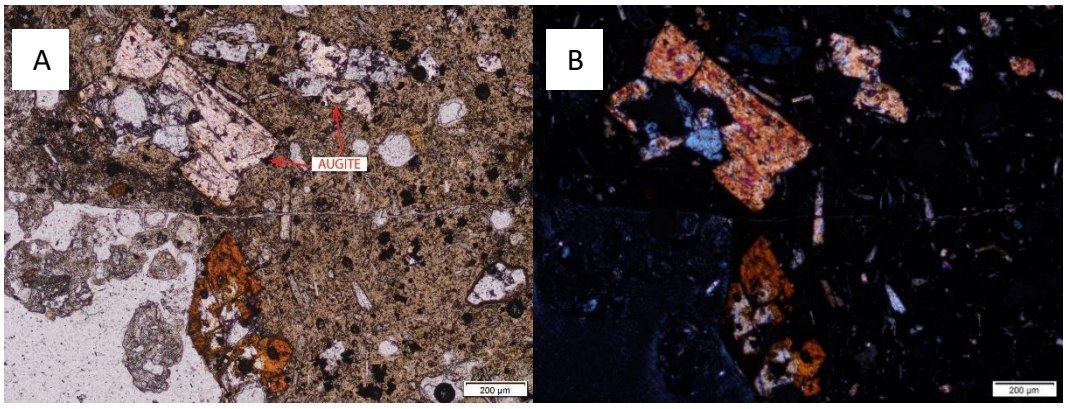

Figure 4.4: Augite in thin section under (A) plane and (B) cross polarised light.

4.4.3 Groundmass Texture

The groundmass of Karaka basalt is glassy and made up of many different microcrysts, including opaque minerals, olivine, augite and plagioclase. Two main groundmass textural types could be seen within the Karaka basalt. Figure 4.6A shows a crystal-rich matrix, whereas Figure 4.6B shows a glass rich matrix, from a basalt scoria lapilli.

4.4.3.1 Plagioclase

Plagioclase (Figure 4.5) was generally found as part of the groundmass and were much smaller than other phenocrysts. These crystals have a proportion of 4.2% in thin section and had a tabular shape. These were found to have an approximate minimum length of 41 µm, a maximum length of 126 µm, and an average length of 76 µm.

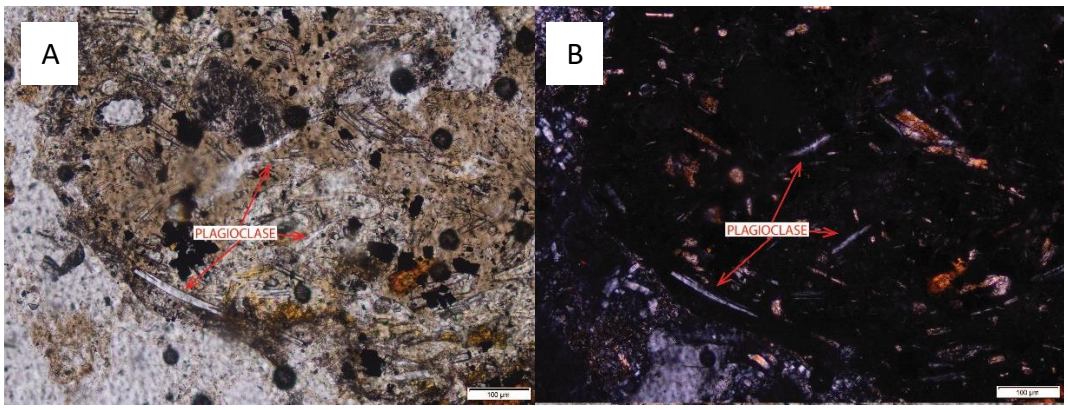

Figure 4.5: Plagioclase under (A) plane and (B) cross polarised light.

4.4.3.2 Glass

Glass differs depending on the sample investigated but is generally sideromelane as viewed in Figure 4.6. Within a thin section of a basalt-bomb, the glass is clear to light brown and is half glass and half crystal. In lapilli basalt, the groundmass is predominantly brown glass.

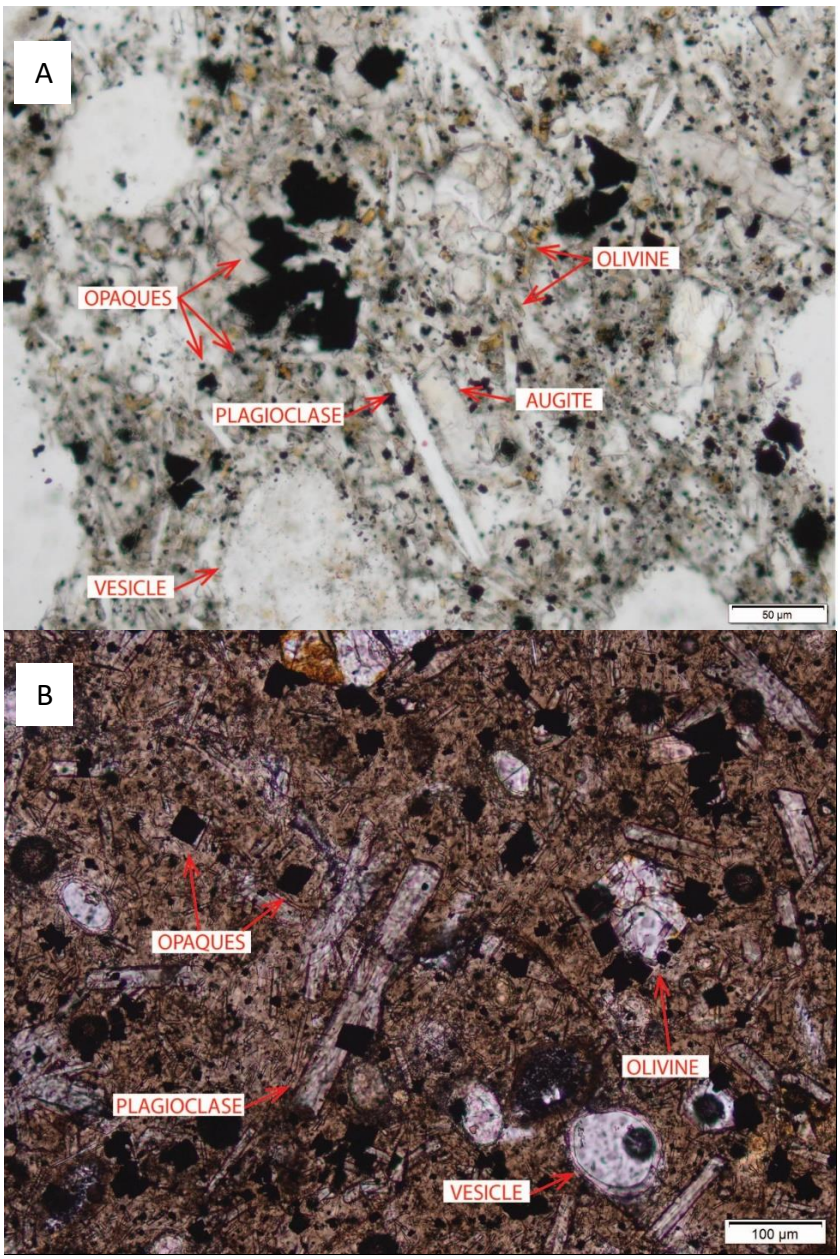

Figure 4.6: (A) Groundmass of a basalt sample, with a microlite-rich groundmass including olivine, opaque minerals, augite and plagioclase. Phenocrysts of each of these minerals are also pictured. (B) Glassy groundmass, showing brown glass with small microcrysts interbedded within it.

4.4.4 Zeolites

Zeolites (Figure 4.7) have been found under the microscope recognised as low birefringent crystals growing inwards from small vesicle walls. EPMA also indicates the presence of zeolites in the sample (section 4.9.4).

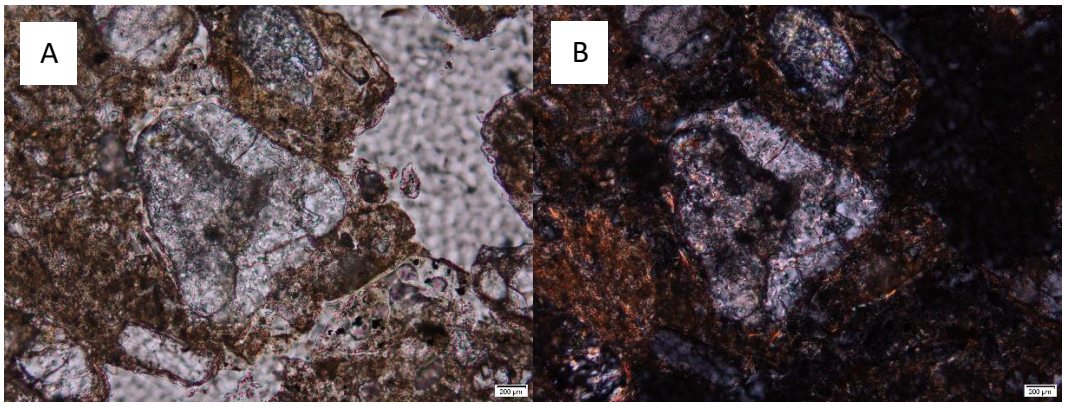

Figure 4.7: A zeolite pictured with different growth fragments within it under (A) plane and (B) cross polarised light.

4.5 Lithics

Within DH2 lithics were also discovered. These range from millimetres to centimetres in diameter. They were generally light brown, weathered and easily crushable. Figure 4.8 shows two different lithic fragments. To the left is a fine-grained clay to siltstone and on the right is a coarser-grained sandstone comprising predominantly of quartz and other weathered grains.

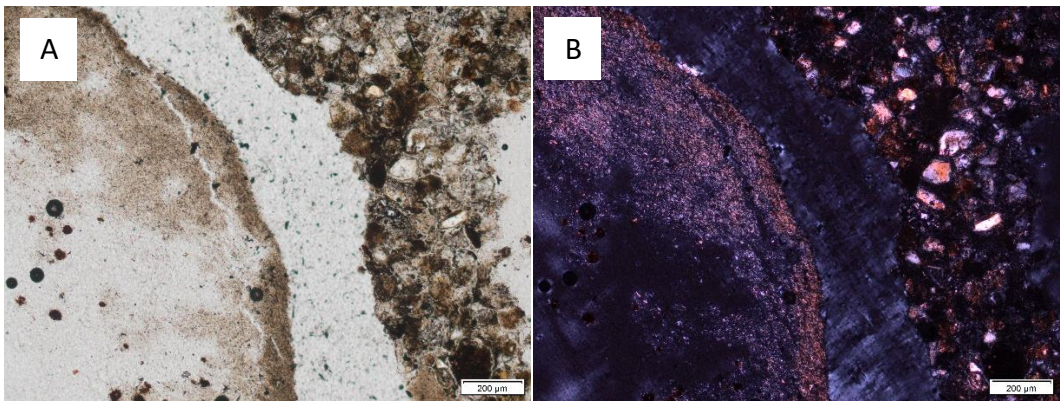

Figure 4.8: Lithics retrieved from DH2 at Karaka under (A) plane polarised and (B) cross polarised light.

4.6 Matrix Composition

The matrix (Figure 4.9) of the tuff deposit extracted from DH2 is a mixed material, generally ranging from white to grey. This becomes more consolidated with depth. When examined under the microscope, further components can be identified. The easiest to see in hand specimen is the small fragments of basalt within the sample

which are a much darker colour than the surrounding material. Other components of the matrix include lithic fragments or rounded lithics grains. The predominant mineral of the matrix is quartz. Quartz grains appear cracked and sub-angular and are generally well sorted in size. There are also some large plagioclase grains which have incorporated within the matrix.

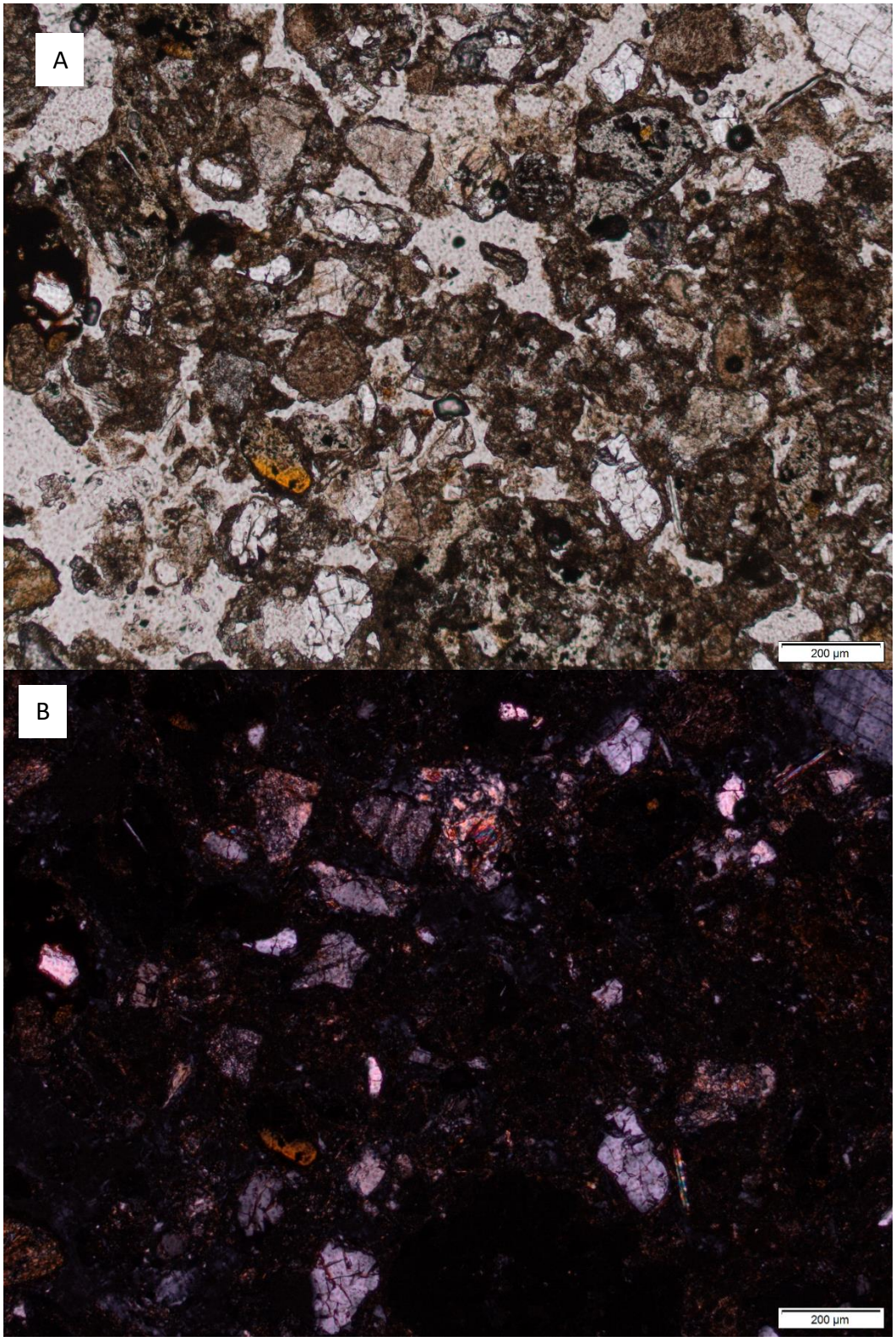

Figure 4.9 An image of the tuff matrix under (A) plane and (B) cross polarised light.

4.7 XRD

XRD was conducted on three basalt samples in an attempt to identify zeolites within the basalt lapilli. The XRD (Figure 4.10) results, however, were dominated by the phenocrysts seen in petrography. The main peaks identified were those of diopside, andesine and fayalite/forsterite. Further analysis is available in Appendix 1.

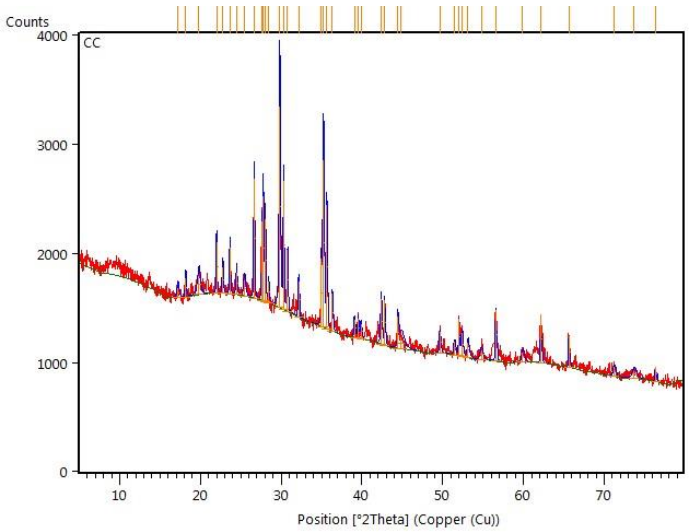

Figure 4.10: Key XRD peaks from sample CC.

4.8 Whole Rock Geochemistry

Whole-rock geochemistry (XRF) of three basalt samples is displayed below in Table 4.2. Silica in all three samples is relatively constant, along with all the other major elements. Many of the trace elements are also similar; however, there are differences between amounts in S, Cl, Co, Ni, Y and Ba. Several elements were not detected in the analysis.

Table 4.2: Major and trace element data for three Karaka basalt samples gained from XRF.

Sample Name	CA	CB	CC
Major elements (XRF, wt.%)			
(normalized to 100% on LOI, volatile free; LOI and Total are original values; all Fe expressed as Fe_2O_3)			
SiO_2	47.50	47.38	47.82
TiO_2	3.33	3.09	3.02
Al_2O_3	13.46	13.79	13.70
Fe_2O_3	16.80	15.94	15.79
MnO	0.17	0.17	0.18
MgO	6.37	6.20	6.14
CaO	7.91	7.98	7.71
Na_2O	2.42	3.05	3.14
K2O	0.92	1.30	1.45
P_2O_5	1.14	1.10	1.06
LOI	3.02	2.56	2.3
Total	99.99	100.57	100.36
Trace elements (XRF, ppm)			
F	553	561	543
S	158	279	288
Cl	248	365	360
Sc	-	-	-
V	205	195	198
Cr	110	101	101
Co	58	64	147
Ni	145	113	104
Cu	45	48	47
Zn	151	140	138
Ga	26	25	25
As	12	11	11
Rb	28	29	32
Sr	861	883	860
Y	40	28	27
Zr	382	357	354
Nb	66	59	56
Mo	-	-	-
Sn	-	-	-
Sb	-	-	-
Cs	20	18	18
Ba	1071	666	639
La	56	49	47
Ce	101	106	109
Nd	48	43	53
Tl	-	-	-
Pb	-	-	-
Th	-	-	-
U	-	-	-

4.8.1 Rock Classification

Results from Karaka obtained using XRF are normalised to 100% volatile free. These have been compared to data from the SAVF (Cook, 2002) and the AVF (McGee *et al.*, 2013) to determine which field it is more closely associated with. If the Karaka chemistry is associated with the SAVF, it is also important to identify if it belongs to Group A or Group B.

Figure 4.11 displays the Karaka whole rock data in green compared to the AVF and SAVF. In this model, the AVF and SAVF data overlap; hence this is not a good proxy for differentiating between the two fields.

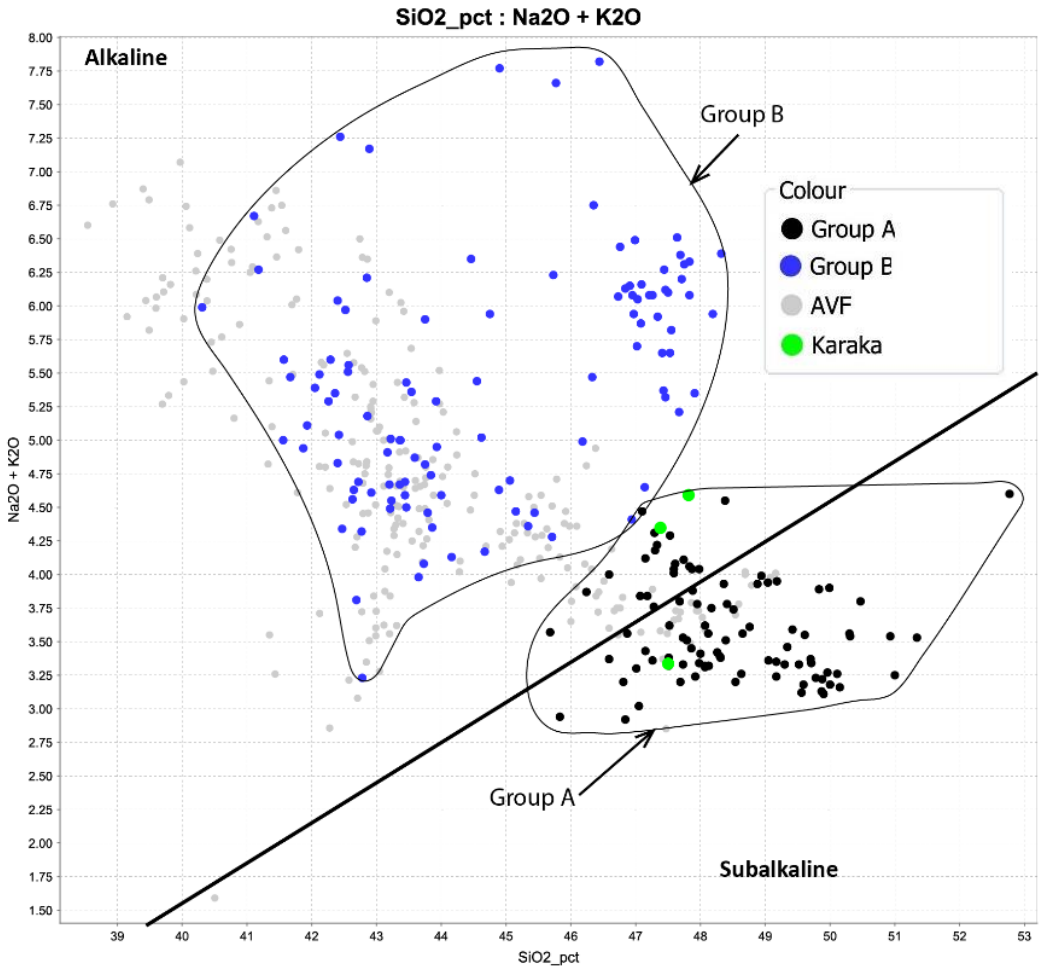

Figure 4.11: ($Na_2O + K_2O$) versus SiO_2 relationships between basalts of Karaka, the SAVF and AVF, as well as the SAVF Group A and B basalts (Miyashiro, 1978).

Two of the Karaka basalt compositions are classified as alkalic, and one is subalkalic but are all within the Group A SAVF basalts. However, a small overlap between Group A and Group B basalts occurs near the Karaka data.

4.8.2 Major element compositions

When examining Karaka basalt against the SAVF and AVF basalts major element data (Figure 4.12), there are some trends. In all graphs comparing Mg_2O% to other major elements, Karaka does not align with the AVF and instead falls within the SAVF as it has a lower Mg_2O wt% than the AVF.

When comparing Mg_2O to K_2O and P_2O_5, Group A and B results separate showing distinct patterns. With P_2O_5, Karaka basalt occurs within the Group B field, however, with K_2O only, one Karaka sample lies within the Group A field whilst two do not fit into either field.

Groups A and B occur in separate fields when considering Mg_2O versus Na_2O, TiO_2 and SiO_2 with some minor overlap. Karaka basalts do not show clear associations in these graphs, falling within, out of, or in areas of overlap between the two groups.

The two groups do not separate well when comparing Mg_2O to Fe_2O_3, CaO and Al_2O_3 with less of a pattern evident between the two groups and within the Karaka data.

4.8.3 Trace Elements

There is a visible trend when Group A and B basalts have their trace elements plotted against Mg_2O (Figure 4.13). Group A basalts are in most cases depleted in these elements, plotting lower and distinct from the Group B basalts. Several elements show more overlap, particularly Ba and Y.

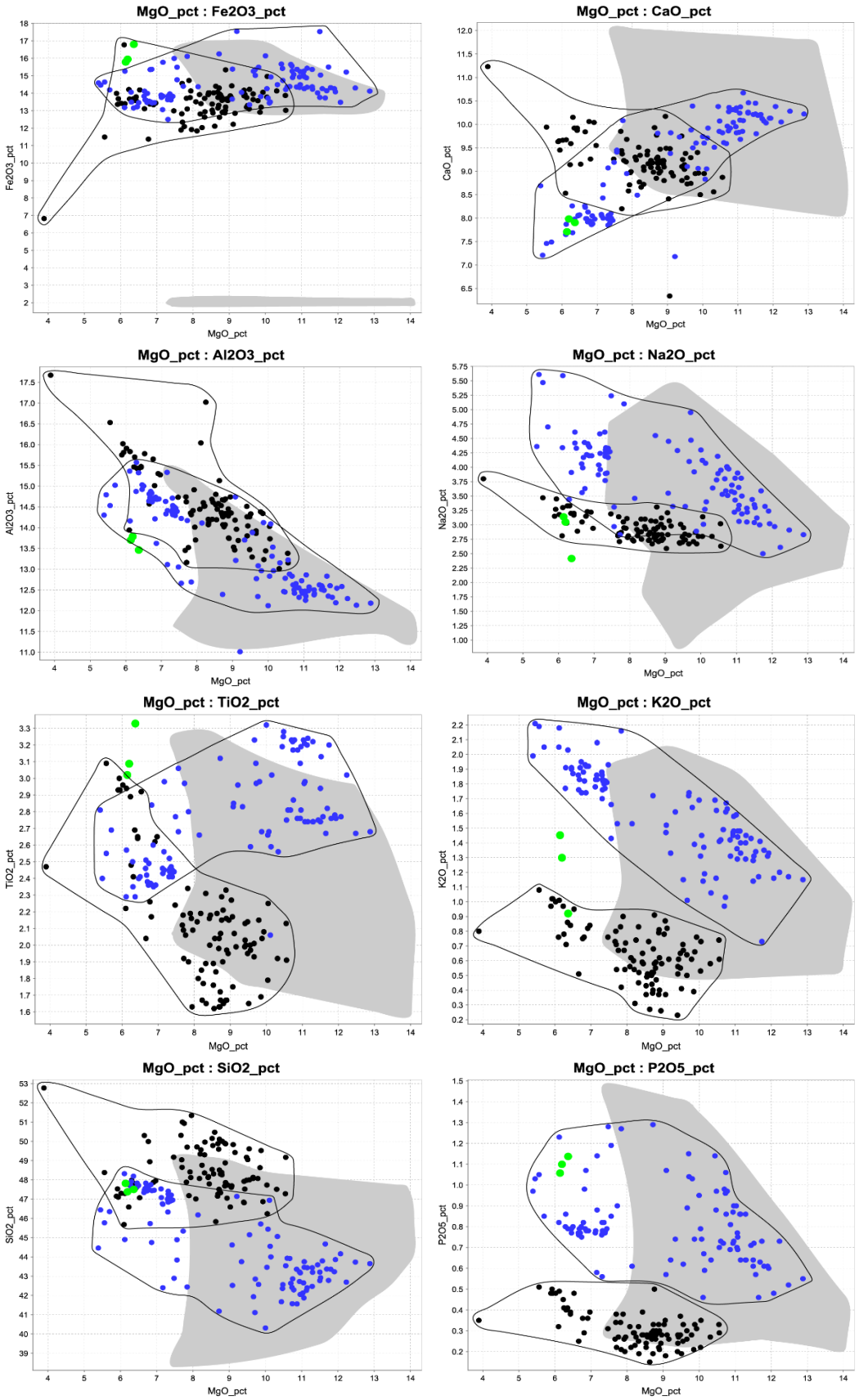

Figure 4.12: Variation diagrams of major elements versus MgO for whole-rock analyses displaying general trends in the SAVF and Karaka data sets. Karaka basalts in green, Group A in black, Group B in blue and AVF in grey.

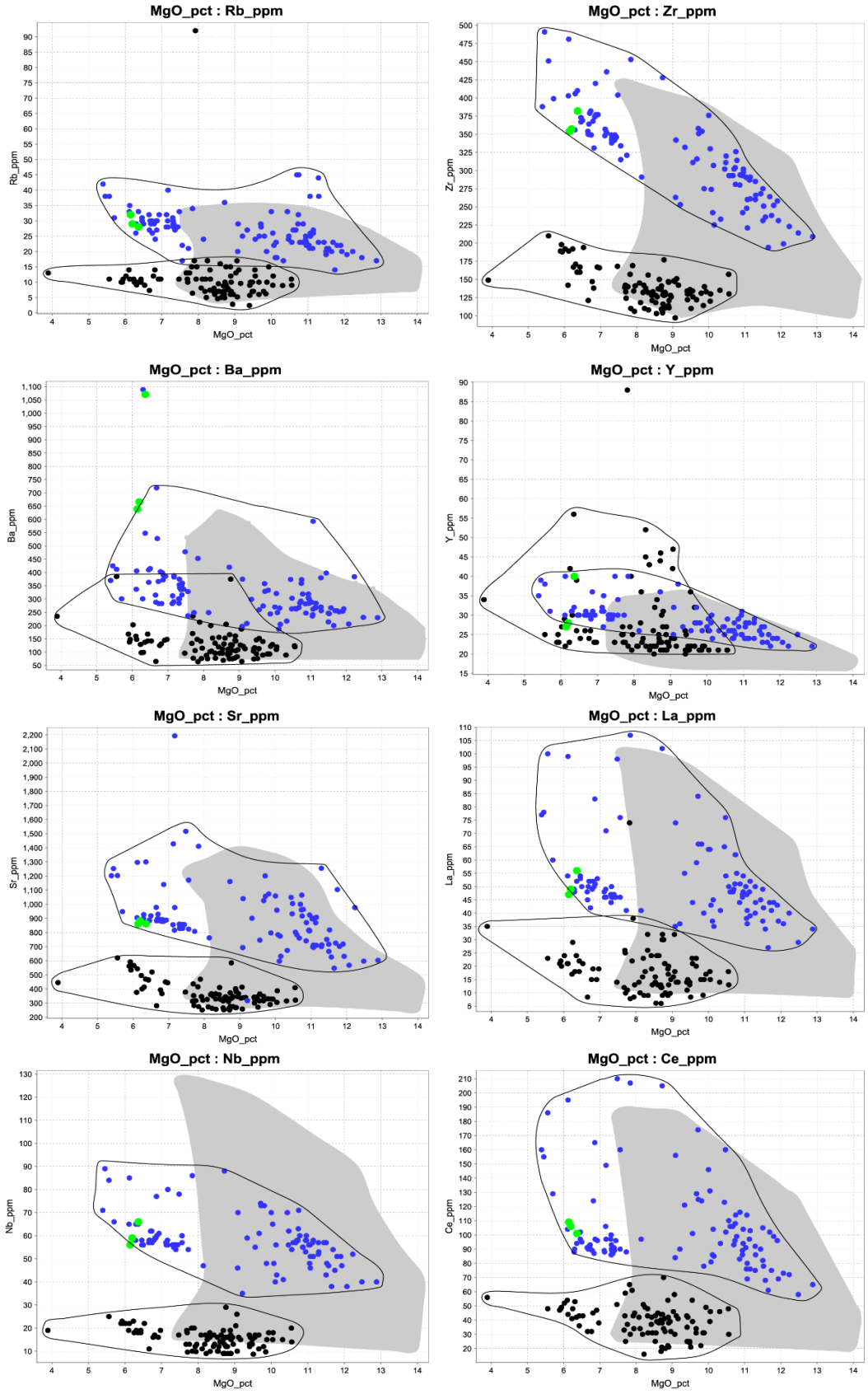

Figure 4.13: Variation diagrams of trace elements versus MgO for whole-rock analyses displaying general trends in the SAVF and Karaka data sets. Karaka basalts in green, Group A in black, Group B in blue and AVF in grey.

When the Karaka data is compared using these elements, they generally fall within the Group B basalts. Cases, where this differs, is in Y and Ba where they overlap with Group A results or display a much higher Ba than other Group B basalts.

Trace elements when plotted against P_2O_5 (Figure 4.14) also show the SAVF and AVF values overlapping which makes it hard to distinguish between the two when looking at the Karaka results.

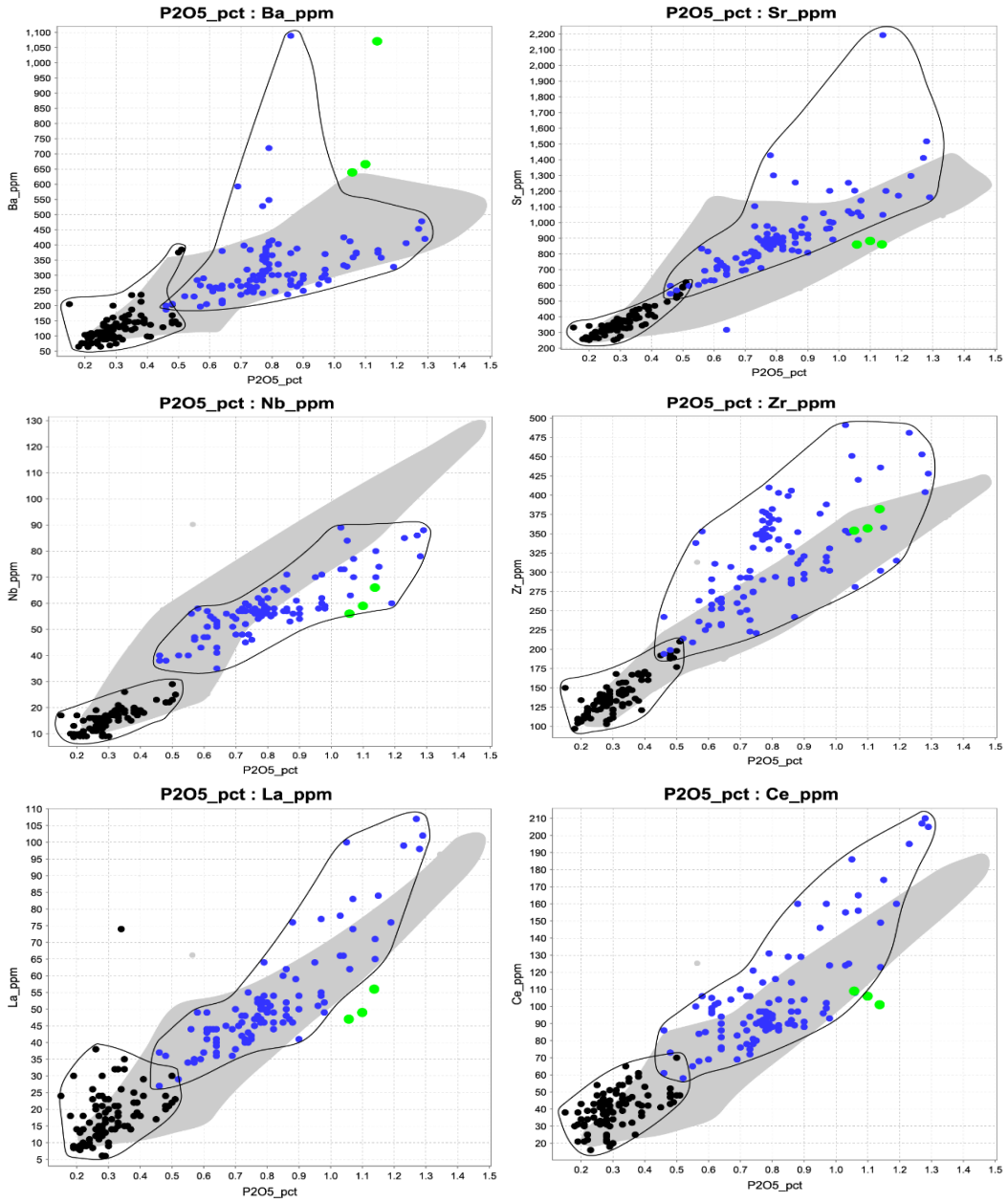

Figure 4.14: Variation diagrams of trace elements versus P_2O_5 for whole-rock analyses displaying general trends in the SAVF and Karaka data sets. Karaka basalts in green, Group A in black, Group B in blue and AVF in grey. The AVF shows some overlap with both Group A and B basalts in these analyses; however, it does not display any overlap with the Karaka basalts.

A distinct trend is seen between Group A and Group B, however. Karaka points fall outside the SAVF and AVF results in Ba, La and Ce graphs. With the Nb and Zr trends, the Karaka points follow the Group B results.

4.9 Mineral Chemistry

EPMA data for different elements were taken and normalised to 100% for the appropriate elemental and mineral analysis. Further data is available in Appendix 2.

4.9.1 Pyroxene

Pyroxene was probed and normalised using calcium, magnesium and iron. These were plotted on a representative ternary plot to classify the type of pyroxene minerals present. All the pyroxenes probed from Karaka are classified as diopside seen in Figure 4.15.

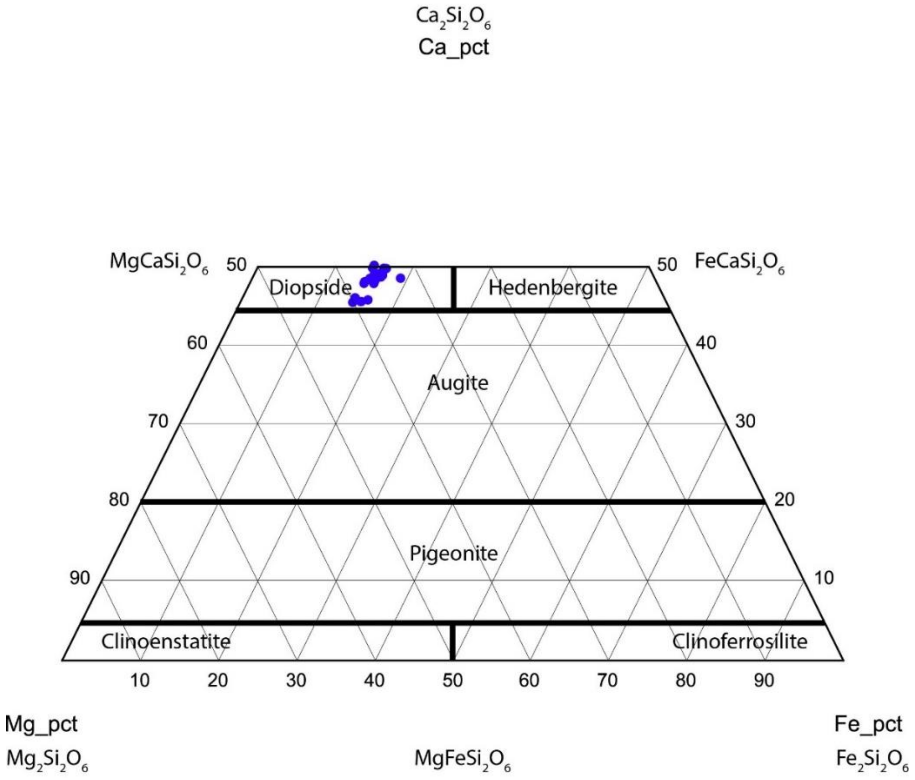

Figure 4.15: Ternary diagram showing the mineral composition of pyroxene probed from Karaka.

4.9.2 Olivine

Olivine was probed and normalised using iron and magnesium. Olivine end members range from the Mg-rich forsterite to Fe-rich fayalite. These results show that the olivine from Karaka ranges from Fo_{62} to Fo_{75} seen in Figure 4.16.

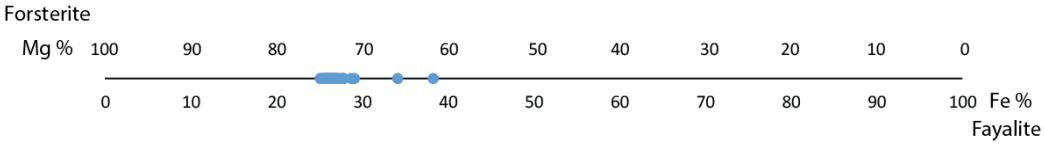

Figure 4.16: Olivine range in composition from fayalite to forsterite.

4.9.3 Plagioclase

Plagioclase was probed, and results were normalised using potassium, calcium and sodium. These values plotted on a ternary diagram (Figure 4.17) show that plagioclase from Karaka samples ranges from labradorite to andesine (Ar_{45-62}).

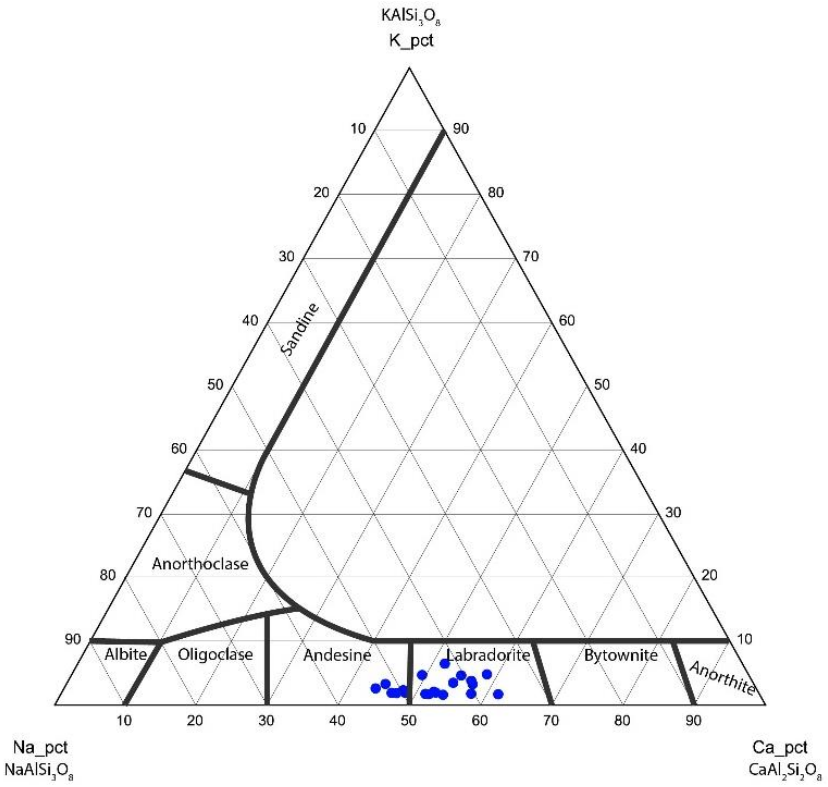

Figure 4.17: Plagioclase ternary diagram displaying the composition of plagioclase in Karaka basalts.

4.9.4 Zeolites

Several points were initially probed as plagioclase but returned anomalous compositions (Table 4.3). The relative proportion of SiO_2, Al_2O_3, alkalis and lack of other major elements, are consistent with zeolites compositions.

Table 4.3: Zeolite probe compositions.

SiO2	TiO2	Al2O3	FeO	MgO	CaO	Na2O	K2O	Total
68.23	0.00	22.07	0.09	0.07	0.39	8.20	0.95	98.08
68.40	0.00	22.00	1.14	0.19	0.34	7.67	0.26	98.90
68.87	0.00	21.57	0.06	0.00	0.29	9.09	0.12	99.90

Chapter 5

Sedimentary Deposits and Tephras

5.1 Introduction

Organic sedimentary deposits and tephra were identified in DH1 as described in Chapter 3. The base of the sedimentary and tephra succession was not reached in DH1, but a good succession of tephras and organic silts and muds are visible. Tephras range in thickness from 1 mm to over a meter and range in composition and colour. Tephras found within North Island lakes are sourced from both the TVZ and CVZ, and are often siliceous. Organic muds and silts within this deposit form brown, 2 mm thick laminated beds.

5.2 Methods

5.2.1 Petrography

Following the optical microscopy methods described in Section 4.2.2 thin sections of sands from the roadside outcrop were examined.

5.2.2 Scanning Electron Microscope

Samples of sand from the roadside outcrop, transitional sediments, organic sedimentary deposits and tephras from DH1 were examined using a SEM. These samples were dried and mounted on stubs using tar tape. Stubs were labelled, and two samples were mounted on each, using a long or short piece of tape. Care was taken to stop contamination between tape pieces. Samples were then coated in platinum for use in the HITACHI S-4700 field emission SEM. Samples were examined using an acceleration voltage of 5 kV.

5.2.3 Grain size

Grain size measurements of DH1 and roadside sands were acquired using a Malvern Mastersizer 3000. This uses laser diffraction to measure particle sizes through light scattering pattern. Samples were added through the dispersion tank, which constantly mixes and sonicates the sample to disaggregate them. The sample was added until the laser was at optimal obscuration, and then the sample was read.

5.2.4 Organic Content - Loss on Ignition

Sedimentary samples were tested for organic content using LOI. This is done by recording weights at several stages of the experiment. Empty dishes were weighed and filled with a sample, and they were then reweighed. These samples were placed in the oven and cooked to burn off any organic material. Once they were taken from the oven, they were reweighed and the difference recorded and converted into a percentage of the original sample.

5.2.5 Electron Probe Microanalysis (EPMA)

Following the optical microscopy methods described in Section 4.2.5 EPMA analysis of tephra samples were analysed by Jenni Hopkins at the Victoria University of Wellington. Glass shards were probed, and major element data for the samples was recorded. All of this data has been normalised to 100% volatile free.

5.3 Sand succession on Road cutting, Urquhart Rd (SC1)

The three different sands sampled from SC1 (Figure 3.10 and 3.11) were examined under SEM and using a petrographic microscope. Their stratigraphic position and field descriptions were presented in Section 3. Grain size (Figure 5.1) for these sands was relatively consistent and unsorted.

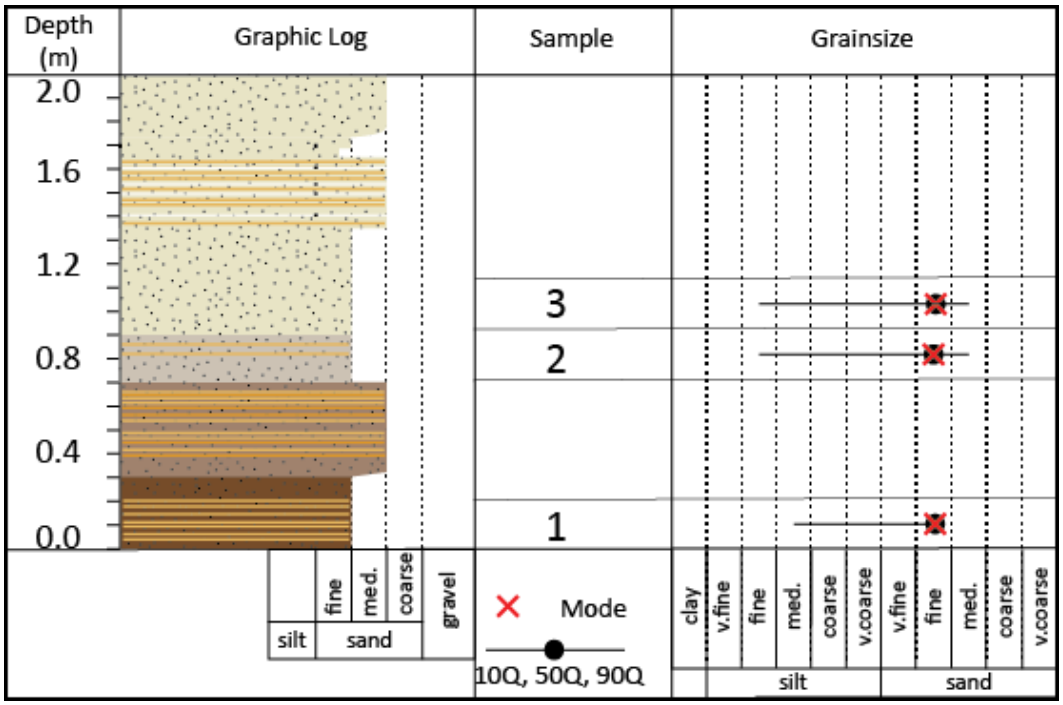

Figure 5.1: Stratigraphic column displaying grain size of sands sampled at SC1 gained from laser sizing.

5.3.1 Sand 1 – Brown FINE SAND

Sand 1 (S1) (Figure 5.2) is a poorly sorted brown fine sand formed predominantly of sub-rounded weathered brown lithics. Of the remaining grains, 30% are sub-angular plagioclase, <10% are sub-angular opaque minerals, and <1% is biotite. Grain sizes in this sample range from medium silt to medium sand.

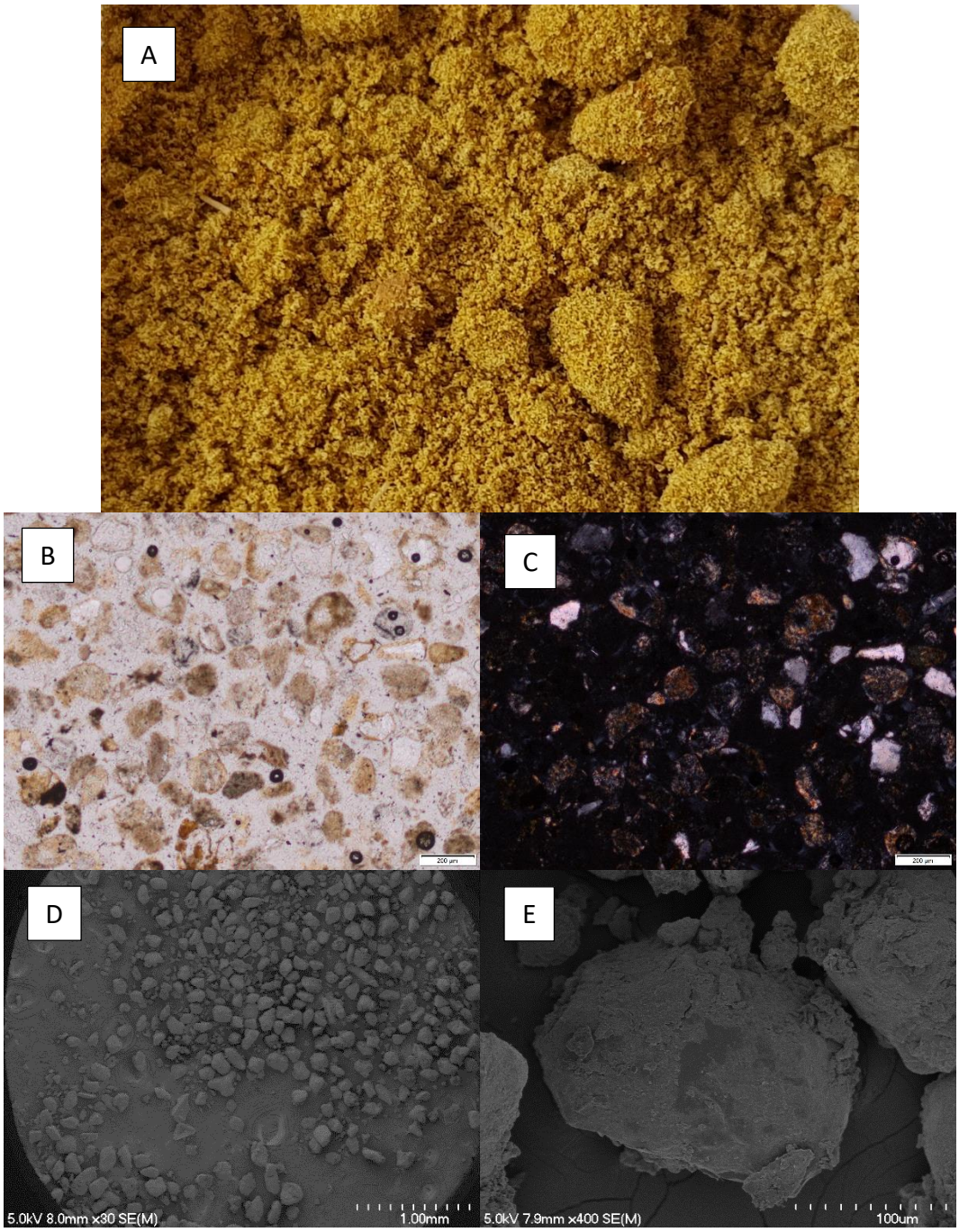

Figure 5.2: (A) Sand 1 in hand sample, (B) under the petrographic microscope in plane polarised light, and (C) cross polarised light, (D) under the SEM showing the overall grain size, and (E) showing a grain at a closer magnification.

5.3.2 Sand 2 – Greyish Brown FINE SAND

Sand 2 (Figure 5.3) is a greyish brown medium sand. It is composed of 45% sub-angular quartz grains, 30% rounded lithics, 10% sub-angular plagioclase and 5% rounded opaque minerals. Biotite grains make up <1% of the sample. Grain sizes in this sample range from fine silt to medium sand.

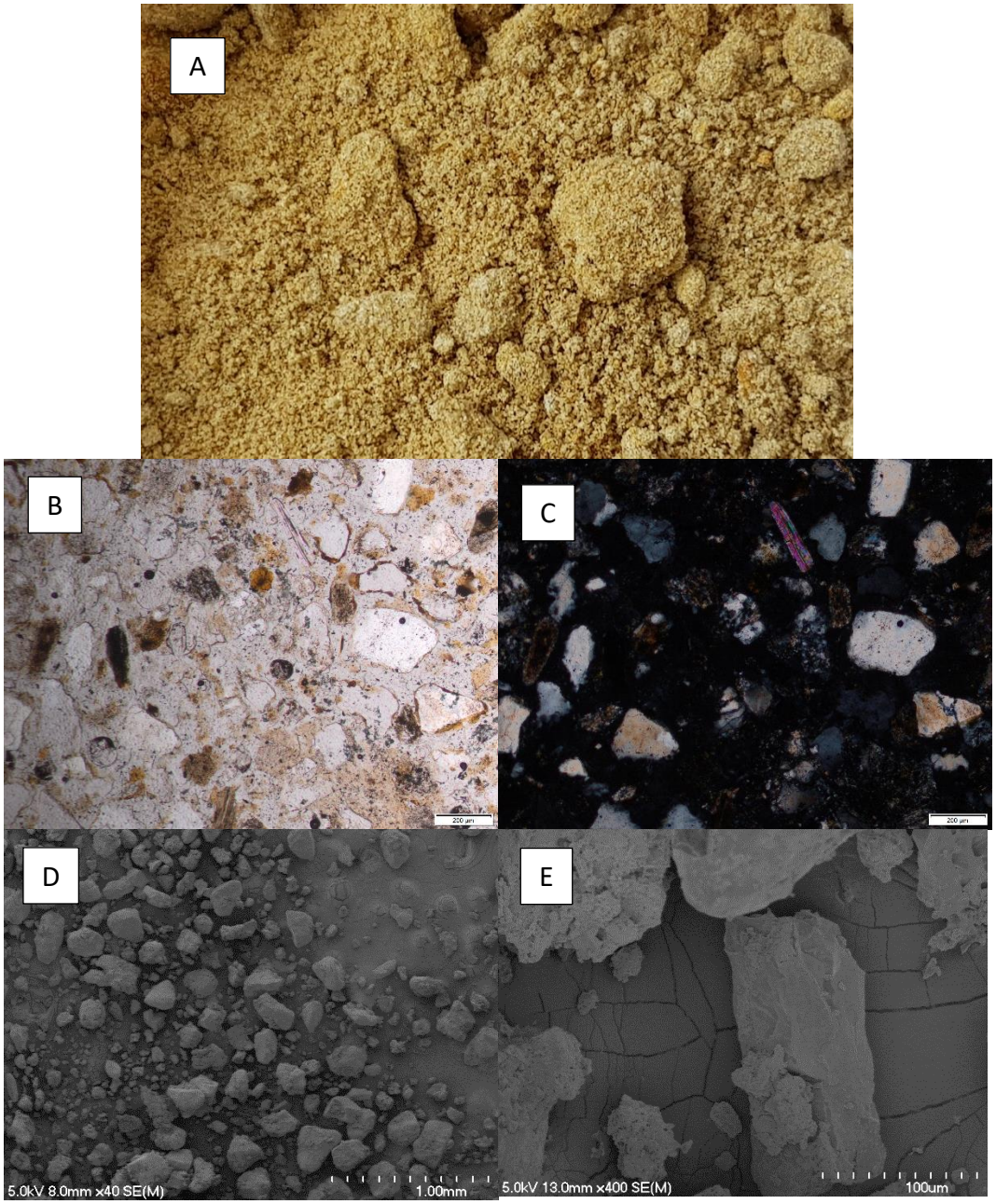

Figure 5.3: (A) Sand 2 in hand sample, (B) under the petrographic microscope in plane polarised light, and (C) cross polarised light, (D) under the SEM showing the overall grain size, and (E) showing a grain at a closer magnification.

5.3.3 Sand 3 – White FINE SAND

Sand 3 (S3) (Figure 5.4) is white fine sand. S3 is comprised of 70% sub-angular quartz crystals, 15% sub-rounded plagioclase crystals, 14% rounded lithics and, 1% of other minerals. Grain size ranges from fine silt to medium sand.

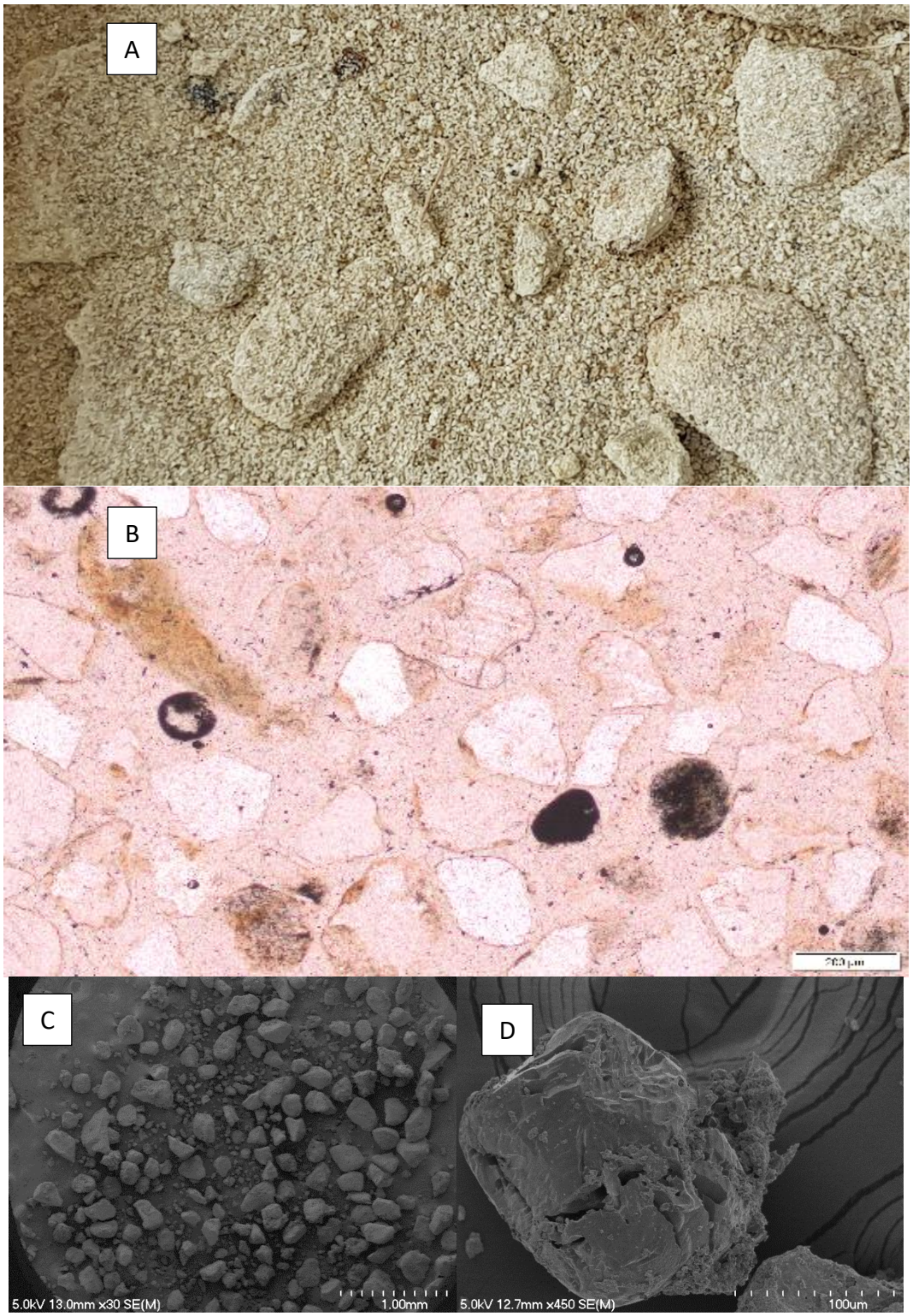

Figure 5.4: (A) Sand 3 in hand sample, (B) under the petrographic microscope in plane polarised light, (C) under the SEM showing the overall grain size, and (D) showing a grain at a closer magnification.

5.4 Grain Size variation of DH1 core.

Samples were taken from the cover ash beds (A – R) and range in grain size throughout the profile. The average grain size is fine silt (Figure 5.5). Many of these samples have a minimum grain size of clay and maximum size of coarse sand. Some samples have a mode of coarse sand and are poorly sorted, including E, H and K.

Grain sizes of the transitional sediments were less consistent than the cover beds (Figure 5.5). Transitional sediment samples (S – AC) generally have a comparable mode and median but are poorly sorted. Grain sizes of many of these samples range from clay to very coarse sand.

Organic sedimentary deposit samples (AD, AF, AH, AI, AJ, AV) are well-sorted and had equal modes and medians. In general, they had a median grain size below coarse silt (Figure 5.5).

Tephras (AE, AG, AK – AP, AQ – AT) were varied in grain size and were well to poorly sorted. The maximum grain size of these samples was coarse sand, and the minimum size was clay (Figure 5.5).

Appendix 3 holds the grainsize data used.

5.5 Grain Composition of Beds within DH1 Core

5.5.1 Cover Succession – Hamilton Ash

The cover bed succession (Hamilton Ash) is comprised of weathered clay and silt. It has been described in Section 3.3, not by microscopic methods, as its composition was beyond the scope of this study.

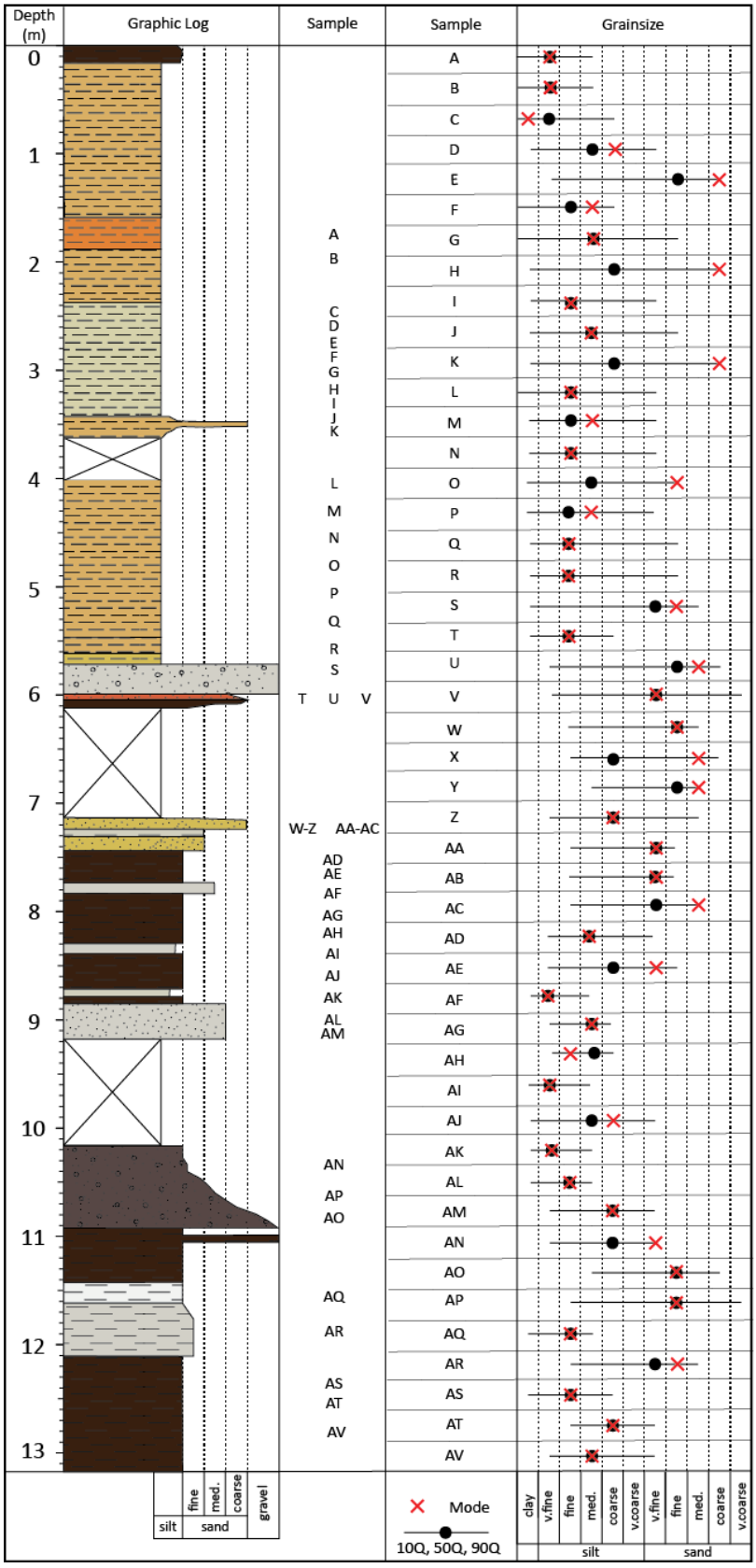

Figure 5.5 The grain size determined for samples from DH1 using a laser particle sizer compared to their stratigraphic position in DH1.

5.5.2 Transitional Sediments

Samples from DH1 that are taken from the transitional sediments are labelled from S through to AC (5.7 to 7.4 m in the core (Figure 5.5)). These sediments do not fall into either the clay cover beds or the organic sedimentary and tephra succession in the lower part of DH1. The transitional sediments include wood, sand and silt. Under the SEM several beds appear to be glassy. This package begins with an obvious tephra layer, which has begun to weather into the clay from a pumice rich material.

5.5.2.1 U

Sample U is reddish-brown fine sand that is a very thin hard layer near the top of the transitional sediments. Figure 5.6 displays U under the SEM. This sample is poorly sorted, consisting of glass shards and small pumice grains. Glass shards range in shape from lunate to cuspate. Pumice fragments are vesicular with circular bubble walls.

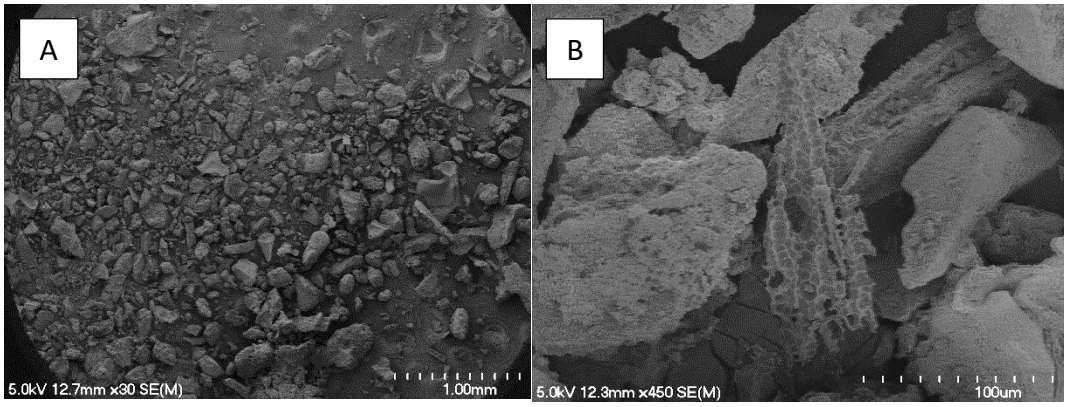

Figure 5.6 Sample U under the SEM, (A) overall-grain morphologies of this sample and, (B) a close up of individual grains in the sample.

5.5.2.2 AA

Sample AA (Figure 5.7) is a moderately sorted light grey, fine sand that is 20 mm thick in DH1. Viewed under SEM AA comprises of predominantly glass shards and some larger pumice fragments. Glass shards are cuspate in shape, indicating bubble wall joins, whilst pumice appears to have lenticular or elongate vesicles that form flat pumice shards.

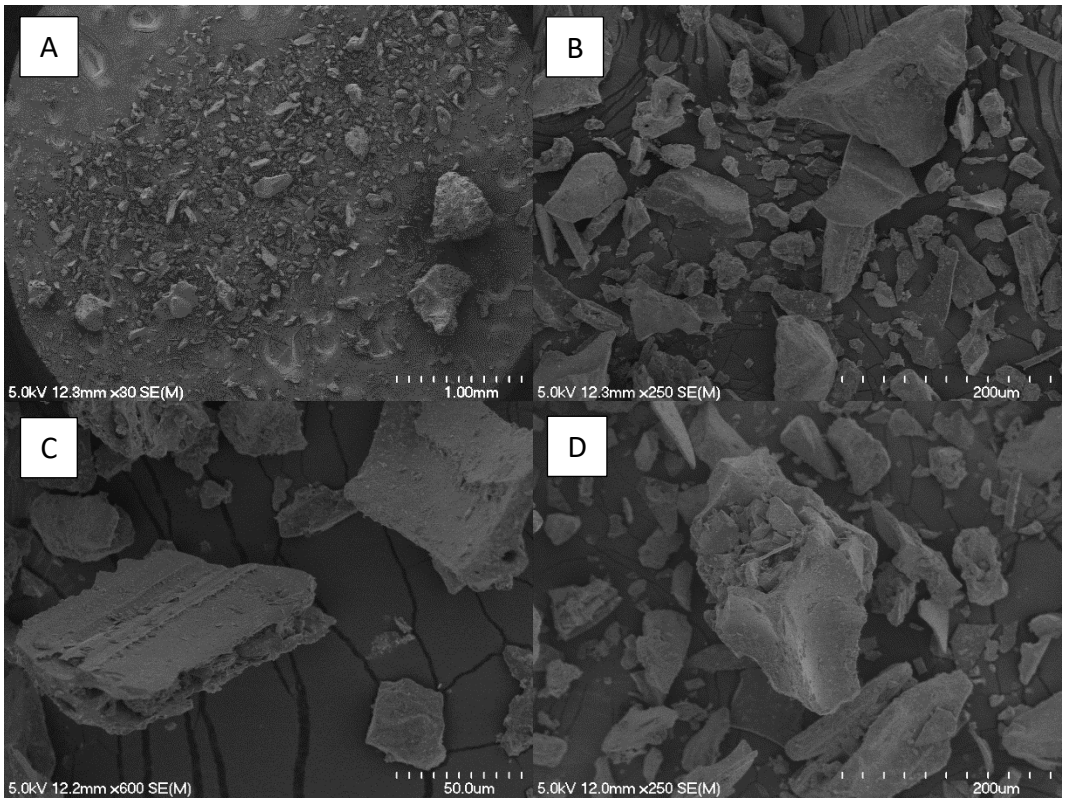

Figure 5.7 Sample AA under the SEM, (A) overall-grain morphologies of this sample and, (B) glass shards, (C) and (D) pumice fragments.

5.5.2.3 AB

Sample AB as seen in Figure 5.8, is yellow-brown fine sand that in DH1 is very hard and contains black bands that become dark brown with depth. This sample is predominantly composed of assorted cuspate glass fragments. There is also a large component of pumice with fibrous cellular structure. This structure forms small circular vesicles enclosed in lenticular bubble walls (Fisher & Schmincke, 1984).

5.5.3 Sedimentary Organic Deposits

Laminated brown sediments discovered in DH1 were sampled at several depths, and representative particles they contain are pictured under the SEM (Figure 5.9). Of the samples investigated (AD, AH and OR1 through to OR5) all were identified as diatomaceous mud/silt, with no other grain types seen under the SEM. The diatoms were round and wheel-like. Some diatoms are joined together with jagged protrusions, and others formed long strands or filaments. No plant material was identified.

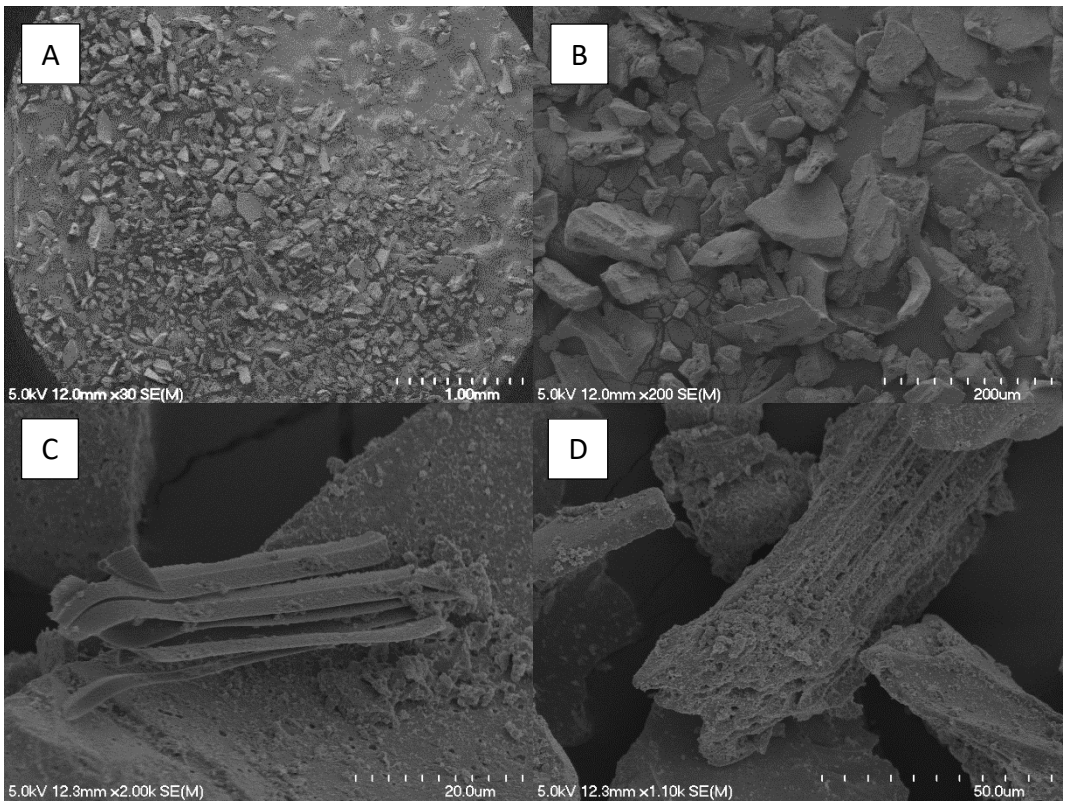

Figure 5.8 Sample AB under the SEM, (A) overall-grain morphologies of this sample and, (B) glass shards, (C) filaments within the sample and (D) fibrous pumice fragments.

Table 5.1 displays the results of LOI analyses of six different lake sediment samples. The organic content of these samples ranges from 9.63% in sample OR6 to 13.68% at the surface of the lake sediments in sample OR1.

Table 5.1: Loss on ignition of lake sediments at different depths.

Sample # Depth	**Tin weight** (g)	**Weight 1** (g)	**Weight 2** (g)	**Organic Content** (%)
OR1 (7.6 m)	0.9171	3.6122	3.1179	13.68
OR2 (8 m)	0.9161	2.5503	2.2752	10.79
OR3 (8.5 m)	0.916	3.0826	2.6016	15.60
OR4 (11.3 m)	0.9171	4.3884	3.8313	12.69
OR5 (12.2 m)	0.9182	3.8557	3.4059	11.66
OR6 (13 m)	0.9117	3.502	3.1649	9.63

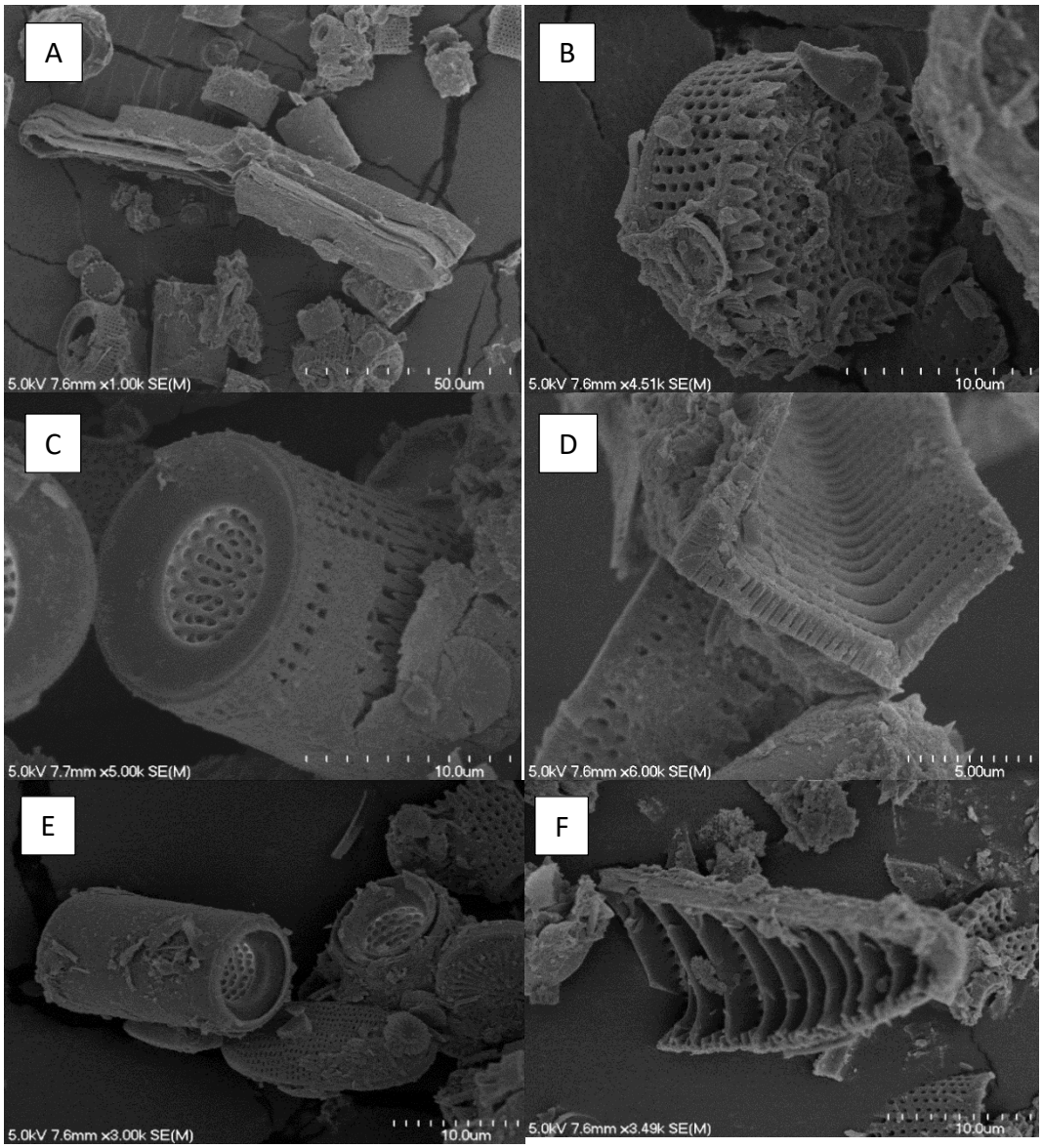

Figure 5.9: Diatoms imaged from samples AD and AH using SEM. (A) Several different diatom morphologies including pinwheel and filamentous species and, (B) a diatom with smaller diatoms emplaced on its surface. Further diatom variations are seen in (C) with two diatoms connected with spikey protrusions, (D) a diatom that has formed square filaments, (E) a cylindrical diatom and, (F) a cross-section of a diatom in the sample.

5.5.3.1 Basal Sample (OR6)

OR6 (Figure 5.10) is the lowermost sample extracted from DH1. It shares characteristics of both tephra and a lake sediments. At 12 m deep, the core was beginning to become more consolidated and changed from brown to grey. This sample was difficult to extract during drilling. Under SEM, the sample was comprised of diatoms, glass, fibrous material and crystals.

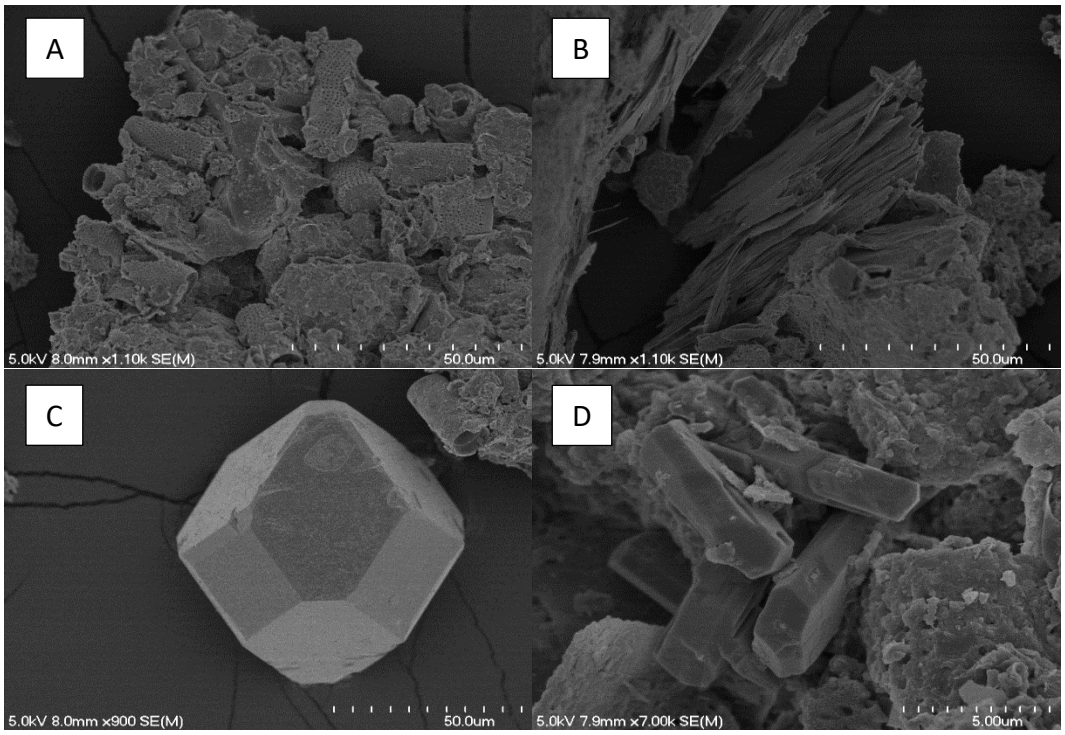

Figure 5.10 Different grains present within sample OR6 as seen under the SEM. (A) Diatoms are present within a coating of another material, (B) fibrous woody material, (C) a crystal with a tetragonal growth pattern and, (D) triclinic crystals.

5.5.4 Tephras

Tephras were found interbedded with the organic sedimentary succession of DH1 from 7.4-13.2 m deep. Often the tephra was grey and a few millimetres thick. These have also been examined under the SEM to determine their grain composition.

5.5.4.1 AE

Sample AE is from a 10 cm thick grey bed. Figure 5.11 displays four images taken of volcanic glass from AE. This sample is poorly sorted, and ranges in grain size from very fine silt to fine sand, with an average size of coarse silt. Glass shards within this sample, are cuspate in shape. Pumice within the sample is less vesicular than other samples investigated. Vesicles appear cylindrical with thick bubble walls.

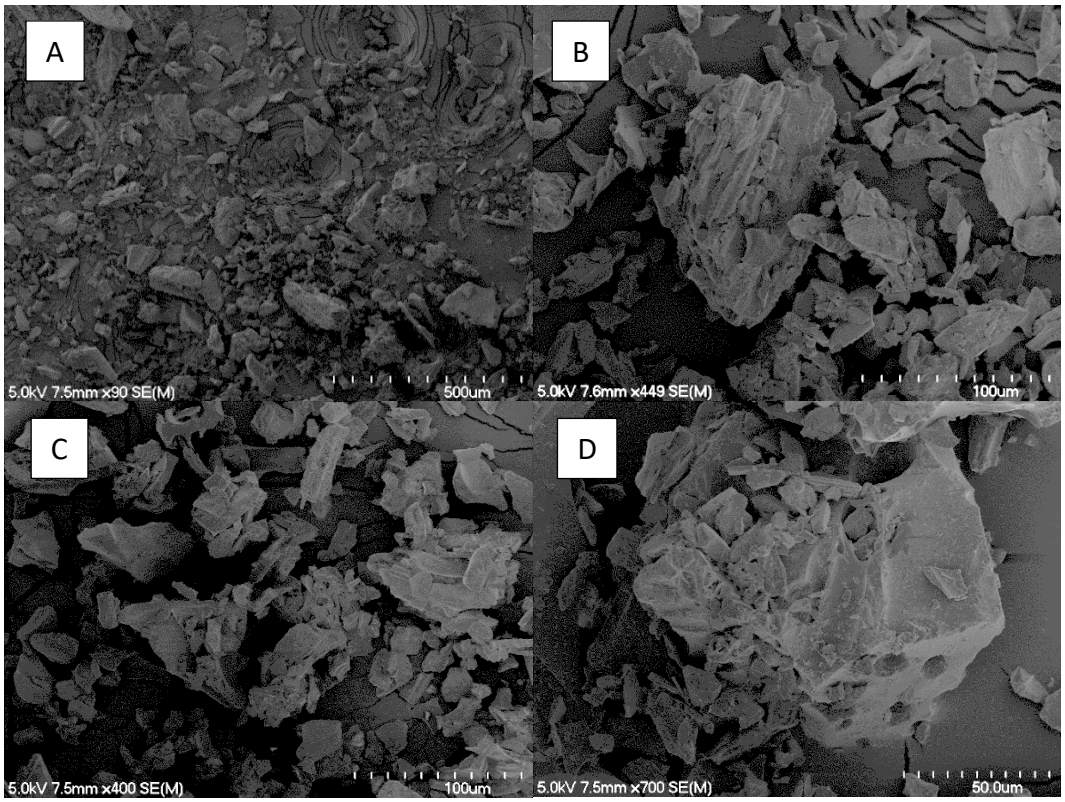

Figure 5.11: SEM images of sample AE. (A) Overall grain composition of this sample, (B and C) pumice fragments and, (D) a pumice fragment with circular vesicles and thick bubble walls.

5.5.4.2 AM

Sample AM is a moderately sorted dark grey coarse silt with grain sizes ranging from very fine silt to very fine sand. Grains are predominantly pumice fragments rather than bubble wall shards, although some glass shards are present. Figure 5.12 displays the grains visualised under SEM.

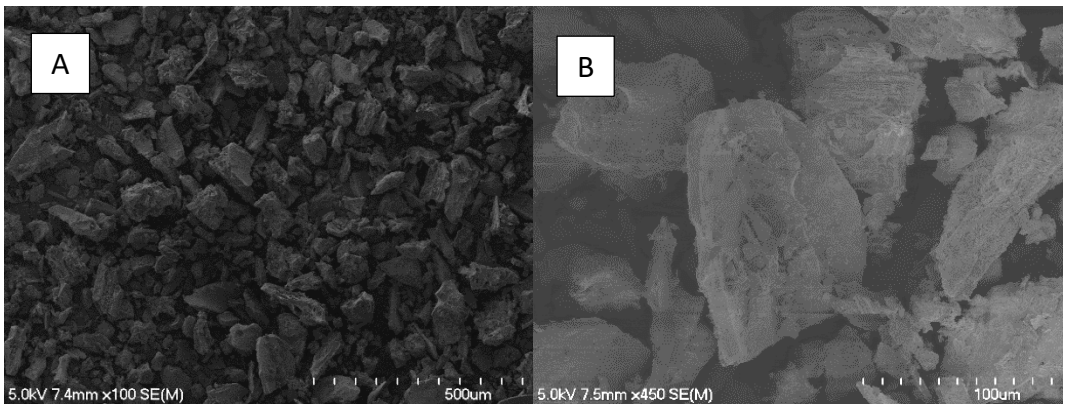

Figure 5.12 Sample AM under the SEM, displaying a moderately sorted pumice. (A) Overall grain morphologies of this sample, (B) a close up of pumice fragments.

5.5.4.3 AN

Sample AN (Figure 5.13) is a moderately sorted coarse silt from the middle of a grey graded deposit with black flecks. Grain sizes of this sample range from very fine silt to very fine sand. Despite being a similar grain size to sample AM, this sample is composed of predominantly glass shards. Both lunate and cuspate glass shards are present, as well as some minor pumice with spherical vesicles.

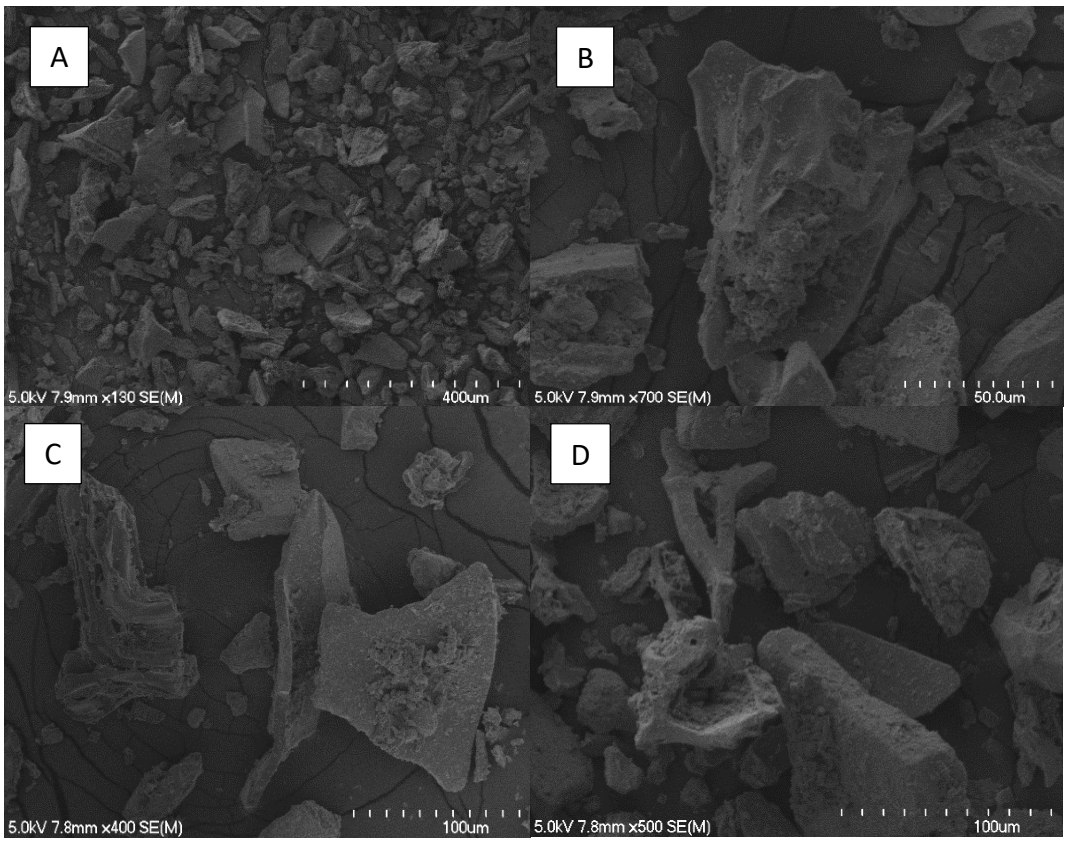

Figure 5.13 Sample AN under the SEM displaying different grain types. (A) Overall grain morphologies of this sample, (B and C) pumice shard glass fragments, and, (D) a round vesicle of a broken glass shard.

5.5.4.4 AP

This sample (Figure 5.14) is a poorly sorted fine sand near the base of a graded deposit with black flecks. Grain sizes in this sample range in size from fine silt to very coarse sand. Pumice shards with both elongate and circular vesicles are present as well as cuspate glass shards. Other grain types include possible micro-fossils in the form of long rods.

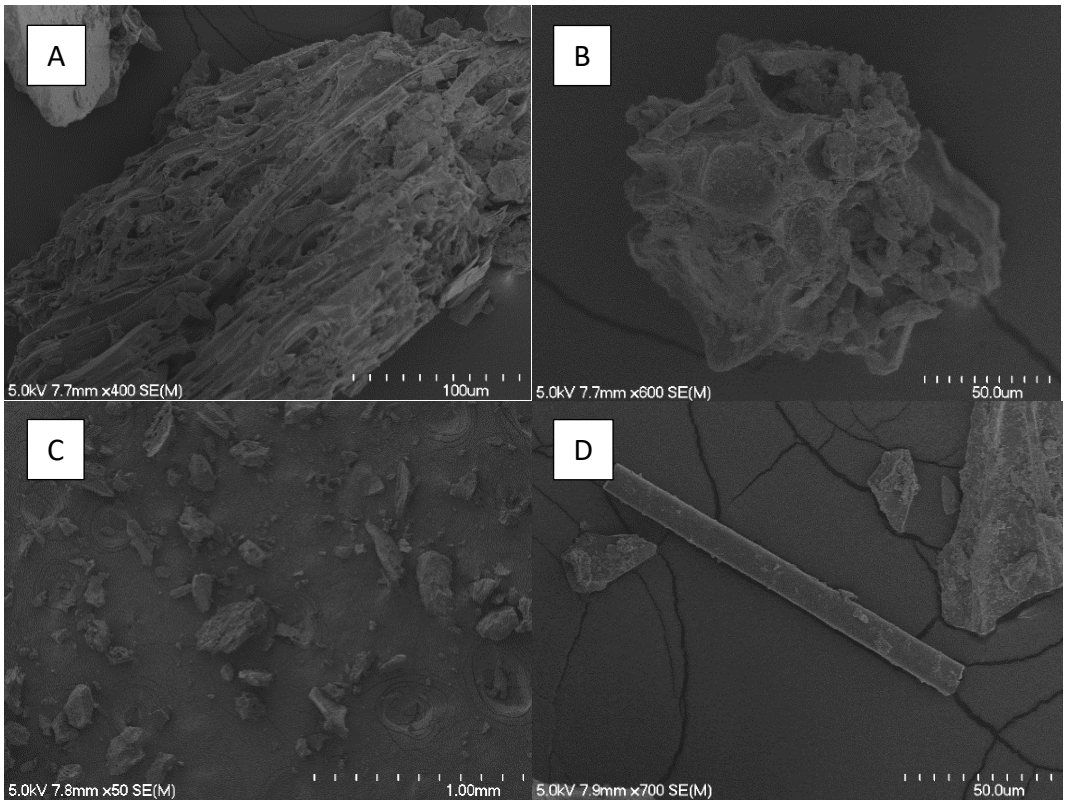

Figure 5.14 Grain types of sample AP as seen under the SEM. (A) A fibrous pumice fragment with lenticular vesicles, (B) a pumice fragment with circular vesicles, (C) overall grain morphologies in this samples, and (D) a possible microfossil.

5.5.4.5 AQ

This sample (Figure 5.15) is a well-sorted very brittle light grey, fine silt with grains ranging in size from clay to medium silt. Most grains within this sample are cuspate glass shards. Some pumice shards are also included and have a fibrous bubble structure. Unlike other samples, AQ has thin twisted glass fragments.

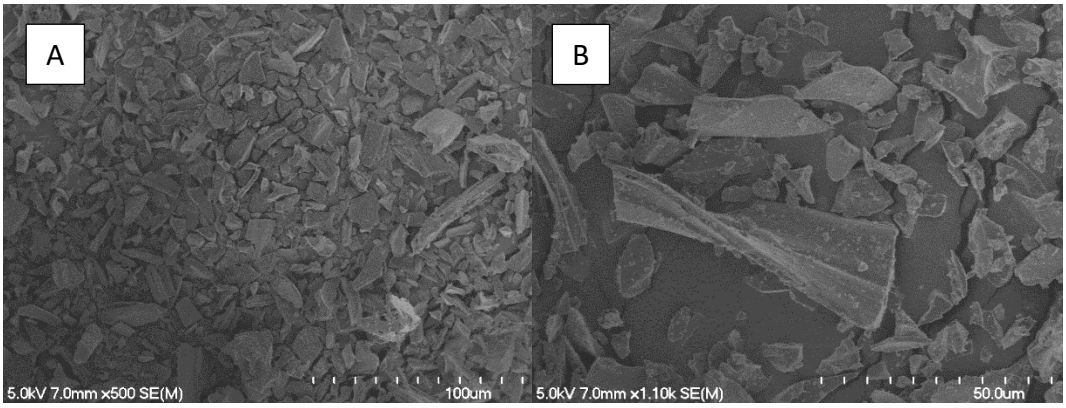

Figure 5.15 Sample AQ as seen under the SEM. (A) Overall grain morphologies in this samples, (B) stretched and twisted glass fragments.

5.6 Tephra analysis (EMPA)

Several tephra layers were sampled from the organic sediment succession (Figure 5.16). Glass from tephras TA, TB, TL, TO, TS, TR, TT, TU, TV and TW were analysed for major element abundances by EPMA. Two samples (TT and TR) have been removed from analysis due to very high H_2O values, likely due to weathering. The remaining tephras have been compared and examined below (Figure 5.17). Samples TV and TW have been sampled from two depths within the same tephra deposit. Data for these tephras is available in Appendix 4.

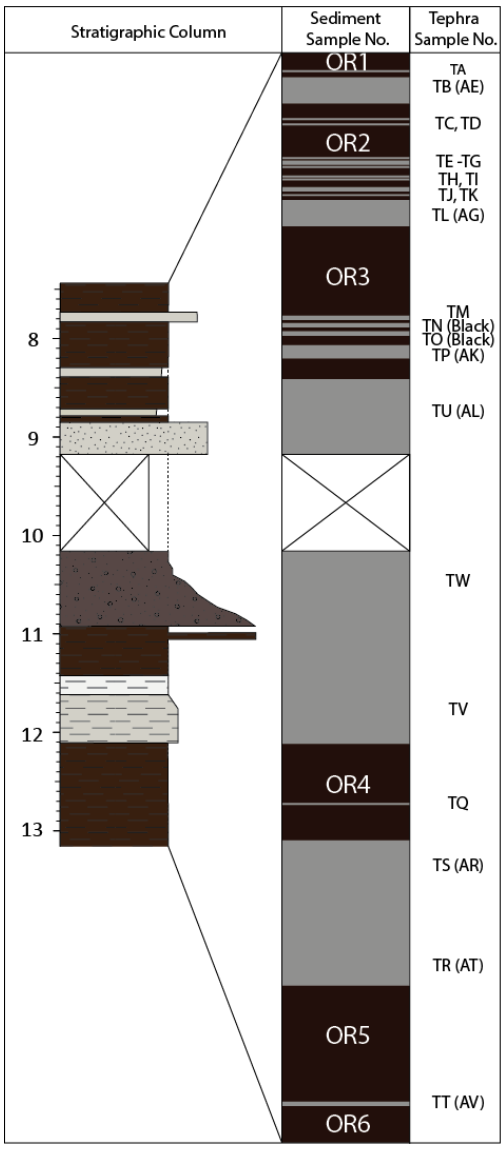

Figure 5.16: Tephra succession in the organic sedimentary succession of DH1.

TA shown in green (Figure 5.17), has a SiO_2 range of 75-77.5%, CaO 0.8-1.35% and Al_2O_3 values from 12.73-13.62%. These plot as a wide spread amongst the other tephras analysed, but form two separate groups when comparing CaO and Al_2O_3. These groupings are of low CaO and Al_2O_3 and high CaO and Al_2O_3.

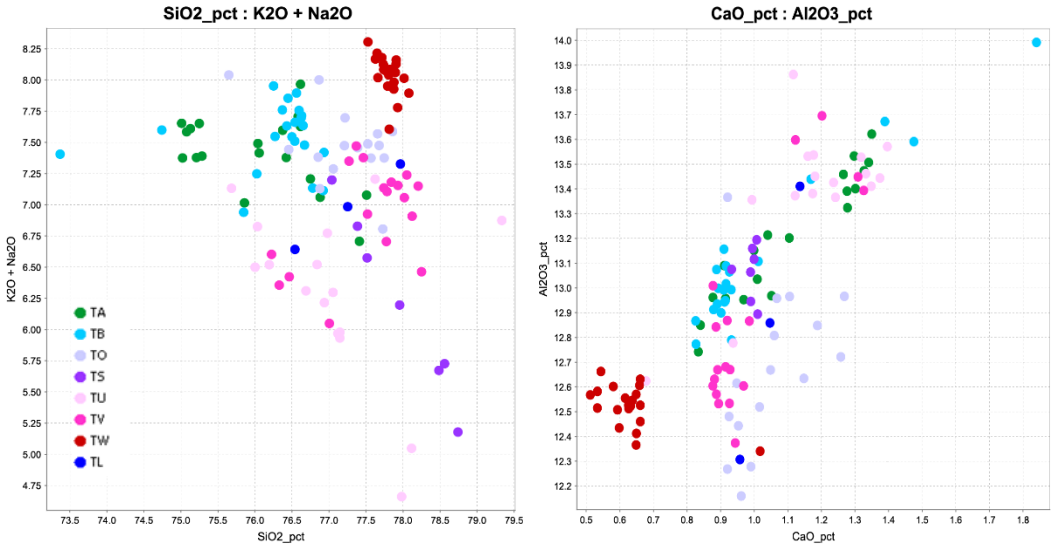

Figure 5.17: Plots displaying EMPA data from tephras sampled from the organic sedimentary deposits of DH1.

TB in light blue (Figure 5.17), has a SiO_2 range of 73.2-77%, CaO from 0.8-1.85% and Al_2O_3 values from 12.76-14%. These points have a wider spread than TA with four points not plotting together, however several of these points plot well between 0.8-1% CaO and Al_2O_3 12.77-13.15%.

TL in dark blue (Figure 5.17), only had three points probed and these range in SiO_2 from 76.5-78%, CaO from 0.95-1.12% and Al_2O_3 12.3-13.4%. The three points have a wide spread.

TO in light purple (Figure 5.17), has SiO_2 values ranging from 75.6-77.9%, CaO 0.92-1.27% and Al_2O_3 12.17-13.8%. These plot well when comparing SiO_2 versus K_2O+Na_2O but have a much wider spread when considering CaO versus Al_2O_3.

TS in dark purple (Figure 5.17), has a SiO_2 range of 77.7-78.8%, CaO range of 0.92-1.2% and Al_2O_3 range of 12.9-13.2%. These have a large spread when

considering SiO2 v K_2O+Na_2O but plot much tighter when comparing CaO and Al_2O_3.

TU in light pink (Figure 5.17), has a spread of SiO_2 from 75.6-79.4%, CaO from 0.92-1.4% and Al_2O_3 from 12.79-13.86%. This data has a wide spread when considering SiO_2 v K_2O+Na_2O but a tighter grouping in a CaO versus Al_2O_3 graph. In the CaO versus Al_2O_3 graph, most of these points group tightly with high Al_2O_3 and CaO values and with only one point plotting with lower Al_2O_3 skewing the group.

TV in dark pink (Figure 5.17), had a spread of SiO_2 from 76.2-78.3%, CaO from 0.86-1.34% and Al_2O_3 from 12.37-13.7%. This sample has a widespread within the SiO_2 versus K_2O+Na_2O graph but shows more of a pattern in the CaO versus Al_2O_3 graph. In this graph, the data splits into two groups, one with high Al_2O_3 and high CaO and the other showing the inverse.

TW in red (Figure 5.17), is the tightest grouping tephra analysed. It has a SiO_2 range of 77.5-78.1%, CaO from 0.5-1.01% and an Al_2O_3 from 12.34-12.67%. This tephra plots separately from other samples in a very distinct cluster.

Chapter 6

Discussion

6.1 Introduction

This thesis has covered many scientific aspects of the Karaka Volcano and investigated it with several different methods. These methods have successfully contributed proof for the existence of the Karaka Volcano and developed its volcano-sedimentary history within the context of the SAVF and AVF. In this chapter, the findings of the research will be discussed, in particular, the new evidence for its volcanic origin, structure, eruptive style, magma type and age.

6.2 Evidence for the Karaka Volcano

Previous evidence for the existence of the volcano at Karaka was established by B. W. Hayward in 2018 and included:

- The geomorphology of the area, in particular, the elevated topography up to 70 m asl, above the average relief of 25 m asl. This topography creates a circular stream pattern around the “central cone”;
- A magnetic survey had shown a magnetic high under the potential scoria cone (Vidanovich, 2018b);
- Boreholes in the area had intercepted lake sediments and soft scoria (Drillwell Exploration NZ Limited, 1996).
- Minor weathered outcrops were discovered including the roadside drain tuff deposit displaying weathered basaltic material; and
- The apparent offset of the Waitemata Group sandstone between the outcrop in Glassons Creek and the depth to the same sandstone in the Drillwell Core.

Evidence for the Karaka Volcano has been broadened in this study with the addition of two drill holes. One drill hole intercepted an organic sedimentary

sequence and the other intercepted fresh basaltic material proving that there has been volcanism occurring here in the past.

The abovementioned drilling results are complemented by the resistivity survey conducted in this study. This survey reveals the extent of deposits between the two drill cores, that is, from the lower proposed lake terrace (DH1) to layers covering the "central cone" of the volcano (DH2). The resistivity survey is also consistent with evidence that constrains the depth of the basalt plug mentioned by (Vidanovich, 2018b), as an area of high resistivity at depth within the profile (Unit 4). Basalts have been shown to display resistivities of 190 to 220 Ω-m (Hyndman & Drury, 1977; Drury, 1979), similar to values seen in units 2 and 4 of the resistivity survey where basalt has been suggested. Although in some studies, hard basalt is found to have much higher resistivity's up to over 1000 Ω-m (Revil *et al.*, 2008).

Clay has a lower resistivity to basalt, matching those seen in Unit 1, representing the clay cover beds (Revil et al., 2008). Lake sediments range in resistivity but, maybe less than 30 Ω-m (Chang *et al.*, 2015). This is similar to the resistivities seen to the south of the resistivity survey, potentially highlighting covered lake sediments.

6.3 Structure of the Karaka Volcano

The initial interpretation of the volcanic structure by Hayward (2018) proposed that the central area of higher topography is a central scoria cone and the high points enclosing the volcano were an ash and tuff ring. Drill hole DH2 (this study) through the upper part of the central hill, did not discover fresh vesicular scoria within 16 m of the surface; instead tuff, with poorly vesicular (dense) basalt lapilli, was discovered, suggesting that the latest form of volcanism was phreatomagmatic in style. Despite the tuff near the surface, there may be a scoria cone beneath. The inclination of the drill hole was not measured but is assumed to be near-vertical. The core from DH2 showed the tuff had horizontal bedding, rather than inclined as tuff beds in some parts of tuff rings or cones can occur

(Francis & Oppenheimer, 2004). The resistivity survey, when compared to the magnetic survey (Vidanovich, 2018b), is consistent with there being a large basalt mass under the tuff sequence which may be due to either a scoria cone or magma plug.

DH1 provides some insight into the volcano-sedimentary history after its eruptive stage. The base of DH1 is hard silt to sand containing diatoms, glass and crystals. Above this is a sequence of dark brown silts and grey tephras. These sediments evolve upwards into a series of sediments that marks the transitions made between a lacustrine and subaerial environment. At the surface, DH1 is covered by clay and silt beds. The sequence also provides the potential for a minimum age of the lake to be determined. The base of DH1, however, does not mark the base of the lake as mentioned earlier, the borehole conducted nearby intercepts organic material to 71 m deep. Which indicates the lake must be considerably older. DH1 also confirms the thick cover beds overlying a potential lake terrace occurring adjacent to the central cone.

The morphology of the tuff ring encircling the “central cone” adopted here is the same as the originally suggested morphology of Hayward (2018). The breach of the tuff ring on the south-eastern side, as Hayward (2018) suggested occurred at the low point where Glasson creek follows out to the Manakau Harbour. The roadside cutting on Urquhart Road where sands were described and sampled is likely where this breach occurred. These sediments are predominantly quartz-rich sands and were likely derived from the erosion of Waitemata Group rock in the surrounding area. These have either been deposited as part of the Puketoka Formation in the surrounding area or after the breach and erosion of the “tuff ring”.

Further subsurface investigations would give more information on the internal structure of the Karaka Volcano and would be most effective if conducted to a greater depth either through deep HQ drilling or deeper, more extensive resistivity surveys. These would be effective either within the “central cone” or within the tuff ring.

6.4 Eruption Style

The deposits retrieved from DH2 show that the eruption style that created the layers exposed in drill core of the Karaka Volcano are from a phreatomagmatic eruption. This is suggested by the fine ash and tuff dominant deposit uncovered. The tuff deposit also encases lithics from the underlying strata and poorly-vesicular basalt lapilli. These types of eruptions occur where water is encountered during an eruption, either from surface water in the form of a lake or in areas underlain by a hard rock that may be conducive of aquifers (Lorenz, 1987; Valentine *et al.*, 2014).

At the location of the volcano on Urquhart Road, artesian water flow is gained from 110 m below the surface. There are two prominent aquifers present in South Auckland, the Waitemata and Kaawa aquifers (Pattle Delamore Partners LTD, 2012). The Kaawa aquifer is around 50 m below the surface and the Waitemata aquifer beneath it to greater depths (Viljevac *et al.*, 2002). This indicates that there is the possibility that the phreatomagmatic eruption is caused by the interaction of rising magma with one or both of the underlying aquifers.

Phreatomagmatic eruptions form tuff rings and or maars (Valentine *et al.*, 2014). The material deposited comes from fragmented county rock and juvenile basaltic material, often forming a small crater (White & Ross, 2011). The deposits formed include tuff beds (Heiken, 1971). Within the Karaka deposit exposed by DH1, there is a bedded tuff sequence, and much of it has randomly embedded poorly vesicular basalt lapilli and lithics within a white tuff. Near the top of the deposit, clay beds contain weathered scoria. This likely indicates tuff weathering rather than the simultaneous deposition of volcanic material and the Kauroa Ash. In DH2 the cover beds are the Kauroa ashes. These have an age of 2.24 (±0.29) to 0.78 Ma (Horrocks, 2000) giving a relative youngest age of Karaka Volcano between these ages.

A fault runs through the ridge slightly to the north of Karaka volcano. In the SAVF volcanic centres often align with faults and in this case may suggest that magma ascent was aided by the Waiau Fault (Kenny *et al.*, 2012).

6.5 Crater Lake

A crater lake that was created by the eruption was first-proposed by Hayward (2018) with evidence from an early water bore and confirmed here through the drilling of DH1. DH1 intersected a succession of brown organic clays and silts, indicating a low energy depositional environment. There are several freshwater low energy depositional environments, including swamps and lakes. The organic sediments, when investigated under the SEM, were comprised predominantly of diatoms. Diatoms contained within this samples appear to be of the Aulacoseira order (Buczko *et al.*, 2010). Often this species is found to create long filaments, and most are found in lakes as a part of phytoplankton. Sometimes they are also found in periphyton of lake fed streams and rivers (Buczko *et al.*, 2010). SEM imagery also revealed a lack of wood or fibrous material within the organic sediments making a paludal/swampy environment less likely.

The presence of a lake and a succession of lake sediments suggests there was an area of lowered topography for these sediments to fill. Evidence comes from the Drillwell Core, stating that mudstone and sandstone become present from 92 m deep Lowering in topography may have occurred through the collapsing and excavating of country-rock in the area.

Tephras have been captured well within this sedimentary lake bed succession. The presence of multiple tephras beds within this lakes indicates longevity of the lake, especially as it has captured several tephras. These tephras are likely derived from the TVZ given the age of the SAVF and the TVZ. As only the top portion of the lake has been intercepted there are likely to be further buried tephras that are correlated to dated eruptions in the TVZ. It appears most tephras are the result of ash falls rather than being reworked.

6.6 Provenance of Lithics

Lithics within the pyroclastic sequence of core DH2 ranged from sandstone to siltstone and were very weathered. The underlying Waitemata Group (Ballance, 1964) is formed from interbedded sand and siltstone. Older drill hole logs in the surrounding area describe interbedded sandstone and siltstone to depth (Drillwell Exploration NZ Limited, 1996). The lithics found within the explosive eruptive deposit are likely from this underlying strata.

6.7 Transitional sediments

The transitional sediments of DH1 are present 5.7 to 7.4 m below the surface and include clays, a light grey pumice, coarse sand and dark brown charred wood.

The sediments recovered here indicate a time in the depositional history of the drill hole where the sediment deposition changed from lacustrine to terrestrial. There is also the possibility that the white pumice layer is the base of the Hamilton Ashes is the Rangitawa Tephra. The wood in the transitional sediments also indicated a potential period where this area was swamp-like rather than a lake.

6.8 Cover beds

Cover beds over eroded volcanic landforms subdue the topography and mask the volcano from the surrounding landscape. Over the Karaka Volcano are several metres of weathered ash cover beds. Cover beds in this area are formed from distal ash from volcanic eruptions in the Taupo Volcanic Zone as well as wind-blown aeolian deposits and paleosols that have since weathered to clay and silt. These cover beds were found in both drill holes DH1 and DH2 and hand augers across the site. Cover beds were also identified in test pits conducted in an analysis of the slope. These beds are inferred to be part of the Hamilton or Kauroa Ash beds which are known to extend as far as South Auckland (Lowe *et al.*, 2001).

On top of the suggested tuff cone, the cover beds are 6.5 m thick, as retrieved from DH2. These range from yellow to red followed by red with yellow mottles.

These are inferred to be the Kauroa Ashes. In DH1 the cover beds are shown to be 5.5 m thick. These are generally yellow to light grey and are inferred to be the Hamilton Ash.

As the Hamilton Ash is younger than the Kauroa Ash, they may expect to be found on top of the proposed scoria cone as well, although due to the elevation they may have been eroded off. Kauroa ash beds were also absent beneath the Hamilton Ash in DH1. This may be due to erosion of these beds from the stream flowing hereafter the crater breach occurred and before this location became subaerial, allowing the Hamilton Ashes to be deposited.

6.9 Distal Tephra Correlation

Tephra beds from the crater lake succession were probed in an attempt to correlate these between other known distal tephras in the Auckland Region and large scale silicic tephras of the North Island. This is useful in providing a chronology of the eruptive events and an upper age constraint on the crater lake.

Of the tephra beds sampled one bed shows possible correlations to the Kidnappers Ignimbrite. The Kidnapper's Ignimbrite was sourced from the Mangakino Volcanic Complex and is dated at ~0.99 Ma, and was the second-largest recorded eruption of the TVZ (Cooper *et al.*, 2012). This produced a silicic fall deposit that covered much of the central North Island including South Auckland. Data collected from matrix glass of pumice from this eruption has been compared to data collected from tephra beds sampled in the Karaka crater lake deposit (Cooper *et al.*, 2016).

Of these tephras, TW was the most neatly clustered and not overlain by other tephra data. This made it a target for correlation. When comparing TW to other tephras, the Kidnappers K2 was the closest result. K2 in both plots of Al_2O_3 versus CaO and FeO versus CaO overlays the TW data (Figure 6.1). Many of the other tephras that were considered from published data had a higher Ca content and as

such did not correlate as well with TW. As TV and TW were taken from the same tephra bed, it is promising that TV also aligns with some of the Kidnappers data.

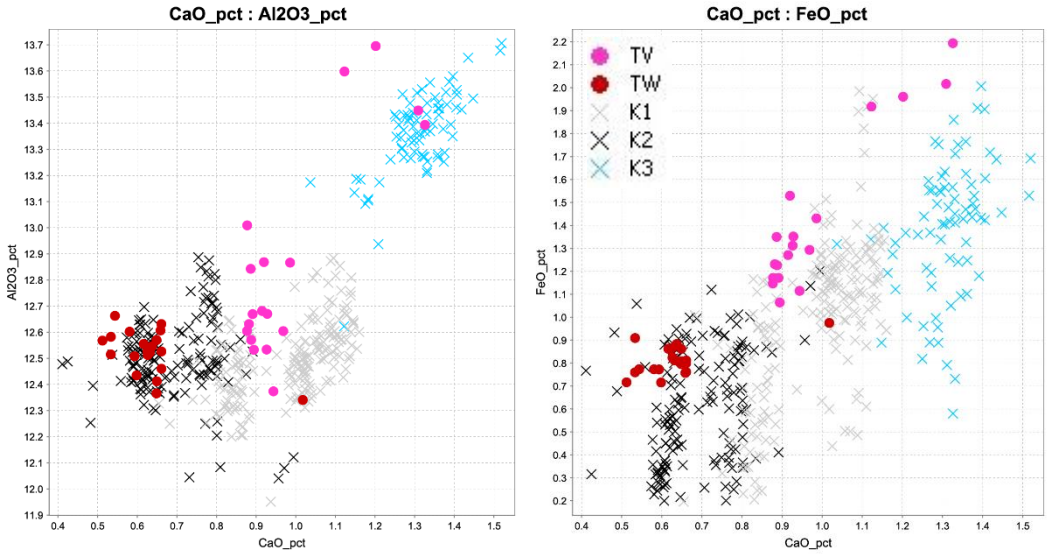

Figure 6.1 EPMA data from tephras of DH1 compared to the Kidnappers Ignimbrite. The K2 dataset is seen to overly TW (Cooper *et al.*, 2016).

6.10 AVF v SAVF

As the Karaka volcano is geographically located between the AVF and the SAVF, it is important to determine to which field the volcano is associated. AVF volcanoes are generally less weathered than their SAVF equivalents due to the age difference between the fields of a minimum of 0.37 Ma years (AVF; 250 ka to 500 ya (Lindsay *et al.*, 2011); SAVF; 1.56-0.51 Ma (Briggs *et al.*, 1994)). Furthermore, the difference between the ages has allowed the older SAVF to become mantled in thick ash beds that were deposited in the interim.

The determination of which field the Karaka Volcano was associated with was aided through the use of major and trace element data obtained from Karaka basalts and comparing their values to Auckland and South Auckland basalts. AVF points have a widespread SiO_2 v Na_2O+K_2O content, so this is not an ideal comparison. The data better separates when comparing Mg and other major elements. In the major element graphs, Karaka Volcano fit better with the SAVF data. Trace element data separates the data well and also follows the same trend

with the Karaka data, with them falling within the SAVF rather than Auckland. When comparing P_2O_5 to trace elemental data, the Karaka data does not correlate well with either volcanic field. Generally, the karaka points fall out of the AVF area and are more closely plotted with the SAVF.

The weathering of the Karaka Volcano, its stratigraphic position beneath the old cover ash beds and elemental data all suggest that the Karaka Volcano is part of the SAVF.

6.11 Magma Type and Origins

The basalt uncovered at the Karaka Volcano is porphyritic with a trachytic to glassy groundmass. Two different types of groundmass occur between small scoria lapilli and relatively larger bombs. Predominant phenocrysts within the basalt were plagioclase, olivine, augite and opaque minerals.

Within the SAVF, there are two types of identified magma (Cook, 2002). These have been displayed on the graphs in Section 4.8. The group that the Karaka Volcano magma falls into was determined using major and trace elemental data. In the SiO_2 versus Na_2O+K_2O graph, the Karaka data falls within the Group A basalts. Two of the Karaka points fall into the alkaline category, and one falls within the subalkaline group.

Major elements compared to Mg are not useful as points fall within both groups of basalt or outside either group. Grouping is tighter when comparing Mg to trace elemental data, with the Karaka data grouping tighter together within the Group B basalts. Trace elements versus P_2O_5 show the Karaka data have a higher P_2O_5 than all of the Group A data points and with some of the trace elements fall within the Group B data, but sometimes they fall just out of it (e.g. Ba, Sr and La).

A possible reason for the variation in the major elemental data is that zeolites are present in the sample. The first indication of zeolites in the basalt arose from EPMA data. Several points that were probed under the assumption that they were

plagioclase. However, these returned anomalous compositions that were not consistent with plagioclase, but instead had zeolite compositions (Table 4.3). The probed crystals were also re-examined under the petrographic microscope, and a possible zeolite is pictured in Figure 4.7.

6.12 Geological history

The formation of the Karaka volcano is likely concurrent with a small plume of rising magma interacting with one or both of the underlying Kaawa or Waitemata aquifers (Figure 6.2a). Interactions between the magma and these aquifers is likely the beginning of the phreatomagmatic eruption that occurred creating the Karaka Volcano (tuff ring and tuff deposit; Figure 6.2b). This eruption has produced poorly vesicular basalt lapilli, tuff material and ejected lithics from the crater. These events, along with the potential for a collapsing crater floor has created the inferred crater lake (Figure 6.2c), that has been intercepted by DH1 (this study) and an earlier bore conducted by Drillwell (1996).

Since the edifice-building eruption, the lake has been infilled with diatomaceous lake sediments and tephra (Figure 6.2d). Infilling would have occurred over time through deposition of these sediments resulting in the lake terrace seen in the field today, covered with a succession of the Hamilton Ash.

The tuff ring produced from the eruption was likely a contributing factor to the prominence of the lake in the past. Over time this ring has been breached through gradational erosion of the deposit (Figure 6.2d). This has led to the topography seen today with the lowered topography of Glassons Creek draining around the Karaka Volcano.

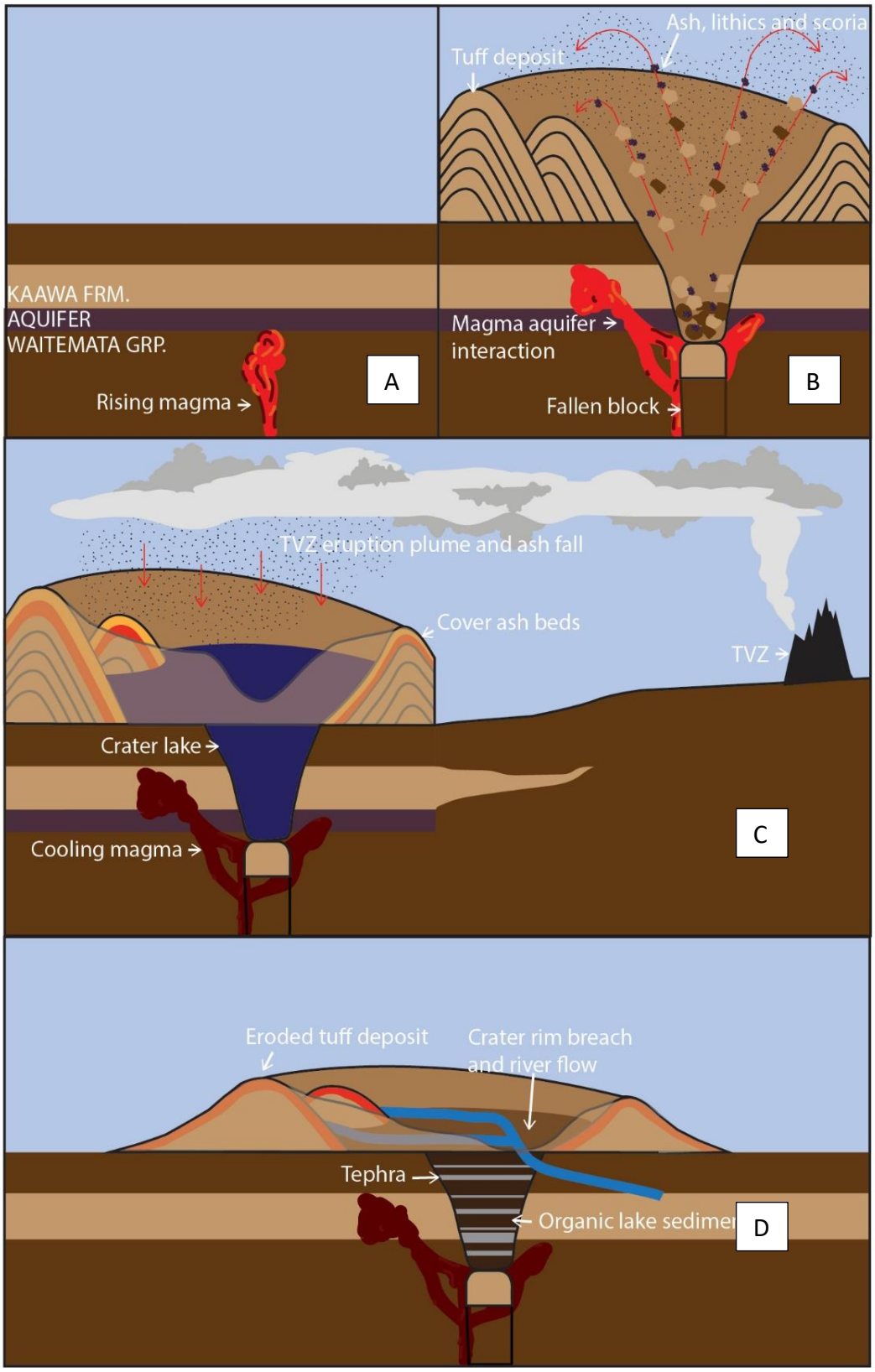

Figure 6.2 The geological history of the Karaka Volcano. (A) The pre-existing topography and subsurface geology. (B) Interactions between rising magma and the underlying aquifer creates an eruption throwing out basalt lapilli, lithics and ash building up a tuff deposit. (C) Filling of the crater lake with water and tephra from distal eruptions in the TVZ. Eruptions in the TVZ also contribute to cover ash beds. (D) Erosion of the tuff ring and in filling in the lake over time has produced the landform seen today.

6.13 Conclusion

The existence of the Karaka Volcano has been proven through the discovery of volcanic material from DH2. This volcanic material included fresh poorly-vesicular basalt lapilli. The basalt has been further investigated and compared to SAVF and AVF basalts and determined to be from the SAVF and the Group B basalts within the SAVF.

DH1 intercepted cover beds, transitional sediments and organic lake sediments and interbedded tephras. The diatoms within the lake sediments confirm a lake environment. The location of this lake within a volcanic tuff ring suggests that the lake environment occurred within the volcanic crater.

Within this study, several lines of evidence have been investigated to place an age on the Karaka Volcano. Evidence includes the proposed age limits of the SAVF, the mantling of the Hamilton and Kauroa Ashes and the possible correlation of the TW tephra to the Kidnappers Ignimbrite. This provides an age range for the Karaka Volcano of 1.56 – 0.99 Ma.

References

Alloway, B., Westgate, J., Pillans, B., Pearce, N., Newnham, R., Byrami, M., & Aarburg, S. (2004). Stratigraphy, age and correlation of middle Pleistocene silicic tephras in the Auckland region, New Zealand: a prolific distal record of Taupo Volcanic Zone volcanism. *New Zealand Journal of Geology and Geophysics, 47*(3), 447-479.

Auckland Council. (2019). *GeoMaps Public* [Map]. https://geomapspublic.aucklandcouncil.govt.nz/viewer/index.html. Retrieved 26/07/2019, 2019.

Ballance, P. F. (1964). The sedimentology of the Waitemata Group in the Takapuna Section, Auckland. *New Zealand Journal of Geology and Geophysics, 7*(3), 466-499.

Ballance, P. F. (1976). Evolution of the Upper Cenozoic magmatic arc and plate boundary in northern New Zealand. *Earth and Planetary Science Letters, 28*, 356-370.

Bebbington, M. S., & Cronin, S. J. (2011). Spatio-temporal hazard estimation in the Auckland Volcanic Field, New Zealand, with a new event-order model. *Bulletin of Volcanology, 73*(1), 55-72.

Bradshaw, J. D. (1989). Cretaceous Geotectonic Patterns in the New-Zealand Region. *Tectonics, 8*(4), 803-820.

Briggs, R. M., Itaya, T., Lowe, D. J., & Keane, A. J. (1989). Ages of the Pliocene—Pleistocene Alexandra and Ngatutura Volcanics, western North Island, New Zealand, and some geological implications. *New Zealand Journal of Geology and Geophysics, 32*(4), 417-427.

Briggs, R. M., Okada, T., Itaya, T., Shibuya, H., & Smith, I. E. M. (1994). K‐Ar ages, paleomagnetism, and geochemistry of the South Auckland volcanic field, North Island, New Zealand. *New Zealand Journal of Geology and Geophysics, 37*(2), 143-153.

Buczko, K., Ognjanova-Rumenova, N., & Magyari, E. (2010). Taxonomy, morphology and distribution of some Aulacoseira taxa in Glacial Lakes in the South Carpathian Region. . *Polish Botanical Journal, 55*(1).

Cassata, W. S., Singer, B. S., & Cassidy, J. (2008). Laschamp and Mono Lake geomagnetic excursions recorded in New Zealand. *Earth and Planetary Science Letters, 268*(1-2), 76-88.

Chang, P.-Y., Chang, L.-C., Lee, T.-Q., Chan, Y.-C., & Chen, H.-F. (2015). Examining lake-bottom structures with the resistivity imaging method in Ilan's Da-Hu Lake in Northeastern Taiwan. *Journal of Applied Geophysics, 119*, 170-177.

Cook, C. (2002). *Petrogenesis and Evolution of Alkalic Basaltic Magmas in a Continental Intraplate Setting: The South Auckland Volcanic Field, New Zealand.* thesis, The University of Waikato, Hamilton.

Cook, C., Briggs, R. M., Smith, I. E. M., & Maas, R. (2005). Petrology and geochemistry of intraplate basalts in the South Auckland Volcanic Field, New Zealand: Evidence for two coeval magma suites from distinct sources. *Journal of Petrology, 46*(3), 473-503.

Cooper, G. F., Wilson, C. J. N., Millet, M. A., & Baker, J. A. (2016). Generation and Rejuvenation of a Supervolcanic Magmatic System: a Case Study from Mangakino Volcanic Centre, New Zealand. *Journal of Petrology, 57*(6), 1135-1170.

Cooper, G. F., Wilson, C. J. N., Millet, M. A., Baker, J. A., & Smith, E. G. C. (2012). Systematic tapping of independent magma chambers during the 1 Ma Kidnappers supereruption. *Earth and Planetary Science Letters, 313*, 23-33.

Drillwell Exploration NZ Limited. (1996). *New Zealand Geotechnical Database - Daily Log Sheet for Urquart Road Karaka*. https://www.nzgd.org.nz/ARCGISMapViewer/mapviewer.aspx.

Drury, M. J. (1979). Electrical-Resistivity Models of the Oceanic-Crust Based on Laboratory Measurements on Basalts and Gabbros. *Geophysical Journal of the Royal Astronomical Society, 56*(2), 241-253.

Edbrooke, S. W. (Cartographer). (2001). Geology of the Auckland area : 1:250,000.

Fisher, R. V., & Schmincke, H.-U. (1984). *Pyroclastic Rocks*. Germany: Springer-Verlag.

Francis, P., & Oppenheimer, C. (2004). *Volcanoes*. Oxford: Oxford University Press.

Furlong, K. P., & Kamp, P. J. J. (2009). The lithospheric geodynamics of plate boundary transpression in New Zealand: Initiating and emplacing subduction along the Hikurangi margin, and the tectonic evolution of the Alpine Fault system. *Tectonophysics, 474*(3-4), 449-462.

Google Earth Pro. (2019). *Karaka Volcano*.

Hayward, B. (2015). Helvetia Volcano - a newly recognised tuff ring and maar in the South Auckland Volcanic Field. *Geocene, 12*, 10-13.

Hayward, B. W. (2018). *Is there a volcano at Karaka?* Unpublished Report BWH 184/18. 16p.

Hayward, B. W., Black, P. M., Smith, I. E. M., Ballance, P. F., TItaya, T., Doi, M., Takagi, M., Bergman, S. A., C. J., Herzer, R. H., & Robertson, D. J. (2001). K‐Ar ages of early Miocene arc‐type volcanoes in northern New Zealand. *New Zealand Journal of Geology and Geophysics, 44*(2), 285.

Hayward, B. W., & Brook, F. J. (1984). Lithostratigraphy of the Basal Waitemata Group, Kawau Subgroup (New), Auckland, New-Zealand. *New Zealand Journal of Geology and Geophysics, 27*(2), 101-123.

Hayward, B. W., Murdoch, G., & Maitland, G. (2011). *Volcanoes of Auckland*. Auckland, New Zealand: Auckland University Press.

Heiken, G. H. (1971). Tuff Rings: Examples from the Fort Rock-Christmas Lake Valley Bain, South-Central Oregon. *Journal of Geophysical Research, 76*(23), 5615-5626.

Horrocks, J. L. (2000). *Stratigraphy, Chronology and Correlation of the Plio-Pleistocene (c. 2.2-0.8 Ma) Kauroa Ash Sequence, Western Central North Island, New Zealand.* PhD thesis, University of Waikato, Hamilton.

Horspool, N. A., Savage, M. K., & Bannister, S. (2006). Implications for intraplate volcanism and back-arc deformation in northwestern New Zealand, from joint inversion of receiver functions and surface waves. *Geophysical Journal International, 166*(3), 1466-1483.

Hyndman, R. D., & Drury, M. J. (1977). Physical Properties of Basalts, Gabbros, and Ultramafic Rocks from DSDP Leg 37. *Physical Properties of Basalt*.

Kamp, P. J. J., & Lowe, D. J. (1981). Quaternary stratigraphy, landscape, and soils of the Hamilton Basin. *In R. M. Briggs (Ed.), Geological Society of New Zealand Miscellaneous Publication, 29B*, 14-28.

Kamp, P. J. J., Tripathi, A., & Nelson, C. S. (2008a). Te Kuiti Group (Late Eocene - Oligocene) Lithostratigraphy east of the Taranaki Basin in central-western North Island, New Zealand. *Ministry of Economic Development, Petroleum Report Series*.

Kamp, P. J. J., Tripathi, A. R. P., & Nelson, C. S. (2008b). Stratigraphic columns and correlations for the Late Eocene - Oligocene Te Kuiti Group, central-western North Island, New Zealand. *Petroleum Report Series, PR3901*.

Kenny, J. A., Lindsay, J. M., & Howe, T. M. (2012). Post-Miocene faults in Auckland: insights from borehole and topographic analysis. *New Zealand Journal of Geology and Geophysics, 55*(4), 323-343.

Laird, M. G., & Bradshaw, J. D. (2004). The break-up of a long-term relationship: the Cretaceous separation of New Zealand from Gondwana. *Gondwana Research, 7*(1), 273-286.

Lander, S. G. (2016). *Geotechnical Investigation Report.* Lander Geotechnical Consultants Limited.

Leonard, G. S., Calvert, A. T., Hopkins, J. L., Wilson, C. J. N., Smid, E. R., Lindsay, J. M., & Champion, D. E. (2017). High-precision 40Ar/39Ar dating of Quaternary basalts from Auckland Volcanic Field, New Zealand, with

implications for eruption rates and paleomagnetic correlations. *Journal of Volcanology and Geothermal Research, 343*, 60-74.

Lindsay, J. M., Leonard, G. S., Smid, E. R., & Hayward, B. W. (2011). Age of the Auckland Volcanic Field: a review of existing data. *New Zealand Journal of Geology and Geophysics, 54*(4), 379-401.

Lorenz, V. (1987). Phreatomagmatism and its relevance. *Chemical Geology, 62*, 149-156.

Lowe, D. J. (2008). *Stop 2 Kainui silt loam and Naike clay, Gordonton Rd [Hamilton Basin]*. Presented at the Australian and New Zealand 4th Joint Soils Conference.

Lowe, D. J. (2010). *Pukekohe silt loam, Pukekohe Hill*. Presented at the 19th World Soils Congress, International Union of Soil Sciences.

Lowe, D. J. (2011). Tephrochronology and its application: A review. *Quaternary Geochronology, 6*(2), 107-153.

Lowe, D. J., Pearce, N. J. G., Jorgensen, M. A., Kuehn, S. C., Tryon, C. A., & Hayward, C. L. (2017). Correlating tephras and cryptotephras using glass compositional analyses and numerical and statistical methods: Review and evaluation. *Quaternary Science Reviews, 175*, 1-44.

Lowe, D. J., Tippett, J. M., Kamp, P. J. J., Liddell, I. J., Briggs, R. M., & Horrocks, J. L. (2001). *Ages on weathered Plio-Pleistocene tephra sequences, western North Island, New Zealand*. Presented at the CDERAD editeur, GoudeL us Dossiers de f'ArcMo-Logis.

McDougall, I., Polach, H. A., & Stipp, J. J. (1969). Excess radiogenic argon in young subaerial basalts from the Auckland volcanic field, New Zealand. *Geochimica et Coemochimica Acta, 33*, 1485-1520.

McGee, L. E., Smith, I. E. M., Millet, M. A., Handley, H. K., & Lindsay, A. M. (2013). Asthenospheric Control of Melting Processes in a Monogenetic Basaltic System: a Case Study of the Auckland Volcanic Field, New Zealand. *Journal of Petrology, 54*(10), 2125-2153.

Miyashiro, A. (1978). Nature of Alkalic Volcanic Rock Series. *Contributions to Mineralogy and Petrology, 66*(1), 91-104.

Molloy, C., Shane, P., & Augustinus, P. (2009). Eruption recurrence rates in a basaltic volcanic field based on tephra layers in maar sediments: Implications for hazards in the Auckland volcanic field. *Geological Society of America Bulletin, 121*(11-12), 1666-1677.

Mortimer, N. (2015). Remnants of a Distant Past - Overview. In I. J. Graham (Ed.), *A Continent on the Move* (Second ed.). New Zealand: The Geoscience Society of New Zealand and GNS Science.

Mullane, K. J. C. (2015). *Geophysical characterisation of the Onewhero and Kellyville volcanic complexes, South Auckland Volcanic Field.* thesis, University of Waikato, University of Waikato.

Needham, A. J., Lindsay, J. M., Smith, I. E. M., Augustinus, P., & Shane, P. A. (2011). Sequential eruption of alkaline and sub-alkaline magmas from a small monogenetic volcano in the Auckland Volcanic Field, New Zealand. *Journal of Volcanology and Geothermal Research, 201*(1-4), 126-142.

Nemeth, K., Agustin-Flores, J., Briggs, R. M., Cronin, S. J., Kereszturi, G., Lindsay, J. M., Pittari, A., & Smith, I. E. M. (2012). *Monogenetic volcanism of the South Auckland and Auckland Volcanic Fields*. Presented at the IAVCEI – CMV/CVS – IAS 4IMC Conference.

Nemeth, K., & Kereszturi, G. (2015). Monogenetic volcanism: personal views and discussion. *International Journal of Earth Sciences, 104*(8), 2131-2146.

Pattle Delamore Partners LTD. (2012). *Karaka Rural Urban Boundary Waitemata Aquifer Recharge Assessment.* Auckland. https://www.aucklandcouncil.govt.nz/plans-projects-policies-reports-bylaws/our-plans-strategies/unitary-plan/history-unitary-plan/documentssection32reportproposedaup/appendix-3-2-10.pdf.

Rafferty, W. J. (1977). *The Volcanic Geology and Petrology of South Auckland.* thesis, University of Auckland, Auckland.

Rafferty, W. J., & Heming, R. F. (1979). Quaternary Alkalic and Sub-Alkalic Volcanism in South Auckland, New-Zealand. *Contributions to Mineralogy and Petrology, 71*(2), 139-150.

Revil, A., Finizola, A., Piscitelli, S., Rizzo, E., Ricci, T., Crespy, A., Angeletti, B., Balasco, M., Cabusson, S. B., Bennati, L., et al. (2008). Inner structure of La Fossa di Vulcano (Vulcano Island, southern Tyrrhenian Sea, Italy) revealed by high-resolution electric resistivity tomography coupled with self-potential, temperature, and CO2 diffuse degassing measurements. *Journal of Geophysical Research-Solid Earth, 113*(B7).

Schofield, J. C. (1958a). Pliocene shell beds south of the Manukau Harbour. *New Zealand Journal of Geology and Geophysics, 1*(2), 247-255.

Schofield, J. C. (1958b). Notes on volcanism and structure in Franklin County. *New Zealand Journal of Geology and Geophysics, 1*(3), 541-559.

Smith, I. E. M., Blake, S., Wilson, C. J. N., & Houghton, B. F. (2008). Deep-seated fractionation during the rise of a small-volume basalt magma batch: Crater Hill, Auckland, New Zealand. *Contributions to Mineralogy and Petrology, 155*(4), 511-527.

Smith, I. E. M., Okada, T., Itaya, T., & Black, P. M. (1993). Age Relationships and Tectonic Implications of Late Cenozoic Basaltic Volcanism in Northland,

New-Zealand. *New Zealand Journal of Geology and Geophysics, 36*(3), 385-393.

Sporli, K. B., & Eastwood, V. R. (1997). Elliptical boundary of an intraplate volcanic field, Auckland, New Zealand. *Journal of Volcanology and Geothermal Research, 79*(3-4), 169-179.

Sutherland, R., & King, P. (2015). Shifting Ground - leaving Gondwana behind. In I. J. Graham (Ed.), *A Continent on the Move* (2nd ed., pp. 125-146). New Zealand: Geoscience Society of NZ, GNS Science.

Tripathi, A. R. P., Kamp, P. J., & Nelson, C. S. (2008). *Basin Analysis of the Late Eocene - Oligocene Te Kuiti Group, Western North Island, New Zealand.* PhD thesis, University of Waikato, Hamilton.

Valentine, G. A., Graettinger, A. H., & Sonder, I. (2014). Explosion depths for phreatomagmatic eruptions. *Geophysical Research Letters, 41*, 3045-3051.

Vidanovich, P. (2018a). *Karaka Volcano Study Summary Report.*

Vidanovich, P. (2018b). *Urquhart Road Ground Magnetic Survey Report.* PVC Ltd., New Zealand.

Viljevac, Z., Murphy, G., Smaill, A., Crowcroft, G., & Bowden, D. (2002). *South Auckland Groundwater, Kaawa Aquifer Recharge Study And Management Of The Volcanic And Kaawa Aquifers.* http://www.aucklandcity.govt.nz/council/documents/technicalpublications/TP133%20-%20South%20Auckland%20Groundwater,%20Kaawa%20Aquifer%20Recharge%20Study%20and%20Management%20of%20the%20Volcanic%20and%20Kaawa%20Aquifers%202002%20(part%201).pdf.

White, J. D. L., & Ross, P.-S. (2011). Maar0diatreme volcanoes: A review. *Journal of Volcanology and Geothermal Research, 201*, 1-29.

Appendices

Appendix 1:

XRD Peak Analysis

SAMPLE CA

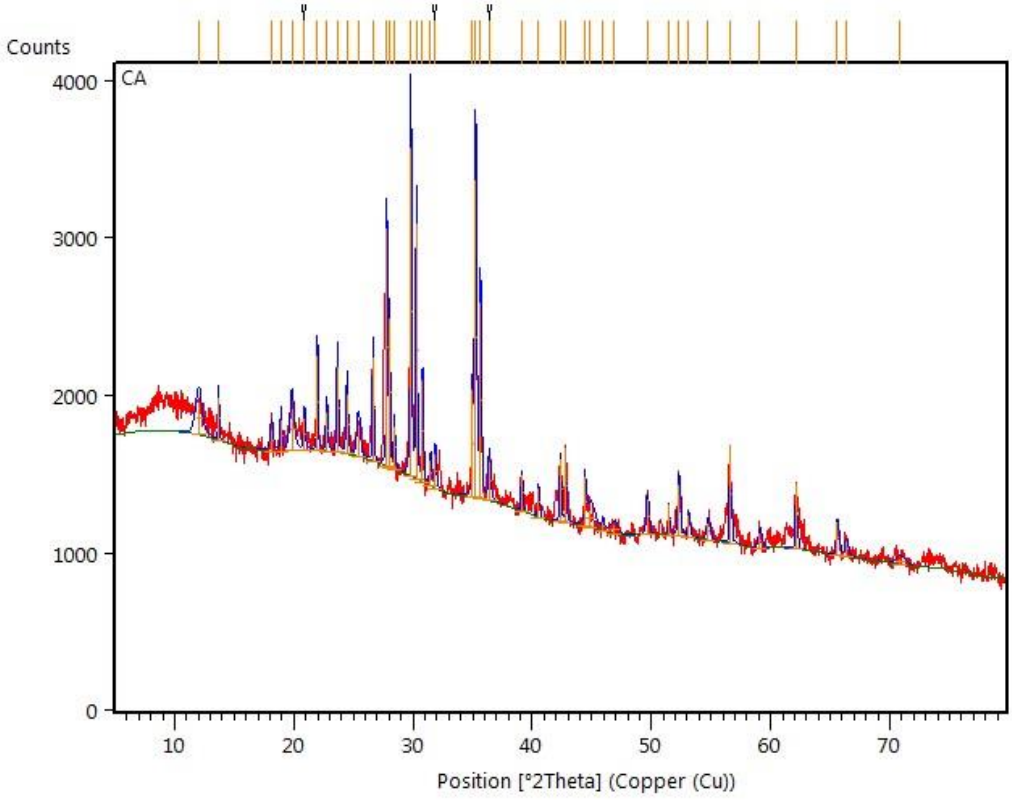

SAMPLE CB

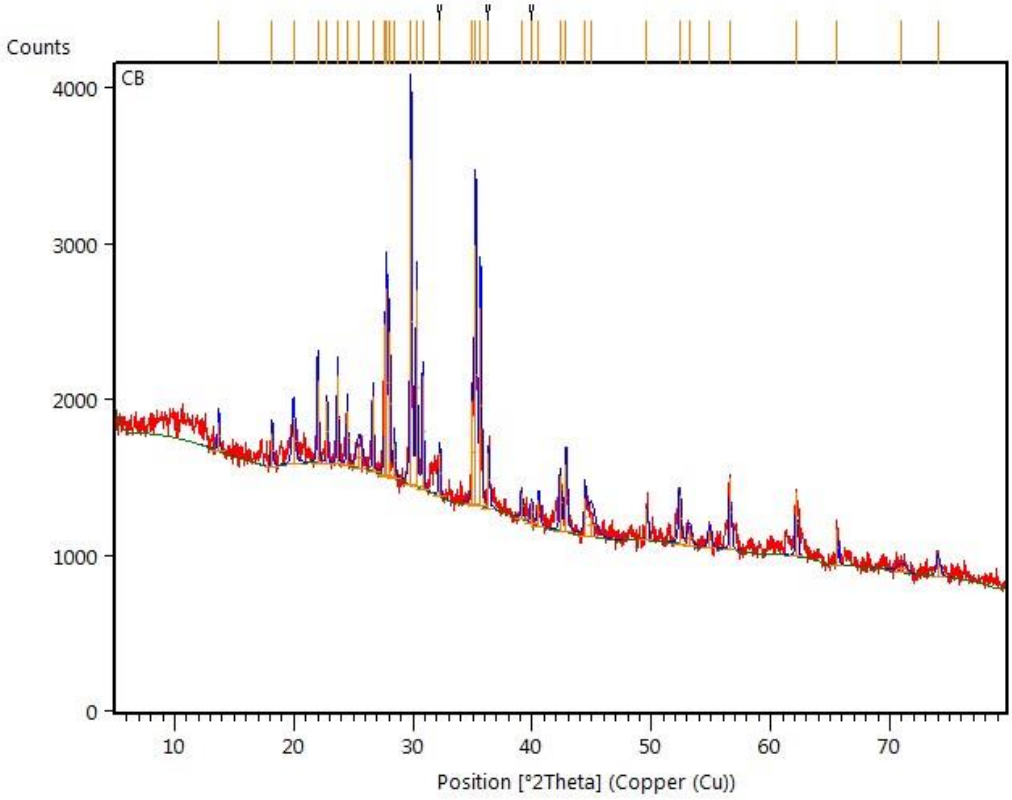

Appendix 2:

EMPA – Basalt Minerals

Sample Name	SiO2	TiO2	Al2O3	FeO	MgO	CaO	Na2O	K2O	Total
Plagioclase-01	51.33	0.00	30.76	0.47	0.16	13.52	3.44	0.19	99.87
Plagioclase-02	51.16	0.00	31.06	0.45	0.12	13.71	3.40	0.17	99.91
B1-P-1	48.42	0.00	33.04	0.42	0.04	16.08	2.35	0.10	100.36
B1-P-2	67.56	0.00	21.86	0.09	0.07	0.39	8.12	0.94	98.08
B1-P-3m	52.40	-2.68	29.10	0.70	0.11	12.18	4.25	0.62	96.05
B1-P-4a	56.40	0.00	27.82	0.22	0.00	9.53	5.69	0.34	99.66
B1-P-4b	55.12	0.00	28.51	0.15	0.02	10.71	5.32	0.32	99.83
B1-P-5	52.63	13.45	27.72	1.27	0.32	11.41	4.34	0.76	111.13
B1-P-6	90.81	0.05	3.72	0.09	0.01	0.03	1.43	0.80	96.13
B2-P-1	53.69	0.00	29.40	0.39	0.03	11.85	4.60	0.33	99.96
B2-P-2	53.30	0.34	29.19	0.68	0.09	11.62	4.45	0.58	99.67
B2-P-3	55.08	1.40	27.59	0.79	0.10	10.21	5.26	0.85	100.43
B2-P-4	47.86	16.15	12.24	8.37	0.43	3.09	1.08	0.81	89.24
B2-P-5	53.54	1.71	26.71	1.86	0.36	10.38	4.65	1.12	99.21
M-P-1	44.84	10.06	11.32	8.54	2.03	5.18	0.14	0.76	82.10
M-P-2	53.13	0.05	28.90	0.72	0.08	11.61	4.47	0.68	98.96
M-P-3	57.28	0.24	27.28	1.14	0.34	10.27	4.19	0.75	100.74
M-P-4	57.73	0.47	27.38	1.24	0.33	10.16	3.54	0.73	100.84
M-P-8	67.82	0.00	21.81	1.13	0.19	0.34	7.60	0.26	98.90
M-P-9a	55.87	0.00	27.77	0.18	0.03	9.61	5.53	0.42	98.99
M-P-9b	54.93	0.11	28.38	0.13	0.00	10.78	5.15	0.36	99.48
M-P-9c	56.01	0.00	27.94	0.17	0.01	9.84	5.60	0.36	99.58
M-P-9d	56.41	0.00	27.94	0.13	0.01	9.40	5.78	0.35	99.67
M-P-9e	55.30	0.00	28.34	0.18	0.00	10.50	5.32	0.33	99.64

Sample Name	SiO2	TiO2	Al2O3	FeO	MgO	CaO	Na2O	K2O	Total
M-P-9f	54.44	0.00	28.67	0.14	0.00	11.06	5.07	0.30	99.38
M-P-10	67.10	0.00	20.41	1.29	0.29	0.20	7.47	0.63	96.78
M-P-11	54.15	0.00	28.71	0.51	0.05	11.19	4.81	0.63	99.41
M-P-12	66.59	0.00	20.45	0.17	0.05	2.31	7.14	0.29	96.73
M-P-13	52.75	0.00	29.78	0.61	0.05	12.50	4.13	0.31	99.81
M-P-14	57.06	0.05	26.84	0.40	0.04	8.82	5.96	0.47	99.16
M-P-15	68.88	0.00	21.57	0.06	0.00	0.29	9.09	0.12	99.90
M-P-16	54.84	0.00	28.47	0.55	0.06	10.69	5.16	0.38	99.76
Plagioclase-03	51.19	0.00	30.80	0.44	0.15	13.71	3.62	0.18	99.91
Plagioclase-04	51.30	0.00	31.03	0.48	0.13	13.77	3.56	0.18	100.27
M-P-16a	52.30	0.02	1.75	25.16	22.62	1.00	0.03	0.03	102.88
M-P-17	59.53	0.00	25.84	1.48	0.81	0.79	4.03	4.85	92.48
M-P-18	97.75	0.00	0.05	0.07	0.00	0.01	0.00	0.03	97.88
M-P-19	96.93	0.00	0.04	0.05	0.00	0.02	0.00	0.04	97.03
M-P-20	66.60	0.00	22.93	0.23	0.00	0.15	7.75	1.41	97.66
M-P-21	55.67	0.00	28.17	0.13	0.01	9.93	5.59	0.36	99.50
M-P-22	56.54	0.00	27.00	0.41	0.03	9.21	5.88	0.60	99.08
Plagioclase-05	51.46	0.16	31.00	0.48	0.15	13.78	3.11	0.19	100.15
Plagioclase-06	51.06	0.00	30.80	0.44	0.13	13.35	3.56	0.17	99.34

Pyroxene

Sample Name	SiO2	TiO2	Al2O3	FeO	MnO	MgO	CaO	Na2O	K2O	Cr2O3	Total
kakanui-01	50.55	0.66	8.78	6.23	0.12	16.68	15.68	1.33	0.00	0.14	100.19
kakanui-02	50.82	0.91	8.65	6.53	0.10	16.56	15.72	1.29	0.01	0.19	100.78
hypersthene-01	54.66	0.09	0.81	15.28	0.49	27.26	1.16	0.00	0.01	0.62	100.37
hypersthene-02	54.20	0.08	0.83	15.38	0.44	26.91	1.20	0.01	0.00	0.51	99.56
B1-Ag-1	44.24	11.45	10.30	9.40	0.13	10.59	20.93	0.82	0.11	0.00	107.98
B1-Ag-2	44.79	3.90	6.79	8.50	0.11	11.51	22.51	0.56	0.01	0.17	98.84
B1-Ag-3	43.63	12.33	8.64	9.49	0.09	10.57	21.45	0.69	0.01	0.03	106.92
B1-Ag-4	44.29	3.83	7.72	8.81	0.13	11.52	21.93	0.63	0.03	0.02	98.91
B1-Ag-5	42.15	11.03	9.06	9.52	0.18	10.43	21.93	0.65	0.04	0.06	105.06
B1-Ag-6a	48.73	1.54	4.11	8.62	0.17	13.35	21.63	0.40	0.01	0.03	98.59
B1-Ag-6b	44.37	3.58	8.19	9.23	0.14	11.11	21.51	0.64	0.01	0.04	98.83
B1-Ag-7	44.75	3.99	7.91	8.97	0.11	11.34	21.63	0.61	0.01	0.08	99.39
B1-Ag-8	44.84	3.73	8.29	8.26	0.12	11.05	21.99	0.58	0.02	0.09	98.96
B1-Ag-9	45.69	3.00	7.27	9.04	0.13	11.63	21.37	0.70	0.01	0.06	98.90
B1-Ag-10a	48.81	1.65	4.23	8.76	0.14	13.57	21.92	0.43	0.02	0.16	99.69
B1-Ag-10b	70.94	1.14	6.91	8.70	0.14	0.97	2.30	1.05	2.62	0.00	94.77
B1-Ag-11	43.08	13.51	8.78	9.58	0.16	10.70	21.18	0.69	0.01	0.05	107.74
B1-Ag-12	44.68	9.06	7.92	9.11	0.14	11.37	21.24	0.63	0.01	0.08	104.24
B1-Ag-13	47.67	3.83	9.91	9.66	0.16	9.32	19.36	0.72	0.16	0.00	100.79
B2-Ag-1	54.04	0.10	29.35	0.54	0.02	0.08	10.70	5.23	0.36	0.00	100.43
B2-Ag-2	47.55	2.21	4.74	9.56	0.18	12.68	21.23	0.45	0.01	0.00	98.62
B2-Ag-3	44.70	3.37	7.93	8.93	0.14	11.30	21.82	0.62	0.01	0.05	98.86

Sample Name	SiO2	TiO2	Al2O3	FeO	MnO	MgO	CaO	Na2O	K2O	Cr2O3	Total
B2-Ag-4	45.58	3.34	7.54	8.56	0.13	11.68	21.63	0.60	0.01	0.00	99.08
B2-Ag-5	44.96	3.07	7.71	9.00	0.12	11.49	21.69	0.63	0.00	0.09	98.77
B2-Ag-6	48.40	2.00	4.47	9.12	0.14	13.02	21.15	0.40	0.01	0.00	98.71
B2-Ag-7	36.38	0.12	0.94	30.82	0.28	24.23	0.39	0.04	0.06	0.00	93.27
B2-Ag-8	45.63	2.72	7.48	8.87	0.07	11.62	21.75	0.54	0.01	0.00	98.69
B2-Ag-9	48.90	2.08	4.16	8.64	0.16	13.61	21.44	0.44	0.04	0.00	99.45
B2-Ag-10	48.09	2.35	4.67	9.23	0.12	13.22	21.44	0.45	0.00	0.08	99.65
B2-Ag-11	44.20	4.35	8.31	8.90	0.11	11.06	21.56	0.63	0.01	0.00	99.14
B2-Ag-12	46.75	2.18	6.50	8.52	0.12	12.33	21.90	0.61	0.00	0.00	98.90
B2-Ag-13	45.54	3.03	7.34	9.08	0.13	11.60	21.71	0.60	0.01	0.05	99.10
Kakanui-01	41.60	12.13	10.71	12.23	0.16	8.45	16.23	1.15	0.43	0.00	103.08
Kakanui-02	50.94	0.72	8.74	6.33	0.12	16.65	15.88	1.21	0.00	0.19	100.77
Hypersthine	54.39	0.13	0.82	15.23	0.47	27.11	1.18	0.01	0.00	0.64	99.99
Hypersthine	54.58	0.13	0.81	15.39	0.43	27.32	1.18	0.02	0.00	0.58	100.45
M-Ag-1	45.01	2.82	7.98	8.96	0.12	11.25	21.68	0.59	0.01	0.00	98.42
M-Ag-2	41.28	2.02	5.98	7.80	0.13	10.53	24.82	0.50	0.01	0.00	93.08
M-Ag-3	45.75	3.11	7.63	8.77	0.12	11.84	21.85	0.60	0.01	0.08	99.76
M-Ag-4	44.20	3.61	8.03	8.92	0.10	11.37	21.96	0.56	0.03	0.00	98.78
M-Ag-5	45.87	2.35	7.29	8.90	0.12	11.53	21.78	0.62	0.01	0.00	98.46
M-Ag-6	37.85	0.14	0.01	24.43	0.32	37.65	0.25	0.02	0.00	0.00	100.67
M-Ag-7	43.63	3.64	9.20	9.07	0.10	10.74	21.87	0.58	0.00	0.01	98.83
M-Ag-8	44.93	3.40	7.93	9.13	0.13	11.21	21.98	0.58	0.01	0.00	99.30
M-Ag-9	45.44	2.92	7.55	8.74	0.10	11.41	21.84	0.56	0.00	0.00	98.56
M-Ag-10	47.04	1.68	4.28	8.84	0.20	12.74	22.83	0.47	0.01	0.00	98.09

Sample Name	SiO2	TiO2	Al2O3	FeO	MnO	MgO	CaO	Na2O	K2O	Cr2O3	Total
M-Ag-11	43.37	3.60	8.83	9.25	0.12	10.63	21.83	0.61	0.02	0.05	98.31
M-Ag-12	53.52	0.07	29.64	0.65	0.01	0.07	11.21	4.99	0.34	0.11	100.61
M-Ag-13	44.23	3.51	8.46	9.22	0.12	10.92	21.47	0.69	0.01	0.00	98.62
Kakanui-05	50.62	0.72	8.72	6.30	0.15	16.72	15.91	1.27	0.01	0.22	100.63
Kakanui-06	50.72	0.69	8.76	6.31	0.16	16.65	15.91	1.24	0.01	0.02	100.46
hypersthine-05	54.56	0.01	0.94	14.94	0.44	27.07	1.24	0.01	0.00	0.63	99.84
hypersthine-06	54.23	0.13	0.82	15.06	0.44	27.02	1.24	0.02	0.00	0.70	99.65
B2-G-1	65.07	2.65	7.82	4.38	0.05	0.79	2.53	0.35	0.52	0.04	84.18
B2-G-2	50.21	0.80	18.52	11.48	0.01	2.33	1.33	1.00	1.12	0.00	86.81
B2-G-3	37.75	1.90	16.65	7.03	0.08	0.24	4.26	5.00	0.66	0.00	73.55
B2-G-4	48.01	1.96	20.66	9.41	0.16	1.83	4.94	3.40	2.20	0.16	92.73
B2-G-5	51.16	2.19	18.47	9.75	0.18	2.11	5.76	2.56	1.70	0.00	93.87

Olivine

Sample Name	SiO2	TiO2	Al2O3	FeO	MnO	MgO	CaO	Cr2O3	Total
Springwater-01	39.05	0.03	0.00	16.88	0.26	43.29	0.00	0.00	99.51
Springwater-02	38.78	0.00	0.00	16.98	0.26	43.31	0.00	0.00	99.33
B1-Ol-1	37.74	0.04	0.05	23.02	0.16	38.63	0.08	0.00	99.70
B1-Ol-2a	37.88	0.05	0.05	23.85	0.23	36.99	0.13	0.00	99.19
B1-Ol-2b	47.53	1.24	17.77	11.34	0.17	2.61	8.04	0.00	88.70
B1-Ol-2-inc	44.22	1.51	15.35	10.11	0.12	5.21	15.13	0.03	91.68
B1-Ol-3	37.70	0.00	0.04	23.98	0.17	37.59	0.13	0.00	99.61
B1-Ol-4	37.76	0.00	0.06	23.20	0.20	38.32	0.11	0.01	99.65
B1-Ol-5	38.02	0.06	0.06	22.71	0.29	38.12	0.20	0.00	99.47
B1-Ol-6	38.12	0.05	0.03	24.41	0.25	37.83	0.16	0.01	100.86
B1-Ol-7	37.54	0.05	0.02	24.25	0.29	37.45	0.23	0.03	99.87
B1-Ol-8	37.88	0.07	0.04	24.02	0.32	38.30	0.22	0.00	100.83
B1-Ol-9	37.59	0.00	0.00	23.93	0.23	37.46	0.22	0.04	99.47
B1-Ol-10	39.64	1.36	15.74	11.57	0.12	1.60	10.05	0.00	80.09
B1-Ol-11	37.24	0.02	0.00	24.53	0.21	36.89	0.10	0.00	99.00
B1-Ol-12	37.52	0.05	0.06	23.65	0.27	37.37	0.23	0.00	99.14
B2-Ol-1	36.44	0.05	0.74	31.33	0.15	24.86	0.32	0.04	93.92
B2-Ol-2	35.34	0.05	0.76	32.33	0.23	24.42	0.33	0.00	93.46
B2-Ol-3	36.65	0.07	0.38	28.83	0.19	31.34	0.19	0.03	97.67
B2-Ol-4	37.52	0.09	0.07	23.67	0.22	38.15	0.13	0.04	99.88
B2-Ol-5a	37.71	0.00	0.01	23.72	0.30	37.68	0.21	0.00	99.63
B2-Ol-5b	37.85	0.00	0.08	23.99	0.23	37.68	0.16	0.00	99.99

Sample Name	SiO2	TiO2	Al2O3	FeO	MnO	MgO	CaO	Cr2O3	Total
B2-Ol-5c	37.35	0.01	0.05	23.75	0.32	38.07	0.24	0.00	99.79
B2-Ol-5d	37.22	0.07	0.01	24.96	0.27	36.77	0.23	0.00	99.53
B2-Ol-5d	37.20	0.01	0.01	24.02	0.23	38.09	0.12	0.03	99.71
B2-Ol-7	38.07	0.01	0.05	23.58	0.27	37.70	0.11	0.00	99.80
B2-Ol-8	38.01	0.07	0.04	23.21	0.22	38.14	0.12	0.04	99.85
B2-Ol-9	38.46	0.07	0.05	24.40	0.26	37.32	0.14	0.05	100.75
B2-Ol-10	37.26	0.00	0.01	23.62	0.27	37.30	0.19	0.00	98.65
B2-Ol-11	42.79	4.30	8.44	8.96	0.09	10.37	21.63	0.00	96.58
B2-Ol-12	37.36	0.05	0.01	25.63	0.19	36.01	0.27	0.02	99.54
B2-Ol-13	37.48	0.11	0.03	23.72	0.23	36.97	0.22	0.00	98.75
B2-Ol-14	38.00	0.02	0.03	24.02	0.21	37.80	0.16	0.00	100.23
B2-Ol-15	37.93	0.04	0.03	23.29	0.20	38.37	0.22	0.00	100.07
Spring water 01	39.26	0.06	0.00	16.89	0.20	43.38	0.00	0.00	99.78
Spring water 02	39.03	0.03	0.00	16.84	0.18	43.61	0.01	0.00	99.70
M-Ol-1	37.35	0.00	0.06	25.00	0.23	36.70	0.12	0.00	99.46
M-Ol-2	37.48	0.06	0.03	24.23	0.27	36.53	0.22	0.00	98.81
M-Ol-3	37.48	0.01	0.03	24.30	0.26	37.26	0.14	0.01	99.50
M-Ol-4	37.79	0.00	0.04	23.77	0.17	37.64	0.10	0.05	99.54
M-Ol-5	37.37	0.02	0.05	24.30	0.20	37.22	0.13	0.03	99.30
M-Ol-6	37.30	0.07	0.00	24.97	0.27	36.84	0.12	0.00	99.57
M-Ol-7	37.52	0.00	0.05	23.71	0.15	38.17	0.10	0.00	99.70
M-Ol-8	37.20	0.00	0.04	26.07	0.33	36.01	0.28	0.00	99.92
M-Ol-9	37.87	0.00	0.01	23.32	0.22	37.57	0.14	0.00	99.13
M-Ol-10	34.17	0.41	0.23	31.29	0.19	28.39	0.29	0.00	94.98

Sample Name	SiO2	TiO2	Al2O3	FeO	MnO	MgO	CaO	Cr2O3	Total
M-Ol-11	37.68	0.00	0.02	23.44	0.19	37.46	0.20	0.05	99.04
M-Ol-12	37.81	0.00	0.02	23.70	0.19	38.17	0.26	0.03	100.17
M-Ol-13	37.73	0.00	0.04	23.36	0.21	37.88	0.12	0.01	99.34
M-Ol-14	37.74	0.03	0.07	24.37	0.20	37.53	0.15	0.01	100.07
M-Ol-15	37.51	0.00	0.01	23.92	0.21	37.47	0.12	0.00	99.24
M-Ol-15b	36.97	0.01	0.08	24.21	0.19	37.51	0.14	0.03	99.13
M-Ol-15c	37.34	0.05	0.07	23.52	0.25	37.13	0.12	0.01	98.50
M-Ol-16	37.58	0.04	0.02	25.07	0.29	36.68	0.13	0.00	99.81
M-Ol-17	37.53	0.00	0.07	23.16	0.18	38.10	0.12	0.05	99.21
Springwater-05	38.89	0.00	0.01	16.83	0.26	43.81	0.00	0.04	99.83
Springwater-06	39.32	0.00	0.00	16.79	0.23	42.90	0.00	0.00	99.24

Fe-Ti Oxides

Sample Name	TiO2	MnO	MgO	SiO2	Al2O3	FeO	Cr2O3	Total
magnetite-01	0.027	0.04	0.092	0.004	0.021	90.628	0.294	91.106
magnetite-02	0.015	0.032	0.072	0.007	0.019	90.296	0.245	90.686
Ilmenite-01	43.243	4.6	0.25	0	0.045	45.71	0	93.848
Ilmenite-02	40.664	4.476	0.246	0	0.025	45.429	0.008	90.848
B1-OP-1	13.097	0.413	4.837	0.041	5.559	62.089	4.705	90.741
B1-OP-2	14.914	0.53	4.66	0.038	4.825	63.809	0	88.776
B1-OP-3	15.24	0.378	4.832	0.09	4.688	66.377	0.456	92.061
B1-OP-4	16.647	0.522	4.598	0.05	5.033	64.862	0.008	91.72
B1-OP-6	0.597	0.357	4.002	26.68	15.047	39.408	0.031	86.122
B1-OP-7	15.353	0.493	4.406	0.065	4.695	65.313	0.025	90.35
B1-OP-8	15.67	0.519	4.267	0.081	5.068	66.034	0.324	91.963
B2-OP-1	27.054	0.237	1.244	0.086	4.866	64.735	0	98.222
B2-OP-2a	15.931	0.392	4.566	0.086	4.888	65.596	0.075	91.534
B2-OP-2b	15.251	0.539	4.431	0.086	4.58	62.592	0	87.479
B2-OP-3	16.086	0.517	4.759	0.066	4.579	65.6	0.187	91.794
B2-OP-4	18.637	0.453	4.559	0.041	4.592	66.217	0.078	94.577
B2-OP-5	35.732	0.685	1.979	0.013	0.338	59.304	0.008	98.059
B2-OP-6	14.888	0.458	4.442	0.045	4.651	66.299	0.084	90.867
M-OP-1	11.218	0.712	2.504	0.106	3.321	74.435	0.036	92.332
M-OP-2	14.862	0.437	6.189	0.283	8.331	60.613	0.164	90.879
magnetite0-3	0	0.061	0.095	0.018	0.042	90.953	0.288	91.457
magnetite0-4	0.009	0.103	0.108	0.005	0.062	90.318	0.284	90.889

Sample Name	TiO2	MnO	MgO	SiO2	Al2O3	FeO	Cr2O3	Total
ilmenite-03	45.592	4.607	0.306	0	0.007	44.798	0.025	95.335
ilmenite-04	48.865	4.768	0.274	0	0	45.707	0.093	99.707

Appendix 3:

Grain size (Under)

	AS	A	B	C	D	E	F
0.05	0	0	0	0	0	0	0
0.06	0	0	0	0	0	0	0
0.12	0	0	0	0	0	0	0
0.24	0	0	0	0	0	0	0
0.49	0	0.56	0.7	0.24	0.34	0.04	0.32
0.98	1.97	14.88	14.12	11.33	8.03	2.1	10.28
2.00	7.33	27.16	23.47	23.04	14.17	4.12	19.75
3.90	15.96	45.41	40.47	39.43	23.17	7.7	33.83
7.80	35.08	66.09	60.62	55.95	32.53	11.92	48.13
15.60	62.26	84.15	78.39	71.92	44.94	17.31	62.86
31.00	84.12	95.46	90.82	86.67	64.1	25.24	78.51
37.00	88.24	97.06	92.97	89.83	69.82	27.84	82.11
44.00	91.75	98.21	94.68	92.56	75.36	30.59	85.3
53.00	94.91	99.03	96.08	95.03	80.95	33.78	88.27
63.00	97.19	99.5	97.01	96.82	85.52	36.92	90.57
74.00	98.74	99.77	97.62	98.08	89.12	39.93	92.36
88.00	99.72	99.93	98.04	99.02	92.15	43.23	93.92
105.00	100	100	98.29	99.58	94.33	46.58	95.18
125.00	100	100	98.45	99.88	95.79	49.84	96.2
149.00	100	100	98.57	100	96.68	53.06	97.02
177.00	100	100	98.68	100	97.26	56.19	97.68
210.00	100	100	98.84	100	97.74	59.29	98.23
250.00	100	100	99.05	100	98.26	62.54	98.71
300.00	100	100	99.3	100	98.85	66.09	99.15
350.00	100	100	99.53	100	99.34	69.28	99.48
420.00	100	100	99.75	100	99.76	73.4	99.78
500.00	100	100	99.91	100	99.97	77.68	99.97
590.00	100	100	100	100	100	81.99	100
710.00	100	100	100	100	100	86.89	100
840.00	100	100	100	100	100	91.08	100
1000.00	100	100	100	100	100	94.77	100
1190.00	100	100	100	100	100	97.5	100
1410.00	100	100	100	100	100	99.25	100
1680.00	100	100	100	100	100	99.97	100
2000.00	100	100	100	100	100	100	100
2380.00	100	100	100	100	100	100	100
2830.00	100	100	100	100	100	100	100
3360.00	100	100	100	100	100	100	100
Dx (10)	2.6	0.801	0.805	0.915	1.22	5.72	0.964
Dx (50)	11.4	4.54	5.4	6.03	19.2	126	8.56
Dx (90)	40.2	21	29.3	37.4	77.4	804	60.1
D [4,3]	17	8.45	15	13.7	35.1	283	25.5
D [3,2]	6.03	2.33	2.53	2.8	4.24	12.8	3.17
Kurtosis3	3.317	11.044	74.076	7.506	21.202	1.47	27.601
Skew3	1.785	2.825	7.912	2.469	4.039	1.45	4.662
Mode	11.5	4.58	4.69	3.21	35.4	616	20.1
Span	3.284	4.443	5.277	6.05	3.966	6.327	6.913

	G	H	I	J	K	L	M
0.05	0	0	0	0	0	0	0
0.06	0	0	0	0	0	0	0
0.12	0	0	0	0	0	0	0
0.24	0	0	0	0	0	0	0
0.49	0.57	0.32	0.14	0.05	0.07	0.91	0.06
0.98	10.94	5.95	7.73	5.04	4.83	13.14	5.16
2.00	17.41	10.02	15.67	11.92	10.27	20.16	12.07
3.90	26.49	16.45	27.83	21.75	17.74	33.41	22.52
7.80	35.7	23.06	41.89	33.28	25.84	48.07	#REF!
15.60	46.91	30.94	56.11	46.31	34.83	63.06	50.34
31.00	62.34	41.22	70.1	60.72	46.03	77.59	65.81
37.00	66.61	44.25	73.55	64.43	49.37	80.77	69.84
44.00	70.62	47.36	76.83	68.01	52.73	83.57	73.73
53.00	74.57	50.82	80.21	71.72	56.28	86.15	77.74
63.00	77.75	54.1	83.15	75	59.38	88.12	81.18
74.00	80.31	57.13	85.71	77.86	61.98	89.64	84.07
88.00	82.65	60.26	88.21	80.71	64.41	90.95	86.75
105.00	84.72	63.25	90.46	83.33	66.5	91.99	88.98
125.00	86.66	65.97	92.44	85.69	68.31	92.82	90.78
149.00	88.63	68.5	94.15	87.85	69.93	93.48	92.19
177.00	90.67	70.87	95.61	89.81	71.41	93.99	93.29
210.00	92.79	73.2	96.87	91.64	72.81	94.43	94.22
250.00	94.92	75.67	97.93	93.38	74.19	94.87	95.05
300.00	96.94	78.44	98.81	95.09	75.63	95.41	95.87
350.00	98.32	80.96	99.38	96.42	76.89	95.96	96.56
420.00	99.36	84.2	99.78	97.78	78.63	96.74	97.37
500.00	99.86	87.48	99.97	98.83	80.67	97.57	98.16
590.00	100	90.68	100	99.54	83.1	98.36	98.87
710.00	100	94.06	100	99.92	86.44	99.12	99.5
840.00	100	96.68	100	100	89.77	99.62	99.86
1000.00	100	98.65	100	100	93.14	99.91	100
1190.00	100	99.72	100	100	96.02	100	100
1410.00	100	99.99	100	100	98.15	100	100
1680.00	100	100	100	100	99.47	100	100
2000.00	100	100	100	100	99.95	100	100
2380.00	100	100	100	100	100	100	100
2830.00	100	100	100	100	100	100	100
3360.00	100	100	100	100	100	100	100
Dx (10)	0.92	1.99	1.2	1.68	1.94	0.812	1.66
Dx (50)	18.2	50.7	11.6	18.7	38.2	8.55	15.4
Dx (90)	167	570	101	180	850	77.3	115
D [4,3]	52.3	173	36.4	61.1	233	45.2	52
D [3,2]	3.58	5.92	3.87	5.05	6.03	2.9	4.84
Kurtosis3	6.63	2.784	12.418	9.491	2.959	22.804	19.759
Skew3	2.522	1.834	3.197	2.916	1.916	4.573	4.153
Mode	30.9	533	14.9	26.5	819	15.4	30.4
Span	9.159	11.184	8.603	9.555	22.183	8.942	7.4

	N	O	P	Q	R	S	T
0.05	0	0	0	0	0	0	0
0.06	0	0	0	0	0	0	0
0.12	0	0	0	0	0	0	0
0.24	0	0	0	0	0	0	0
0.49	0.07	0	0.09	0.47	0.08	0.06	0
0.98	6.52	3.94	4.98	9.28	6.8	3.9	2.13
2.00	15.5	10.19	10.17	16.03	16.49	8.14	5.93
3.90	28.81	19.73	20.72	26.62	29.26	13.32	14.53
7.80	44.39	31.33	34.97	38.87	43.29	18.47	32.9
15.60	60.08	43.2	52.01	52.06	57.85	23.82	64.81
31.00	74.88	55.07	72.22	64.89	71.44	30.48	87.48
37.00	78.28	58.09	77.13	67.6	74.4	32.62	89.81
44.00	81.39	61.03	81.51	69.91	77.07	35.01	91.39
53.00	84.42	64.19	85.56	72	79.69	38.01	92.72
63.00	86.92	67.12	88.61	73.66	81.91	41.33	93.85
74.00	88.95	69.83	90.89	75.14	83.82	44.91	94.91
88.00	90.82	72.73	92.77	76.88	85.7	49.33	96.03
105.00	92.41	75.7	94.21	79.04	87.46	54.43	97.06
125.00	93.77	78.69	95.35	81.63	89.07	59.87	97.9
149.00	94.98	81.8	96.33	84.73	90.58	65.66	98.51
177.00	96.09	84.94	97.24	88.02	92.01	71.46	98.94
210.00	97.14	88.12	98.12	91.26	93.43	77.17	99.25
250.00	98.11	91.28	98.92	94.18	94.9	82.73	99.51
300.00	98.99	94.34	99.57	96.64	96.43	88.06	99.75
350.00	99.54	96.55	99.9	98.17	97.65	91.98	99.91
420.00	99.91	98.45	100	99.26	98.8	95.59	100
500.00	100	99.58	100	99.8	99.55	98.03	100
590.00	100	100	100	100	99.91	99.42	100
710.00	100	100	100	100	100	99.96	100
840.00	100	100	100	100	100	100	100
1000.00	100	100	100	100	100	100	100
1190.00	100	100	100	100	100	100	100
1410.00	100	100	100	100	100	100	100
1680.00	100	100	100	100	100	100	100
2000.00	100	100	100	100	100	100	100
2380.00	100	100	100	100	100	100	100
2830.00	100	100	100	100	100	100	100
3360.00	100	100	100	100	100	100	100
Dx (10)	1.31	1.97	1.97	1.05	1.25	2.57	2.93
Dx (50)	10	23.1	14.5	14	10.8	90.1	11.5
Dx (90)	81.3	233	69.2	196	139	323	37.7
D [4,3]	31.5	73.8	30.1	58.6	45.9	129	20.3
D [3,2]	3.93	5.75	5.02	3.76	3.89	7.87	6.28
Kurtosis3	13.826	3.366	14.665	4.408	10.444	1.391	34.888
Skew3	3.458	1.923	3.482	2.112	3.106	1.302	5.171
Mode	12.2	194	23.9	15.8	13.6	168	13
Span	8.001	9.998	4.633	13.907	12.784	3.557	3.012

	U	V	W	X	Y	Z	AA
0.05	0	0	0	0	0	0	0
0.06	0	0	0	0	0	0	0
0.12	0	0	0	0	0	0	0
0.24	0	0	0	0	0	0	0
0.49	0	0	0	0	0	0	0
0.98	1.52	0.74	0.6	0.78	0.37	1	0.61
2.00	3.47	2.12	1.62	2.61	1.25	3.17	1.9
3.90	6.68	5.62	3.47	5.09	2.88	6.09	3.66
7.80	11.15	12.11	6.62	9.65	5.54	10.94	6.49
15.60	16.9	21.51	11.72	20.72	9.66	21.35	11.86
31.00	23.88	33.5	18.54	37.77	15.37	42.98	24.42
37.00	25.86	36.9	20.31	41.62	16.94	49.56	29.67
44.00	27.91	40.29	21.96	44.9	18.45	55.73	35.59
53.00	30.31	44.01	23.68	47.87	20.05	61.71	42.76
63.00	32.82	47.52	25.31	50.22	21.54	66.47	49.97
74.00	35.45	50.8	27.03	52.2	23.01	70.25	56.85
88.00	38.71	54.28	29.39	54.18	24.86	73.68	64.1
105.00	42.59	57.68	32.79	56.07	27.31	76.65	70.96
125.00	46.92	60.82	37.42	57.82	30.55	79.3	76.99
149.00	51.85	63.69	43.88	59.48	35.15	81.81	82.05
177.00	57.13	66.21	51.85	61.16	41.09	84.28	86.14
210.00	62.71	68.49	61.03	63.11	48.35	86.82	89.53
250.00	68.64	70.61	71.11	65.81	57.08	89.51	92.37
300.00	74.84	72.73	81.24	69.63	66.82	92.35	94.9
350.00	79.9	74.48	88.65	73.75	74.93	94.62	96.7
420.00	85.33	76.62	94.92	79.6	83.44	96.88	98.28
500.00	89.87	78.8	98.52	85.53	90.07	98.52	99.29
590.00	93.44	81.08	99.99	90.85	94.72	99.51	99.83
710.00	96.4	83.87	100	95.52	97.87	99.95	100
840.00	98.29	86.52	100	98.38	99.42	100	100
1000.00	99.45	89.25	100	99.8	100	100	100
1190.00	99.93	91.82	100	100	100	100	100
1410.00	100	94.07	100	100	100	100	100
1680.00	100	96.02	100	100	100	100	100
2000.00	100	97.57	100	100	100	100	100
2380.00	100	98.76	100	100	100	100	100
2830.00	100	99.53	100	100	100	100	100
3360.00	100	99.93	100	100	100	100	100
Dx (10)	6.62	6.42	12.8	8.06	16.3	7.01	13
Dx (50)	140	71.1	171	61.9	217	37.4	63
Dx (90)	503	1050	363	574	499	258	216
D [4,3]	204	321	180	202	242	86.4	93.5
D [3,2]	14.7	15.9	24.7	16	30.6	13.5	20.5
Kurtosis3	2.227	6.469	-0.416	0.332	0.465	5.019	5.588
Skew3	1.484	2.462	0.503	1.159	0.833	2.246	2.164
Mode	252	65.3	236	459	287	32.4	69.1
Span	3.549	14.676	2.051	9.14	2.221	6.701	3.218

	AB	AC	AD	AD2	AE	AF	AG
0.05	0	0	0	0	0	0	0
0.06	0	0	0	0	0	0	0
0.12	0	0	0	0	0	0	0
0.24	0	0	0	0	0	0	0
0.49	0	0	0	0	0	0	0
0.98	0.62	0.6	0.95	0.92	0.89	3.09	1.46
2.00	1.7	1.79	3.54	3.47	3.26	10.63	4.82
3.90	3.22	3.99	9.47	9.3	6.56	25.1	9.56
7.80	5.72	7.53	21.64	21.7	13.61	57.34	19.26
15.60	10.5	12.61	43.96	45.61	27.91	89.08	45.13
31.00	20.83	20.06	70.45	73.19	44.77	98.65	78.97
37.00	25.17	22.64	76.1	78.56	48.76	99.03	85.17
44.00	30.34	25.53	81.07	83.09	52.63	99.22	89.87
53.00	37.15	29.1	85.76	87.25	56.89	99.37	93.48
63.00	44.75	32.91	89.5	90.51	61.11	99.54	95.7
74.00	52.68	36.82	92.44	93.09	65.28	99.69	97.1
88.00	61.83	41.4	94.96	95.33	69.96	99.84	98.05
105.00	71.18	46.37	96.82	97.03	74.77	99.96	98.63
125.00	79.75	51.47	98.08	98.21	79.29	100	99
149.00	86.94	56.78	98.82	98.95	83.34	100	99.27
177.00	92.34	62.16	99.25	99.39	86.7	100	99.49
210.00	96.11	67.67	99.53	99.67	89.47	100	99.7
250.00	98.32	73.46	99.73	99.85	91.74	100	99.87
300.00	99.51	79.5	99.91	99.98	93.74	100	99.98
350.00	99.92	84.38	100	100	95.24	100	100
420.00	100	89.5	100	100	96.78	100	100
500.00	100	93.58	100	100	98.05	100	100
590.00	100	96.53	100	100	99.01	100	100
710.00	100	98.63	100	100	99.68	100	100
840.00	100	99.7	100	100	99.97	100	100
1000.00	100	100	100	100	100	100	100
1190.00	100	100	100	100	100	100	100
1410.00	100	100	100	100	100	100	100
1680.00	100	100	100	100	100	100	100
2000.00	100	100	100	100	100	100	100
2380.00	100	100	100	100	100	100	100
2830.00	100	100	100	100	100	100	100
3360.00	100	100	100	100	100	100	100
Dx (10)	14.8	11.3	4.07	4.12	5.9	1.91	4.1
Dx (50)	70.2	119	18.2	17.3	39.1	6.82	17.2
Dx (90)	163	428	64.6	61.2	218	16.1	44.2
D [4,3]	81.7	176	28.4	26.9	85.3	8.55	22.9
D [3,2]	22.3	22.1	9.05	8.99	12.6	4.23	8.36
Kurtosis3	1.549	1.66	17.061	14.203	8.415	39.145	31.443
Skew3	1.134	1.377	3.291	3.09	2.675	4.78	4.452
Mode	88.6	250	18.8	17.9	89.8	7.85	19
Span	2.106	3.506	3.334	3.301	5.429	2.078	2.339

	AH	AI	AJ	AK	AL	AM	AN
0.05	0	0	0	0	0	0	0
0.06	0	0	0	0	0	0	0
0.12	0	0	0	0	0	0	0
0.24	0	0	0	0	0	0	0
0.49	0	0	0	0	0	0	0
0.98	0.91	5.16	1.59	4.74	2.4	1.2	0.99
2.00	3.42	17.61	5.06	16.8	8.11	3.81	3.15
3.90	9.07	43.63	9.92	37.2	17.05	7.77	6.5
7.80	21.94	73.03	17.85	61.02	34.53	13.83	11.78
15.60	48.33	87.67	32.86	81.31	64.36	22.61	19.58
31.00	74.99	93.86	61.11	95.25	90.74	38.47	33.12
37.00	80.54	94.75	69.54	97.38	94.39	44.97	38.74
44.00	85.44	95.42	77.35	98.84	96.82	52.3	45.26
53.00	89.99	95.94	84.72	99.73	98.39	61.04	53.36
63.00	93.4	96.3	90.19	99.99	99.15	69.47	61.62
74.00	95.87	96.55	94.07	100	99.54	77.07	69.47
88.00	97.72	96.76	96.92	100	99.77	84.4	77.55
105.00	98.84	96.94	98.6	100	99.9	90.41	84.75
125.00	99.45	97.09	99.48	100	99.99	94.83	90.55
149.00	99.72	97.21	99.84	100	100	97.61	94.7
177.00	99.84	97.3	99.97	100	100	99.11	97.35
210.00	99.94	97.39	100	100	100	99.81	98.91
250.00	100	97.49	100	100	100	100	99.65
300.00	100	97.64	100	100	100	100	99.96
350.00	100	97.79	100	100	100	100	100
420.00	100	98.01	100	100	100	100	100
500.00	100	98.25	100	100	100	100	100
590.00	100	98.48	100	100	100	100	100
710.00	100	98.73	100	100	100	100	100
840.00	100	98.95	100	100	100	100	100
1000.00	100	99.15	100	100	100	100	100
1190.00	100	99.35	100	100	100	100	100
1410.00	100	99.52	100	100	100	100	100
1680.00	100	99.69	100	100	100	100	100
2000.00	100	99.83	100	100	100	100	100
2380.00	100	99.94	100	100	100	100	100
2830.00	100	100	100	100	100	100	100
3360.00	100	100	100	100	100	100	100
Dx (10)	4.21	1.37	3.94	1.41	2.39	5.18	6.35
Dx (50)	16.2	4.46	24.4	5.62	11.5	41.8	49.2
Dx (90)	53	19.1	62.6	22.9	30.2	104	123
D [4,3]	23.7	30.6	29.9	9.3	14.6	49.3	58.7
D [3,2]	8.87	3.14	9.04	3.46	5.7	11.9	13.7
Kurtosis3	9.966	98.791	2.923	3.905	8.574	1.33	1.938
Skew3	2.47	9.269	1.437	1.914	2.189	1.112	1.244
Mode	15.1	4.17	31.9	4.56	14.5	57.8	66.6
Span	3.01	3.974	2.399	3.814	2.425	2.356	2.368

	AO	AP	AQ	AR	AT	AU	#1
0.05	0	0	0	0	0	0	0
0.06	0	0	0	0	0	0	0
0.12	0	0	0	0	0	0	0
0.24	0	0	0	0	0	0	0
0.49	0	0	0	0	0	0	0
0.98	0.55	0.53	2.03	0.89	0.76	1.16	0.31
2.00	1.56	1.62	8.32	2.78	2.56	3.42	0.95
3.90	3.26	3.61	19.87	5.52	4.69	8.87	2.14
7.80	5.72	6.74	44.88	9.16	8.15	18.01	4.24
15.60	9.04	11.21	76.59	14.14	17.17	38.31	7.56
31.00	13.81	17.57	94.62	23.55	39.38	65.2	14.13
37.00	15.53	19.63	96.39	26.9	47.56	71.6	15.72
44.00	17.53	21.88	97.46	30.34	56.1	77.48	16.95
53.00	20.14	24.58	98.13	34.1	65.47	83.18	18.11
63.00	23.13	27.41	98.49	37.57	73.84	87.73	19.7
74.00	26.41	30.32	98.73	40.84	80.94	91.27	22.41
88.00	30.58	33.77	98.92	44.58	87.4	94.22	27.74
105.00	35.53	37.63	99.09	48.95	92.39	96.34	36.53
125.00	41.01	41.72	99.22	54.03	95.88	97.76	48.03
149.00	47.14	46.13	99.33	60.24	97.94	98.63	61.54
177.00	53.55	50.68	99.41	67.22	99.01	99.17	74.66
210.00	60.13	55.36	99.5	74.67	99.52	99.53	85.87
250.00	66.81	60.2	99.59	82.16	99.74	99.79	93.71
300.00	73.45	65.15	99.71	89.13	99.89	99.97	98.34
350.00	78.55	69.1	99.83	93.83	100	100	99.96
420.00	83.68	73.3	99.95	97.43	100	100	100
500.00	87.75	76.84	100	99.3	100	100	100
590.00	90.88	79.78	100	100	100	100	100
710.00	93.61	82.63	100	100	100	100	100
840.00	95.6	84.99	100	100	100	100	100
1000.00	97.21	87.3	100	100	100	100	100
1190.00	98.43	89.59	100	100	100	100	100
1410.00	99.29	91.84	100	100	100	100	100
1680.00	99.82	94.13	100	100	100	100	100
2000.00	99.99	96.23	100	100	100	100	100
2380.00	100	97.99	100	100	100	100	100
2830.00	100	99.22	100	100	100	100	100
3360.00	100	99.89	100	100	100	100	100
Dx (10)	18.4	13.2	2.29	8.98	9.69	4.34	20.9
Dx (50)	161	173	8.71	109	38.9	21	128
Dx (90)	562	1230	23.8	307	95.8	69.6	228
D [4,3]	243	408	13.5	136	47.7	31.4	130
D [3,2]	27.6	25.2	5.15	17.5	15.4	9.69	33.9
Kurtosis3	6.615	5.467	123.867	0.269	6.361	11.793	-0.358
Skew3	2.29	2.333	10.017	0.926	1.862	2.784	0.219
Mode	207	226	9.95	206	47.3	20.5	148
Span	3.373	7.036	2.474	2.732	2.212	3.109	1.616

	#2	#3
0.05	0	0
0.06	0	0
0.12	0	0
0.24	0	0
0.49	0	0
0.98	1.05	0.83
2.00	2.51	1.81
3.90	5.23	3.73
7.80	9.46	6.95
15.60	14.99	11.4
31.00	22.16	17.94
37.00	24.35	20.08
44.00	26.46	22.12
53.00	28.49	23.97
63.00	30.07	25.24
74.00	31.4	26.15
88.00	33.11	27.33
105.00	35.92	29.69
125.00	40.35	34.01
149.00	47.27	41.47
177.00	56.08	51.57
210.00	65.97	63.39
250.00	75.89	75.68
300.00	84.68	86.81
350.00	90.17	93.78
420.00	93.95	98.36
500.00	95.77	99.9
590.00	96.54	100
710.00	97.02	100
840.00	97.52	100
1000.00	98.17	100
1190.00	98.82	100
1410.00	99.33	100
1680.00	99.68	100
2000.00	99.88	100
2380.00	100	100
2830.00	100	100
3360.00	100	100
Dx (10)	8.41	12.8
Dx (50)	158	173
Dx (90)	348	320
D [4,3]	189	170
D [3,2]	18	23
Kurtosis3	21.731	-0.675
Skew3]	3.842	0.216
Mode	206	215
Span	2.154	1.78

Appendix 4:

EMPA- Tephra Analysis

Sample name	SiO2	TiO2	Al2O3	FeO	MnO	MgO	CaO	Na2O	K2O	Cl	H2O
TA_1	75.01	0.21	13.51	2.09	0.05	0.14	1.34	4.47	3.19	0.18	4.61
TA_2	75.86	0.20	13.40	2.01	0.07	0.15	1.30	4.13	2.89	0.19	6.64
TA_3	76.88	0.15	13.15	1.63	0.03	0.10	1.00	3.44	3.62	0.17	6.15
TA_4	76.61	0.09	12.85	1.56	0.03	0.05	0.84	4.10	3.86	0.17	5.24
TA_5	75.13	0.22	13.46	2.07	0.07	0.18	1.27	4.55	3.06	0.17	4.58
TA_6	76.04	0.17	13.21	1.89	0.06	0.10	1.04	4.12	3.37	0.19	6.08
TA_7	77.51	0.11	12.74	1.59	0.07	0.07	0.83	3.42	3.66	0.18	6.24
TA_8	75.25	0.18	13.32	2.10	0.06	0.16	1.28	4.44	3.21	0.16	5.16
TA_9	76.62	0.12	12.96	1.61	0.09	0.07	0.91	4.04	3.59	0.17	6.06
TA_10	76.37	0.13	13.04	1.74	0.04	0.08	1.01	4.16	3.44	0.18	5.75
TA_11	75.28	0.21	13.47	2.13	0.05	0.14	1.33	4.42	2.97	0.17	5.31
TA_12	77.41	0.12	13.09	1.62	0.08	0.07	0.91	2.81	3.90	0.18	6.04
TA_13	76.75	0.16	12.95	1.84	0.02	0.11	0.97	3.64	3.57	0.16	5.64
TA_14	76.42	0.16	12.97	1.87	0.04	0.11	1.05	4.01	3.37	0.19	5.61
TA_15	75.02	0.22	13.62	2.18	0.06	0.18	1.35	4.25	3.13	0.17	5.41
TA_18	75.08	0.22	13.39	2.24	0.06	0.15	1.28	4.38	3.20	0.19	4.98
TA_19	76.58	0.13	12.96	1.60	0.07	0.07	0.88	3.91	3.80	0.19	5.58
TA_20	75.21	0.22	13.53	2.13	0.06	0.18	1.30	4.15	3.23	0.19	6.04
TB_1	76.65	0.12	12.91	1.66	0.06	0.08	0.88	4.00	3.64	0.16	5.56
TB_2	76.62	0.13	12.93	1.56	0.08	0.08	0.89	4.17	3.53	0.16	5.54
TB_3	76.03	0.12	13.44	1.84	0.07	0.08	1.17	4.06	3.19	0.17	6.13
TB_4	76.60	0.12	12.87	1.73	0.05	0.06	0.83	4.12	3.63	0.16	5.10
TB_5	76.37	0.11	13.00	1.76	0.04	0.07	0.89	4.13	3.63	0.19	4.83
TB_6	76.54	0.10	12.99	1.68	0.04	0.09	0.91	3.83	3.83	0.17	5.52

Sample name	SiO2	TiO2	Al2O3	FeO	MnO	MgO	CaO	Na2O	K2O	Cl	H2O
TB_7	76.67	0.12	12.99	1.69	0.03	0.08	0.93	3.88	3.60	0.19	6.22
TB_8	76.45	0.12	12.90	1.66	0.06	0.07	0.90	4.13	3.73	0.17	6.06
TB_9	76.25	0.13	12.94	1.71	0.05	0.05	0.91	4.12	3.83	0.18	5.05
TB_10	76.56	0.13	12.77	1.68	0.08	0.05	0.83	4.21	3.68	0.17	5.09
TB_11	76.78	0.12	13.16	1.77	0.06	0.07	0.91	3.80	3.34	0.18	6.14
TB_12	76.43	0.13	13.07	1.71	0.04	0.07	0.93	4.11	3.52	0.21	5.90
TB_13	76.50	0.11	13.02	1.75	0.08	0.09	0.92	4.06	3.49	0.17	5.65
TB_14	75.85	0.23	13.59	1.63	0.03	0.26	1.48	3.60	3.34	0.17	6.65
TB_15	76.93	0.13	12.95	1.55	0.03	0.08	0.91	3.91	3.51	0.19	5.91
TB_16	76.92	0.15	13.07	1.77	0.02	0.07	0.89	3.65	3.46	0.17	5.68
TB_17	76.54	0.15	13.09	1.65	0.06	0.09	0.92	3.95	3.56	0.20	5.20
TB_18	74.74	0.19	13.67	2.20	0.06	0.14	1.39	4.32	3.28	0.18	4.72
TB_19	73.37	0.34	13.99	2.72	0.06	0.28	1.84	4.26	3.15	0.12	5.44
TB_20	76.63	0.14	12.79	1.70	0.03	0.07	0.93	4.08	3.63	0.17	5.84
TL_12	76.54	0.14	13.41	1.97	0.06	0.11	1.14	3.02	3.63	0.22	5.38
TL_17	77.96	0.12	12.31	1.22	0.01	0.09	0.96	3.25	4.08	0.26	3.80
TO_1	76.85	0.10	12.96	1.57	0.01	0.05	1.07	3.37	4.01	0.13	3.61
TO_2	75.65	0.15	13.37	1.78	0.04	0.06	0.92	4.31	3.73	0.19	5.35
TO_3	76.88	0.18	12.97	1.34	0.05	0.19	1.27	3.59	3.54	0.16	4.38
TO_4	77.73	0.07	12.72	1.32	0.00	0.10	1.26	3.64	3.16	0.15	6.53
TO_5	77.57	0.06	12.63	1.08	0.06	0.08	1.15	3.56	3.82	0.16	5.52
TO_6	77.86	0.14	12.16	1.18	0.01	0.10	0.96	3.55	4.04	0.27	3.75
TO_7	76.46	0.17	12.97	1.71	0.05	0.11	1.11	3.99	3.46	0.17	3.95
TO_8	77.66	0.14	12.27	1.27	0.06	0.12	0.92	3.51	4.06	0.25	3.17

Sample name	SiO2	TiO2	Al2O3	FeO	MnO	MgO	CaO	Na2O	K2O	Cl	H2O
TO_9	77.22	0.15	12.52	1.26	0.04	0.10	1.02	3.68	4.02	0.26	3.63
TO_11	77.68	0.13	12.28	1.32	0.01	0.12	0.99	3.47	4.01	0.26	4.37
TO_13	77.39	0.06	12.81	1.16	0.02	0.05	1.06	3.51	3.95	0.16	4.78
TO_16	76.87	0.13	12.44	1.51	0.04	0.07	0.95	3.03	4.97	0.13	5.17
TO_17	77.75	0.08	12.62	1.15	0.06	0.02	0.95	3.70	3.67	0.15	4.68
TO_18	77.52	0.09	12.48	1.41	0.03	0.06	0.93	3.70	3.79	0.13	4.12
TO_20	77.06	0.17	12.85	1.25	0.04	0.16	1.19	3.75	3.54	0.17	5.84
TS_2	78.56	0.11	12.95	1.54	0.03	0.09	0.99	2.17	3.56	0.21	6.72
TS_3	78.74	0.14	13.16	1.65	0.06	0.07	0.99	1.78	3.40	0.20	7.27
TS_10	78.48	0.14	13.19	1.42	0.02	0.06	1.01	2.21	3.46	0.19	6.50
TS_13	77.38	0.08	13.08	1.55	0.10	0.05	0.93	3.24	3.58	0.18	7.34
TS_17	77.04	0.14	12.89	1.60	0.04	0.08	1.01	3.07	4.13	0.22	6.56
TS_18	77.51	0.11	13.12	1.57	0.01	0.10	1.00	3.24	3.34	0.18	5.36
TR_1	76.69	0.17	12.05	1.23	0.04	0.34	1.76	4.51	3.21	0.13	17.41
TR_2	74.21	0.23	14.61	1.60	0.01	0.27	1.34	4.78	2.93	0.07	19.71
TR_3	74.28	0.07	17.00	0.95	0.02	0.13	0.51	5.07	1.97	0.13	44.15
TR_4	78.28	0.05	12.48	0.56	0.03	0.09	0.69	3.62	4.19	0.20	39.75
TR_5	77.27	0.00	12.71	0.15	0.02	0.12	0.82	6.29	2.62	0.21	48.72
TR_6	52.47	0.05	36.62	0.38	0.03	0.04	9.49	0.34	0.57	0.66	38.41
TR_7	74.17	0.07	15.96	1.22	0.01	0.03	0.55	5.93	2.06	0.21	34.42
TR_8	56.21	0.03	25.89	0.22	0.04	0.04	11.89	5.53	0.16	0.00	16.94
TR_9	73.59	0.13	18.50	1.56	0.01	0.10	0.40	3.87	1.83	0.10	42.73
TR_10	76.68	0.14	13.51	1.24	0.02	0.11	0.91	4.14	3.25	0.16	23.10
TR_11	77.22	0.14	12.44	1.31	0.05	0.20	1.04	3.43	4.17	0.22	21.42

Sample name	SiO2	TiO2	Al2O3	FeO	MnO	MgO	CaO	Na2O	K2O	Cl	H2O
TR_12	58.23	0.00	27.97	0.22	0.00	0.00	4.76	8.48	0.32	0.00	22.23
TR_13	60.32	0.00	24.70	0.17	0.00	0.00	5.71	8.68	0.42	0.00	18.42
TR_14	61.64	0.00	22.41	0.06	0.01	0.01	6.22	8.83	0.82	0.00	35.99
TR_15	79.64	0.10	12.35	0.94	0.00	0.17	0.85	2.54	3.41	0.28	30.95
TR_16	77.14	0.10	12.97	0.84	0.00	0.12	0.96	4.76	3.10	0.20	27.76
TR_17	76.99	0.12	13.20	1.23	0.04	0.08	0.87	4.00	3.47	0.19	16.01
TR_18	77.83	0.08	12.95	1.22	0.02	0.06	0.65	3.24	3.94	0.23	18.95
TR_19	77.04	0.09	13.92	0.87	0.01	0.08	0.80	4.14	3.05	0.21	36.23
TR_20	76.71	0.10	13.06	1.25	0.01	0.08	0.84	4.69	3.27	0.17	17.09
TT_3	77.26	0.12	13.32	0.63	0.00	0.03	1.93	5.23	1.48	0.08	15.15
TT_7	77.48	0.09	14.51	0.82	0.02	0.11	0.92	3.53	2.53	0.93	40.48
TT_11	77.53	0.14	12.66	1.68	0.01	0.19	1.28	3.25	3.27	1.23	43.14
TT_12	75.59	0.11	13.23	2.27	0.06	0.16	2.83	2.42	3.33	1.80	49.39
TT_13	76.70	0.14	13.15	1.65	0.02	0.17	1.13	3.17	3.87	0.30	11.12
TT_15	77.00	0.14	13.33	1.66	0.00	0.14	1.25	2.76	3.72	0.29	12.73
TT_16	75.91	0.13	13.18	1.44	0.02	0.25	1.14	4.23	3.69	0.20	13.00
TT_17	75.90	0.14	13.31	1.73	0.04	0.26	1.30	3.56	3.75	0.21	13.57
TU_1	77.98	0.18	13.86	2.01	0.03	0.16	1.12	1.74	2.92	0.20	2.76
TU_3	77.12	0.16	13.37	1.90	0.06	0.18	1.24	2.37	3.60	0.19	4.83
TU_5	77.15	0.14	13.54	1.92	0.01	0.09	1.18	2.56	3.42	0.18	3.96
TU_6	76.69	0.15	13.44	1.85	0.04	0.15	1.37	3.47	2.84	0.20	4.53
TU_7	78.12	0.12	13.53	1.86	0.05	0.11	1.16	1.48	3.56	0.19	7.46
TU_8	76.94	0.13	13.43	1.88	0.04	0.14	1.24	3.09	3.13	0.23	6.41
TU_9	77.15	0.15	13.45	1.97	0.03	0.13	1.18	2.68	3.25	0.18	6.40

Sample name	SiO2	TiO2	Al2O3	FeO	MnO	MgO	CaO	Na2O	K2O	Cl	H2O
TU_11	76.98	0.12	13.36	1.68	0.04	0.06	0.99	3.59	3.19	0.19	4.97
TU_12	75.68	0.14	13.46	2.02	0.07	0.16	1.33	4.03	3.10	0.19	3.31
TU_14	76.84	0.12	13.37	1.89	0.04	0.09	1.12	3.59	2.94	0.18	5.07
TU_15	76.19	0.17	13.53	2.12	0.04	0.12	1.32	3.61	2.91	0.20	3.93
TU_16	76.00	0.17	13.57	2.19	0.03	0.13	1.40	3.59	2.91	0.20	3.82
TU_17	76.03	0.18	13.41	2.04	0.03	0.13	1.35	3.82	3.00	0.21	3.15
TU_18	79.33	0.12	12.62	0.34	0.02	0.01	0.68	2.20	4.67	0.08	6.66
TU_19	77.62	0.11	12.78	1.19	0.05	0.10	0.94	3.38	3.83	0.28	3.70
TV_1	78.12	0.13	12.67	1.17	0.00	0.10	0.89	3.28	3.63	0.28	3.94
TV_3	76.46	0.18	13.45	2.02	0.06	0.10	1.31	3.83	2.60	0.20	4.74
TV_4	77.46	0.15	12.68	1.27	0.04	0.10	0.91	3.00	4.38	0.23	2.93
TV_5	78.05	0.13	12.37	1.11	0.05	0.09	0.94	3.31	3.93	0.23	3.03
TV_6	78.20	0.12	12.53	1.06	0.02	0.02	0.89	3.42	3.73	0.27	5.54
TV_9	77.78	0.15	12.53	1.31	0.05	0.14	0.93	3.38	3.73	0.26	3.12
TV_10	76.22	0.15	13.70	1.96	0.06	0.10	1.20	3.55	3.06	0.17	4.85
TV_11	78.25	0.08	13.01	1.17	0.04	0.10	0.88	3.16	3.30	0.21	5.02
TV_12	77.27	0.14	12.84	1.35	0.05	0.11	0.89	3.38	3.97	0.27	3.29
TV_13	77.77	0.12	12.87	1.53	0.04	0.04	0.92	3.32	3.38	0.19	4.78
TV_14	77.74	0.15	12.60	1.29	0.02	0.10	0.97	3.36	3.78	0.27	2.63
TV_15	77.01	0.16	13.60	1.92	0.04	0.11	1.12	3.22	2.83	0.20	5.89
TV_16	77.37	0.11	12.67	1.35	0.01	0.09	0.93	3.56	3.91	0.29	3.19
TV_17	76.33	0.20	13.39	2.19	0.05	0.16	1.33	3.57	2.79	0.21	4.56
TV_18	77.84	0.12	12.63	1.23	0.02	0.10	0.88	3.25	3.93	0.26	2.93
TV_19	77.93	0.16	12.60	1.15	0.03	0.10	0.88	3.33	3.83	0.28	2.73

Sample name	SiO2	TiO2	Al2O3	FeO	MnO	MgO	CaO	Na2O	K2O	Cl	H2O
TV_20	78.02	0.11	12.57	1.23	0.03	0.11	0.89	3.30	3.76	0.25	3.42
TW_1	77.81	0.11	12.34	0.98	0.04	0.10	1.02	3.80	3.81	0.17	3.18
TW_2	77.88	0.06	12.51	0.82	0.03	0.09	0.63	3.90	4.08	0.17	0.99
TW_3	77.91	0.05	12.57	0.72	0.04	0.05	0.51	3.77	4.39	0.16	1.48
TW_4	77.65	0.05	12.66	0.77	0.06	0.04	0.54	3.94	4.28	0.19	3.39
TW_5	77.83	0.07	12.46	0.81	0.02	0.06	0.66	4.16	3.92	0.17	1.47
TW_6	78.01	0.09	12.43	0.72	0.07	0.06	0.60	3.88	4.13	0.17	1.49
TW_7	77.91	0.06	12.51	0.76	0.04	0.05	0.53	4.00	4.13	0.18	1.50
TW_8	77.90	0.07	12.41	0.81	0.03	0.07	0.65	4.04	4.02	0.18	2.09
TW_9	77.66	0.07	12.63	0.80	0.07	0.08	0.66	3.97	4.04	0.15	1.27
TW_10	77.73	0.07	12.53	0.76	0.05	0.07	0.66	4.09	4.04	0.18	1.61
TW_11	77.74	0.06	12.61	0.76	0.05	0.04	0.66	4.10	3.98	0.18	1.43
TW_12	77.71	0.08	12.51	0.77	0.08	0.08	0.59	4.14	4.04	0.17	0.46
TW_13	78.08	0.08	12.37	0.80	0.06	0.08	0.65	3.90	3.99	0.16	1.48
TW_14	77.88	0.08	12.53	0.87	0.03	0.07	0.63	3.94	3.99	0.17	0.69
TW_15	77.79	0.05	12.57	0.86	0.06	0.07	0.65	3.90	4.05	0.16	2.46
TW_16	77.53	0.06	12.58	0.91	0.03	0.05	0.53	4.08	4.22	0.14	1.14
TW_17	77.63	0.07	12.55	0.86	0.05	0.05	0.62	4.06	4.11	0.17	1.16
TW_18	77.77	0.09	12.60	0.77	0.05	0.07	0.58	3.76	4.31	0.15	1.18
TW_19	77.93	0.08	12.55	0.88	0.07	0.08	0.64	3.70	4.07	0.17	2.02